A PHYSICOCHEMICAL EXPERIMENTAL AND PREDICTIVE APPROACH TO ELUCIDATE BACTERIAL ATTACHMENT TO NANOSTRUCTURED SURFACES

A Dissertation

Presented to the Faculty of the Graduate School

of Cornell University

in Partial Fulfillment of the Requirements for the Degree of

Doctor of Philosophy

by

Yifan Cheng

January 2017

A PHYSICOCHEMICAL EXPERIMENTAL AND PREDICTIVE APPROACH TO ELUCIDATE BACTERIAL ATTACHMENT TO NANOSTRUCTURED SURFACES

Yifan Cheng, Ph.D.

Cornell University 2017

Prevention of bacterial attachment to various surfaces is of critical importance to areas that directly affect human health and life, including food processing, water treatment, and medicine. The past decade has witnessed a rapid growth in novel antifouling materials, some of them with features at the nanoscale.

This work focused on studying the effect of substrate and bacterial physicochemical factors, the nanoscale topography in particular, on bacterial attachment and biofilm formation.

In Chapter One, a physicochemical mathematical model was developed for the porous anodized aluminum oxide (AAO) surfaces based on the Extended Derjaguin, Landau, Verwey, and Overbeek (XDLVO) theory. By integrating the electrostatic, acid-base and van der Waals interaction forces over the surface topography of AAO, the adjusted XDLVO model is able to delineate the effect of changing pore diameter, pore depth and surface porosity on the maximum repulsive force (F_{max}), which prove to be an effective indicator of tendency for bacterial attachment. The predicted force-distance (FD) curves for a model system consisted of a polydopamine-coated microsphere and various AAO surfaces was verified with atomic force microscopy, showing that total repulsive force was indeed enhanced by the densely distributed pores covering the 15 and 25 nm pore AAO surfaces.

In Chapter Two and Chapter Three, the adjusted XDLVO model was validated with a bacterial attachment assay using surrogate strains *Escherichia coli* ATCC 25922 and *Listeria*

innocua as well as pathogenic strains *Escherichia coli* O157:H7, *Listeria monocytogenes*, *Staphylococcus aureus* and *Staphylococcus epidermidis*. As predicted by the model, surfaces with 15 and 25 nm pore diameters significantly repressed attachment and biofilm formation by all strains tested. The observed effect was attributed to the repulsive force, primarily electrostatic and acid-base forces, which were greatly enhanced by the large surface area originating from the high density, small-diameter pores. It was also demonstrated how this predictive approach could be used to optimize different elements of surface topography (particularity pore diameter and density) and surface energies for further enhancing the observed bacteria-repelling effect.

In Chapter Four, a phenomenon observed near hydrophilic surfaces, also known as particle-exclusion zones (EZ), was studied by exposing Nafion and alumina to bacteria suspensions, including *S. aureus*, *E. coli* O157:H7, and *L. monocytogenes*. Using confocal laser scanning microscopy (CLSM), bacterial cell density distribution in a 3D space near solid-liquid interface was obtained, and a robust image analysis method was developed to generate a quantitative profile of cell concentration near the interface, which allowed the precise quantification of EZ and of a transition zone (TZ), based on pixel intensity profiles. A typical bacterial EZ size of 40 - 60 μm and a TZ of 40 - 80 μm was revealed for bacteria suspended in tryptic soy broth (TSB, pH 7.0, IS $\approx$ 100 mM). In addition, surface topography appeared to influence EZ and TZ near AAO surface, with the 15 nm pore AAO having the largest combined EZ-TZ size. A robust EZ-TZ region could prove an important antifouling mechanism.

Overall, this work provides critical insights on the mechanisms of bacterial attachment to surfaces with nanoscale topography, which can be used for developing biofouling-resistant material surfaces for a wide range of applications sensitive to bacterial attachment and biofilm formation.

BIOGRAPHICAL SKETCH

Yifan Cheng was born in Shanghai, China. At the age of six, he started learning drawing and Chinese calligraphy in a local art school. Although sitting in a classroom for hours might have initially been against his will, the aesthetic beauty of strokes, patterns, and colors, as well as the pleasure of creation on a canvas soon captured Yifan's attention. After he started school, Yifan was fascinated by the order and complexity of the world unveiled by science and described in the language of mathematics, the clarity and certainty of which presented a distinctive type of beauty so different from the ineffable beauty in art. Inspired to learn more of the laws of nature and apply them in a system that is important to human life, he transferred to Cornell University from Shanghai Jiao Tong University in 2010, and majored in Food Science. There Yifan strived for academic excellence and got involved in research activities where he found great pleasure in satisfying his creativity and curiosity. After getting his Bachelor of Science degree, in the fall of 2012, Yifan joined the research group of Dr. Carmen Moraru to pursuit a PhD degree in Food Science. The PhD journey was marked with excitement of conceiving new ideas, perseverance after unsuccessful experiments, and ecstasy in moments when hypotheses were finally proved by experiments. After 4 years of hard work, Yifan was able to achieve his research goals. Upon completing his dissertation, Yifan will continue working in the same Food Safety Engineering laboratory as a postdoctoral associate, to further his ideas and also gain experience as an independent researcher.

To my grandma Changjie Mei for those bike rides that brought me closer to the beauty of drawing, calligraphy, and sciences

ACKNOWLEDGEMENTS

I would like to express my special appreciation and thanks to my PhD advisor and thesis committee chair, Professor Carmen Moraru, for your academic guidance and inspiration throughout my pursuit of the PhD degree. Over the years, your trust and support helped me through thick and thin in experiments and research, and your mentorship and scholarship inspired me to grow as a scientist. Your brilliant comments and the thought-provoking questions are key catalysts in forming my research ideas. Your sense of humor and the whole collection of "force" inside jokes we laughed at together will always (not just "may") "be with me". I would like to thank Professor Randy Worobo and Professor Michael King for being my minor committee members in the field of Microbiology and Biomedical Engineering, respectively. The conversations we had in the past few years have been an invaluable source of inspiration for my research. The knowledge and advice from your respective realm of expertise have been of tremendous help to me along my PhD journey. I would also like to thank our collaborators, Professor Diana Borca-Tasciuc and her research group, for providing the nanostructured surfaces along with their expertise and insights – these are truly indispensable ingredients to this dissertation.

I would like to acknowledge the past and present members of the Moraru Lab for your support, assistance, and all the lasting memories in and outside of the lab. Special thank you to Guoping Feng for enlightening me the first glance of the nano project, passing on your experimental skills in microbiology and microscopy, and giving me all those thoughtful tips on research and career – your mentorship and friendship mean so much to me; to Markus Ribeiro for the unforgettable time we had on the road trips, on the badminton court, and at pool tables; to Dongjun Zhao for being so warm, full of energy, and compassionate all the time. Many thanks to

Lillian Hsu, Anne Sauer for training me on various equipment and sharing your two cents on how to survive grad school. I want to thank Rachel Miller, Ezen Choo, Charles Lee, Sam Mudgal, and Michael Wagner for your friendship, support, and assistance on research. Deep gratitude also goes to all faculty, staff, and students in the Department of Food Science whom I have come to know in my Cornell years. A special thank you to Janette Robbins and Erin Atkins for all their help. The interdisciplinary nature of my research requires the use of equipment all over Cornell Campus. Thank you to Teresa Porri, Penny Burke, Brian Bowman, Steve Krisk, Malcolm Thomas, and Carol Bayles for their technical support at various stages of my PhD research.

I was lucky to have the opportunity to live in Triphammer Cooperative for four years and get to make many Co-Op friends with whom I share so much wonderful and unforgettable memories that I will always cherish. Thank you to all of the "Triphamsters" who cheered me up during my lows, and shared my excitement and happiness when I made progress in research. In particular, I would like to thank Tianyu Wang for your friendship, support, and the many stimulating conversations (some fun and delightful, others deep and substantial) we have had on a wide range of topics. I would like to thank my current housemates, Xiaopeng Yu and Yi Jiang, for sharing with me your passion in bodybuilding and board games as well as sustainable polymers and 3D imaging data reconstruction.

Most of all, I would like to thank my parents Shujun Yang and Gang Cheng for instilling in me the curiosity and eagerness to discover the unknown and appreciate the beauty of nature, for everything you had to give up to allow me grow to be the person I am, and for your unconditional love and support throughout this journey that kept me strong in those difficult times.

TABLE OF CONTENTS

LIST OF FIGURES

LIST OF TABLES

LIST OF ABBREVIATIONS

AAO	Anodized aluminum oxide
Adj XDLVO	The Adjusted XDLVO theory, the effect of surface topography is considered
AFM	Atomic force microscope
BPB	Butterfield phosphate buffer
CA	Contact angles
CLSM	Confocal laser scanning microscope
DLVO	Derjaguin-Landau-Verwey-Overbeek, a theory named after the four scientists who contribute significantly to its genesis.
EZ	Exclusion zones
EPS	Extracellular polymeric substances
NS	Nanosmooth aluminum oxide
SEM	Scanning electron microscope
pD	Polydopamine
TSB	Tryptic soy broth
TZ	Transition zones

LIST OF SYMBOLS

F_{LW} (U_{LW})	Lifertz-van der Waals interaction force (energy)
F_{EL} (U_{EL})	Electrostatic interaction force (energy)
F_{AB} (U_{AB})	Acid-base interaction force (energy)
$F_{\mathrm{Total}}^{\mathrm{XDLVO}}$ ($U_{\mathrm{Total}}^{\mathrm{XDLVO}}$)	Total interaction force (energy) calculated based on the extended DLVO theory
Adj	Adjusted for surface topography
F_{max}	Maximum total $F_{\mathrm{Total}}^{\mathrm{XDLVO}}$ exerted on a bacterial cell during its process of approaching the solid-liquid interface from infinitely far away
IS	Ionic strength
T	Temperature
γ^-	Electron-donor component of surface energy/tension
γ^+	Electron-acceptor component of surface energy/tension
γ^{LW}	Apolar component of surface energy/tension
λ	Characteristic wavelength of bacteria-surface interaction
λ_1	Characteristic decay of acid-base interactions in water
ϵ	Permittivity of water
k_{B}	Boltzmann constant
C_{e}	The elementary charge
H	Hamaker constant
h	Separation distance between the bottom of a colloidal particle and the surface of a substratum
h_0	Minimum separation between two bodies, which is delimited by the outer electron shells (van der Waals boundaries).
a	Equivalent radius of the bacterium
d	Depth of the cylindrical pores
P	Surface porosity of the substrate

R	Radius of the cylindrical pores
θ_{ij}	Liquid contact angles of liquid i on substrate j
N_{hs}	Number of hemispheres distributed along the circumference of a cylindrical pore per the one-ring model
A_{e}	Effective interaction area between a spherical object and a nanoporous surface
R_{e}	Effective radius, or radius of the effective interaction area
κ^{-1}	Debye length
$\rho_{\infty\,\mathrm{i}}$	Ionic concentration of ion i in bulk solution
z_{i}	Valence of ion i
N_w	Number of cylindrical nanopores that contribute significantly to the repulsive force exerted on a bacterial cell
$\psi_{\mathrm{b}}, \psi_{\mathrm{s}}$	Electric potential at bacteria and substrate surface, respectively

INTRODUCTION

Despite tremendous efforts made to reduce foodborne illnesses by improving safety in the food supply chain, recent data shows that foodborne illnesses continue to be a significant concern in the United States and worldwide[1–3]. The Centers for Disease Control and Prevention (CDC) recently estimated that each year roughly 1 in 6 Americans (or 48 million people) get sick, 128,000 are hospitalized, and 3,000 die of foodborne diseases[3]. In addition to the adverse consequences on public wellness, foodborne illnesses also impose a huge economic burden on society. According to a recent conducted by Scharff in 2011, the aggregated annual cost of foodborne illness was $77.7 billion and the average cost per case of foodborne illness was $1,626[1].

Most of the microbial contamination problems in the food industry are caused by the transfer of microorganisms from food contact surfaces and processing equipment to the foods themselves [4]. Often times, in order to survive under various stresses from the environment (e.g. low water activity), microbial species tend to co-colonize surfaces they come in contact with and form biofilms, where individual cells are interconnected and are enclosed in a matrix consisting of extracellular polymeric substances (EPS). Studies have shown that microbial cells living in biofilms demonstrate altered gene expression[5], increased production of EPS [6], and enhanced resistance to sanitizers, disinfectants and antimicrobial agents [7]. Adhesion of spoilage or pathogenic microorganisms to surfaces and the formation of biofilms impose persisting risk of microbial contamination of processed food products. In addition to being a potential source of contamination, biofilms can also accelerate the corrosion of material surfaces, interfere with heat transfer, and increase fluid frictional resistance[4], all of which raise the operating costs by a large amount and should therefore be averted.

Currently, the most widely adopted method for removing biofilms in food processing facilities is the Cleaning-In-Place (CIP) procedure, which employs sequential treatment with heated acid and/or alkali and antimicrobial sanitizers along with turbulent flow, so as to both chemically and physically remove biofouling [4]. While planktonic cells can be effectively removed by physical means (e.g. water turbulence or scrubbing) and/or killed by chemical sanitizers, they become more resistant to conventional cleaning methods once they form biofilms, largely due to the protection conferred by EPS and biomass in the outer shell of the biofilm [8]. Another issue associated with CIP is that, despite the water flush at the end of the cleaning protocol to remove the CIP chemicals, some residues may enter food products, potentially impairing food quality and jeopardizing consumer health. Additionally, CIP waste streams demand expensive treatment before they can be released to the environment[9], which further increases operating costs in the food industry.

All these disadvantages and limitations associated with CIP, which only provides a *posthoc* fix, highlight the critical need for preventative strategies to alleviate biofouling. Recently, antifouling and fouling-release materials, capable of limiting biofilm formation by providing resistance against initial attachment and weakening cell-surface binding, have emerged as a promising solution to biofilm-associated problems in various environments, such as food processing environment[10], surfaces of biomedical device[11], wastewater treatment plants[12], and shipping industry [13].

Attachment of bacteria to nanostructured surfaces is significantly different from attachment on bulk or microstructured materials.[14] Explanations of this behavior allude to the fact that nano-structuring induces significant changes in surface charge and surface free energy, which affect attachment and biofilm formation.[15] There is, therefore, a great opportunity to design

nanostructured materials able to effectively repel microorganisms. Unfortunately, most nanostructuring methods are expensive, which renders the approach prohibitively expensive for many applications. Nanostructured surfaces can also be extremely delicate and incompatible with the cleaning procedures used in industrial or medical applications.

Compared to other nanofabrication methods, anodization is a widely available surface treatment that produces an oxide which, under well-controlled conditions, exhibits a nanoporous structure, is chemically inert to many cleaning agents, and has excellent wearing properties. Anodization is used on an industrial scale and can be applied to large surface areas and three-dimensional parts. Aluminum anodization, in particular, is a widely used process, with countless industrial applications.[16] By controlling the anodizing voltage and bath composition, Al anodization produces cylindrical, parallel pores oriented perpendicular to the surface, of defined pore diameter and surface porosity.[17,18]

Nonetheless, despite the rapid development of antifouling materials and micro/nano-fabrication technologies in the past decade, we still lack a systematic understanding of the mechanisms by which these antifouling materials resist adhesion by microorganisms. Collectively, the scientific community has identified some key factors that govern the attachment of particulates (including microorganisms) to surfaces. These include, among others, electric double layer and charge density [19,20], surface hydrophobicity and surface free energy [21,22], roughness and surface topography [23], environmental factors and biological factors [23]. Notwithstanding the relatively extensive literature coverage of each of these key factors, a consensus on the effect of these factors on fouling has yet to be reached. For example, two of the most debated factors are roughness[24] and hydrophobicity/hydrophilicity[25]. There is some evidence supporting that the propensity of bacterial attachment onto a surface increases with surface roughness[26], whereas others have shown

the opposite[27,28]. Likewise, as for hydrophobicity/hydrophilicity, Hook *et al.* [29] found no correlation between bacterial attachment and water contact angle for 496 polymeric materials, even though other researchers have suggested that superhydrophobic (water contact angle > 150°) or superhydrophilic (water contact angle < 10°) materials can mitigate biofouling[30]. Besides better clarifying these influences, we also need to improve our understanding of some of these factors to a quantitative level, which will allow us to accurately predict the tendency of fouling, and eventually to design "tailored" antifouling surface for specific systems.

My Ph.D. research is aimed at understanding the bacterial attachment trend observed on nanostructured anodic aluminum oxide (AAO) surfaces, using a combination of theoretical modeling and experimental approaches. First, I built upon the extended Dejaguin-Landau-Verwey-Overbeek (XDLVO) model and added in topographical parameters that enable the calculation of total force exerted on a bacterial cell by nanoporous AAO surfaces (Chapter One). A significant negative correlation was found between the theoretical force predictions and the biomass accumulation on various nanoporous AAO surfaces, which validates the usefulness of the adjusted XDLVO model for explaining the effect of nanoscale topography on bacterial attachment – the details are described in the first part of Chapter Two. Despite the proven effectiveness of the model, the magnitude of the interaction forces predicted by the adjusted XDLVO model should also be verified to further substantiate the model – the second part of Chapter Two is devoted to verifying the predicted force-distance plots with single-cell force spectroscopy. In Chapter Three, the nanoporous AAO surfaces were challenged with bacterial pathogens implicated in illness associated with food and clinic settings, and the adjusted XDLVO model was applied to explain the attachment by an even wider range of bacterial strains on AAO surfaces. The model can also be used as a predictive tool for selecting or engineering desired topographical and surface energy

traits for more effective bacteria-repellent antifouling materials tailored to specific applications (Chapter Three). Chapter Four investigates a long-range exclusion phenomenon mostly found at the solid-liquid interface of hydrophilic materials. The implications of this remarkable exclusion phenomenon for the understanding of bacterial attachment are also discussed in this chapter.

REFERENCES

(1) Scharff, R. L. Economic Burden from Health Losses due to Foodborne Illness in the United States. *J. Food. Prot.* **2012**, *75* (1), 123–131.

(2) Hoffmann, S.; Batz, M. B.; Morris, J. G. Annual Cost of Illness and Quality-Adjusted Life Year Losses in the United States due to 14 Foodborne Pathogens. *J. Food Prot.* **2012**, *75* (7), 1292–1302.

(3) Scallan, E.; Hoekstra, R. M.; Angulo, F. J.; Tauxe, R. V.; Widdowson, M.-A.; Roy, S. L.; Jones, J. L.; Griffin, P. M. Foodborne Illness Acquired in the United States—Major Pathogens. *Emerg. Infect. Dis.* **2011**, *17* (1), 7–15.

(4) Kumar, C. G.; Anand, S. . Significance of Microbial Biofilms in Food Industry: A Review. *Int. J. Food Microbiol.* **1998**, *42* (1–2), 9–27.

(5) Donlan, R. M. Biofilms: Microbial Life on Surfaces. *Emerg. Infect. Dis.* **2002**, *8* (9), 881–890.

(6) Sutherland, I. W. Biofilm Exopolysaccharides: A Strong and Sticky Framework. *Microbiology* **2001**, *147* (1), 3–9.

(7) Robbins, J. B.; Fisher, C. W.; Moltz, A. G.; Martin, S. E. Elimination of Listeria Monocytogenes Biofilms by Ozone, Chlorine, and Hydrogen Peroxide.

(8) Chmielewski, R. a. N.; Frank, J. F. Biofilm Formation and Control in Food Processing Facilities. *Compr. Rev. Food Sci. Food Saf.* **2003**, *2* (1), 22–32.

(9) Lin, S. H.; Lin, C. M.; Leu, H. G. Operating Characteristics and Kinetic Studies of Surfactant Wastewater Treatment by Fenton Oxidation. *Water Res.* **1999**, *33* (7), 1735–1741.

(10) Bansal, B.; Chen, X. A Critical Review of Milk Fouling in Heat ExchangersFinnis, Chera M. *Group* **2006**, *5* (2), 27–33.

(11) Desrousseaux, C.; Sautou, V.; Descamps, S.; Traoré, O. Modification of the Surfaces of Medical Devices to Prevent Microbial Adhesion and Biofilm Formation. *J. Hosp. Infect.* **2013**, *85* (2), 87–93.

(12) Chen, W.; Su, Y.; Peng, J.; Zhao, X.; Jiang, Z.; Dong, Y.; Zhang, Y.; Liang, Y.; Liu, J. Efficient Wastewater Treatment by Membranes through Constructing Tunable Antifouling Membrane Surfaces. *Environ. Sci. Technol.* **2011**, *45* (15), 6545–6552.

(13) Yebra, D. M.; Kiil, S.; Dam-Johansen, K. Antifouling Technology - Past, Present and Future Steps towards Efficient and Environmentally Friendly Antifouling Coatings. *Prog. Org. Coatings* **2004**, *50* (2), 75–104.

(14) Puckett, S. D.; Taylor, E.; Raimondo, T.; Webster, T. J. The Relationship between the Nanostructure of Titanium Surfaces and Bacterial Attachment. *Biomaterials* **2010**, *31* (4), 706–713.

(15) Hori, K.; Matsumoto, S. Bacterial Adhesion: From Mechanism to Control. *Biochem. Eng. J.* **2010**, *48* (3), 424–434.

(16) Thomas, P.; Benaben, P. Preparation of Highly Ordered Nanoporous Alumina by Two Step Anodising: Process and Industrial Applications. *Trans. Inst. Met. Finish.* **2007**, *85* (4), 212–216.

(17) Jessensky, O.; Müller, F.; Gösele, U. Self-Organized Formation of Hexagonal Pore Arrays in Anodic Alumina. *Appl. Phys. Lett.* **1998**, *72* (10), 1173.

(18) Masuda, H.; Yada, K.; Osaka, A. Self-Ordering of Cell Configuration of Anodic Porous Alumina with Large-Size Pores in Phosphoric Acid Solution. *Jpn. J. Appl. Phys.* **1998**, *37* (11A), L1340–L1342.

(19) Camesano, T. a.; Logan, B. E. Probing Bacterial Electrosteric Interactions Using Atomic Force Microscopy. *Environ. Sci. Technol.* **2000**, *34* (16), 3354–3362.

(20) Pranzetti, A.; Mieszkin, S.; Iqbal, P.; Rawson, F. J.; Callow, M. E.; Callow, J. a; Koelsch, P.; Preece, J. a; Mendes, P. M. An Electrically Reversible Switchable Surface to Control and Study Early Bacterial Adhesion Dynamics in Real-Time. *Adv. Mater.* **2013**, *25* (15), 2181–2185.

(21) Bos, R.; Van Der Mei, H. C.; Gold, J.; Busscher, H. J. Retention of Bacteria on a Substratum Surface with Micro-Patterned Hydrophobicity. *FEMS Microbiol. Lett.* **2000**, *189*, 311–315.

(22) White, J. S.; Walker, G. M. Influence of Cell Surface Characteristics on Adhesion of Saccharomyces Cerevisiae to the Biomaterial Hydroxylapatite. *Antonie Van Leeuwenhoek* **2011**, *99* (2), 201–209.

(23) Feng, G.; Cheng, Y.; Wang, S.; Hsu, L. C.; Feliz, Y.; Borca-Tasciuc, D. a.; Worobo, R. W.; Moraru, C. I. Alumina Surfaces with Nanoscale Topography Reduce Attachment and Biofilm Formation by Escherichia Coli and Listeria Spp. *Biofouling* **2014**, *30* (November), 1253–1268.

(24) Mitik-Dineva, N.; Wang, J.; Truong, V. K.; Stoddart, P.; Malherbe, F.; Crawford, R. J.; Ivanova, E. P. Escherichia Coli, Pseudomonas Aeruginosa, and Staphylococcus Aureus Attachment Patterns on Glass Surfaces with Nanoscale Roughness. *Curr. Microbiol.* **2009**, *58* (3), 268–273.

(25) Bowen, W. R.; Lovitt, R. W.; Wright, C. J. Atomic Force Microscopy Study of the Adhesion of Saccharomyces Cerevisiae. *J. Colloid Interface Sci.* **2001**, *237* (1), 54–61.

(26) Rimondini, L.; Farè, S.; Brambilla, E.; Felloni, a; Consonni, C.; Brossa, F.; Carrassi, a. The Effect of Surface Roughness on Early in Vivo Plaque Colonization on Titanium. *J. Periodontol.* **1997**, *68* (6), 556–562.

(27) Hsu, L.; Fang, J.; Borca-Tasciuc, D.; Worobo, R.; Moraru, C. I. The Effect of Micro- and Nanoscale Topography on the Adhesion of Bacterial Cells to Solid Surfaces. *Appl. Environ. Microbiol.* **2013**.

(28) Singh, A. V.; Vyas, V.; Patil, R.; Sharma, V.; Scopelliti, P. E.; Bongiorno, G.; Podestà, A.; Lenardi, C.; Gade, W. N.; Milani, P. Quantitative Characterization of the Influence of the Nanoscale Morphology of Nanostructured Surfaces on Bacterial Adhesion and Biofilm Formation. *PLoS One* **2011**, *6* (9), e25029.

(29) Hook, A. L.; Chang, C.-Y.; Yang, J.; Luckett, J.; Cockayne, A.; Atkinson, S.; Mei, Y.; Bayston, R.;

Irvine, D. J.; Langer, R.; et al. Combinatorial Discovery of Polymers Resistant to Bacterial Attachment. *Nat. Biotechnol.* **2012**, *30* (9), 868–875.

(30) Li, Z.; Wu, C.; Zhao, K.; Peng, B.; Deng, Z. Polydopamine-Assisted Synthesis of Raspberry-like Nanocomposite Particles for Superhydrophobic and Superoleophilic Surfaces. *Colloids Surfaces A Physicochem. Eng. Asp.* **2015**, *470*, 80–91.

JUSTIFICAITON AND OBJECTIVES OF THIS RESEARCH

Objective 1 - Develop a mathematical model to quantitatively describe the physicochemical forces exerted by nanostructured surfaces on bacterial cells

Justification: Bacteria-surface interaction is governed by the interplay between biological factors and physicochemical factors. A quantitative prediction of bacteria–surface interaction forces is needed to understand the tendency of attachment by various strains on a wide range of surfaces. The extended Derjaguin-Landau-Verwey-Overbeek model (extended DLVO or XDLVO model for short) was developed to explain the interaction between spherical objects and an *ideal* surface, however most natural and artificial objects bear surface micro- or nanoscale features on their surfaces, which are not accounted for by the XDLVO model in its existing form. In order to directly verify the theoretical predictions generated by the model, the force-distance trajectory of a microsphere over various nanostructured surfaces should be recorded with force spectroscopy and compared with model predictions.

Objective 2 – Validate the model predictions with bacterial attachment assays conducted at various time scales

Justification: Validation of the model predictions with bacterial attachment assay is necessary for ensuring the accuracy and usefulness of the model.

Objective 3 – Apply the model to bacterial attachment and biofilm formation by various pathogenic bacteria on a series of nanostructured surfaces, and use the model to build a roadmap for identifying or engineering effective antifouling materials

Justification: The nanostructured AAO surfaces need to be challenged with pathogenic bacteria of a variety of physiological and physicochemical properties to demonstrate its applicability in real life situations. The adjusted XDLVO model allows the expression of total interaction force as a function of tunable material surface parameters including electrostatic, surface energy, and surface topography. With the help of the adjusted XDLVO model, it is feasible to develop an efficient and systematic algorithm to further optimizing surface topographical features and physicochemical properties, and thus create surfaces with a stronger ability to prevent bacterial attachment and biofilm formation.

Objective 4 – Develop a quantitative confocal microscopy technique to visualize and analyze bacterial cell density distribution near liquid-solid interfaces, study the bacteria-exclusion phenomenon near hydrophilic materials, and investigate the effect of surface topography on the size of exclusion zones and transition zones.

Justification: Hydrophilic surfaces of both an abiotic and biological origin have been found to bear particle-exclusion zones (EZ) as large as hundreds of micrometers above fluid-solid interfaces. While the mechanism for EZ formation is still debated, its unique long-range particle-repellent property may hold promise for the development of antifouling surfaces.

CHAPTER ONE

MODELLING THE INTERACTION BETWEEN A BACTERIAL CELL AND NANOSTRUCTURED SURFACES

1.1. Abstract

A comprehensive mathematical model was developed to obtain mechanistic understanding of bacterial attachment on nanostructured surfaces. The force components of the extended DLVO theory - the van de Waals, electrostatic, and acid-base forces - were integrated over the nanoscale cylindrical pores in the anodized aluminum oxide (AAO) surfaces, which allowed the computation of the total interaction force ($F_{\mathrm{Total}}^{\mathrm{XDLVO}}$) and the maximum repulsive force barrier ($F_{\max}$) as a function of pore diameter, pore depth, surface porosity. The model predictions revealed that the smaller pore surfaces (i.e. 15 nm and 25 nm pore AAO) exert greater repulsive $F_{\max}$ on the approaching bacterial cell than the larger pore surfaces as well as the nanosmooth control. The predictions were substantiated by the actual force-distance curves generated by atomic force microscopy. The adjust XDLVO model can serve as a powerful tool for explaining and predicting bacterial attachment on nano-engineered AAO surfaces.

1.2. Introduction

Bacteria attachment and subsequent biofilm formation are affected by numerous factors including physical and chemical properties of the contact surface, composition and temperature of the environment, bacteria cell physiology and cell surface properties. The interaction of bacteria cells with solid substrates has been explained before using the thermodynamic theory, which considers the effect of surface energy, and the classical Derjaguin and Landau, Verwey and Overbeek (DLVO) theory, which accounts for the effect of both surface energy and surface charge on the cell-substratum interactions [1–3].

The thermodynamic theory and many experimental observations indicate that surface free energy of the substratum influences both the strength and reversibility of bacteria adhesion [4]. The relationship between surface free energy and relative bacterial adhesion is frequently illustrated by the "Baier curve" (Figure 1), which shows that the number of bacteria attached to solid surfaces reaches a minimum at a surface energy of about 25 mN/m [5]. This relationship was first reported in 1973 for biofouling in marine applications and has also been found to hold for microorganisms and contaminants specific to food processing [4,6,7]. The existence of this minimum is well documented in literature, both for bacteria contaminants including *E. coli, Listeria* and *P. aeruginosa* [6,8,9], as well as for organic matter.[10] Despite its success in identifying "the universal minimum in biological stick-to-itiveness" as between 20 and 30 mJ/m^2, Baier curve is constructed based entirely on empirical observations; a more rigorous derivation of this low-fouling surface energy region from first principles is needed. In Chapter Three, the Baier curve will be substantiated with a quantitative predictive tool derived from the XDLVO model, "the $F_{\max}$ Cloud", in three-dimensional surface energy space.

Another thermodynamic approach compares the surface free energy before and after bacterial adhesion, and the total free energy change occurred during the adhesion process is expressed in the so-called free energy of adhesion (ΔG_{adh})[11,12]. A negative ΔG_{adh} value indicates that bacterial adhesion lowers the total free energy of the system, and therefore the adhesion event is likely to occur because it is thermodynamically favorable; conversely, if the adhesion of a certain bacterial cell onto a surface gives rise to a positive ΔG_{adh} value, the process is thus thermodynamically unfavorable, and the substrate surface will appear antifouling against this particular strain.

However, there are two limitations associated with the thermodynamic model: 1) it fails to take into account the interaction between the electric double layer of the cell and the material surface; 2) it only considers the initial and final energy states but neglects the critical role of energy barriers during the attachment process. In some cases, the formation of a new cell-substratum interface, at the expense of the cell-liquid and liquid-substratum interfaces, is thermodynamically favorable, but kinetically too slow to be practical, due to a huge energy barrier opposing the attachment process.

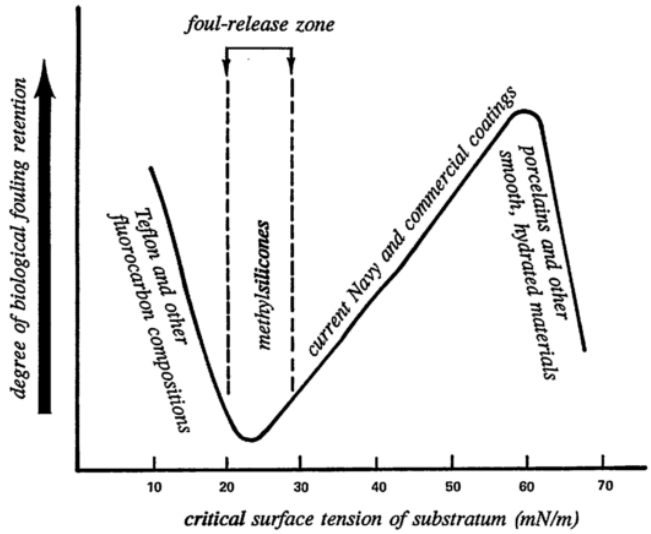

Figure 1. The Baier curve, which shows the empirical relationship between critical substratum surface tension and biomass accumulation on such surface (Source: Baier [13]).

Bacterium-surface interaction is also described by the DLVO theory [14], according to which the total interaction between a surface and a bacterium cell is the sum of Lifertz-van der Waals attractive forces and electrostatic Coulomb interactions. The van der Waals forces are dominant in the vicinity of the surface but decrease sharply with separation distance h as h^{-3}, while the Coulomb interactions become dominant further away from the surface [15]. Bacteria and natural surfaces in aqueous solutions are usually negatively charged, as was the case both for the surfaces and cells

used in the current study. This gives rise to a repulsive electrostatic energy that increases as the ionic strength of the surrounding aqueous medium decreases [16]. At low ionic strength, when a bacterial cell approaches a surface it encounters an energy barrier that cannot be overcome solely by motility or Brownian motion; at high ionic strength, this energy barrier vanishes and bacterial cells can easily approach the surface and adhere irreversibly [15,17–20]. The DLVO theory was later modified by van Oss into the extended DLVO (XDLVO) theory [21]. The XDLVO theory accounts for both interactions described above, as well as for hydration forces and the hydrophobic/ hydrophilic forces between bacteria and the surface, which are summarized as acid-base interaction forces [21]. The acid-base interaction forces are dominant in the short-range, but they diminish exponentially in magnitude as the separation distance increases [21]. The total interaction force between the surface and the bacterium, $F_{\mathrm{Total}}^{\mathrm{XDLVO}}$, can be calculated as the sum of the Lifertz-van der Waals attraction (F_{LW}), the acid-base interaction (F_{AB}) and the electrostatic repulsion (F_{EL}) [22]. These three XDLVO component forces and their respective physical mechanisms are summarized in Figure 2.

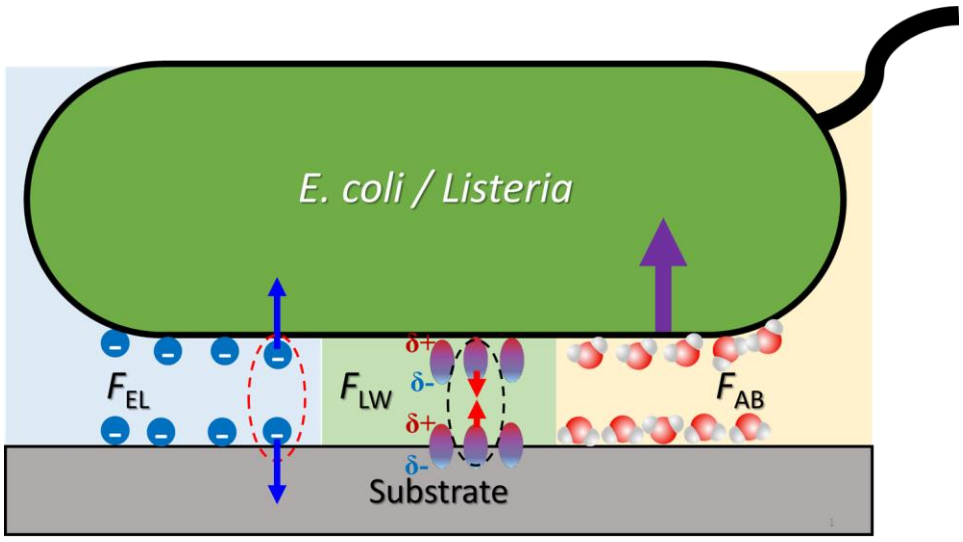

Figure 2. Schematic representation of the physicochemical forces exerted on a typical bacterial cell by a substrate. F_{EL}: electrostatic interaction, F_{LW}: Lifertz-van der Waals interaction, and F_{AB} acid-base interaction. In the case of an *E. coli* ATCC 25922 (or *L. innocua* cell) interacting with an alumina substrate, the directions of the forces are as shown above.

In general, the LW interactions are attractive, whereas the EL interactions can be attractive or repulsive, depending on the sign of electrical charges on the substrate and bacteria, respectively. The AB interactions are based on electron acceptor/electron donor interactions between polar moieties. Depending on the polarity, or the hydrophobic-hydrophilic properties, these interactions can be attractive (hydrophobic attraction) or repulsive (hydrophilic repulsion or hydration effects), and their magnitude may be up to ten-, or even a hundred-fold greater than that of EL and LW.[23,24] Nonetheless, despite its critical role in cell-surface interaction, the physics behind AB interactions is less understood, and the reason for their significant contribution to attachment has yet to be elucidated.

Compared with the above-mentioned thermodynamic approach, the XDLVO theory is more comprehensive because it accounts for electrostatic interactions and the properties of the

bacteria cells, as well as the force (or energy) barriers involved in the attachment process. Sharma and Rao[25] studied the bacterial adhesion to pyrite (FeS_2) under different physicochemical conditions (ionic strength and pH) and compared the experimental results with the predictions by XDLVO and the surface thermodynamics approaches. They found that in general, the XDLVO approach explains more effectively the attachment of bacteria–bacteria, mineral–mineral or mineral–bacteria systems than the thermodynamic approach.

Inspired by the promising results of the XDLVO modeling approach in literature, in the present study the XDLVO theory is selected for modeling the interaction between bacteria and the nanoporous anodic aluminum oxide (AAO) surfaces. To correctly model the interaction between the AAO surfaces and bacterial cells the classical XDLVO model had to be adjusted to account for the effect of surface topography on the interaction forces.

1.3. Model Development

1.3.1. Geometry of anodized aluminum oxide

Nanoporous aluminum oxide surfaces with pore diameters of 15 nm, 25 nm, 50 nm and 100 nm were prepared by two-step anodization of high purity aluminum substrate using a procedure that will be described in the next chapter.

In order to generate a simplified but representative model for anodic alumina surfaces, the surface topography AAO was inspected by scanning electron microscopy (SEM). Figure 3a shows an example of a typical cross-section of the anodized layer, comprising ordered cylindrical pore arrays perpendicular to the surface. Based on this characteristic feature of the anodic layer, the surface topography was treated as cylindrical pores uniformly distributed across the surface, with pore diameter, pore depth, and surface porosity as the key surface topography descriptors (Figure

3b). A typical top-down SEM image of each anodized surfaces and a commercial nanosmooth alumina surface are shown in Figure 3c. It should be noted that a cylindrical pore model is a more accurate depiction of the 15 nm and 25 nm pore surfaces than the 50 nm and 100 nm pore surfaces, due to the irregularity in the pore shape of the larger pore surfaces. Nonetheless, since no significant departure from a circular shape was detected in the cross section of the larger pores, the cylindrical pore model should produce acceptable results. No surface feature was observed on the nanosmooth alumina surfaces at the magnification used for the anodized surfaces, which validated its use as a smooth control surface for this study.

Another thing that is worth commenting on is the presence of a network of pores linked by narrow bridges (indicated by their darker color) underneath the surface of the 50 nm and 100 nm pore surfaces (Figure 3c). This secondary structure was not included in the model because its impact on total interaction forces was negligible due to its small surface area and relatively far position from the surface layer.

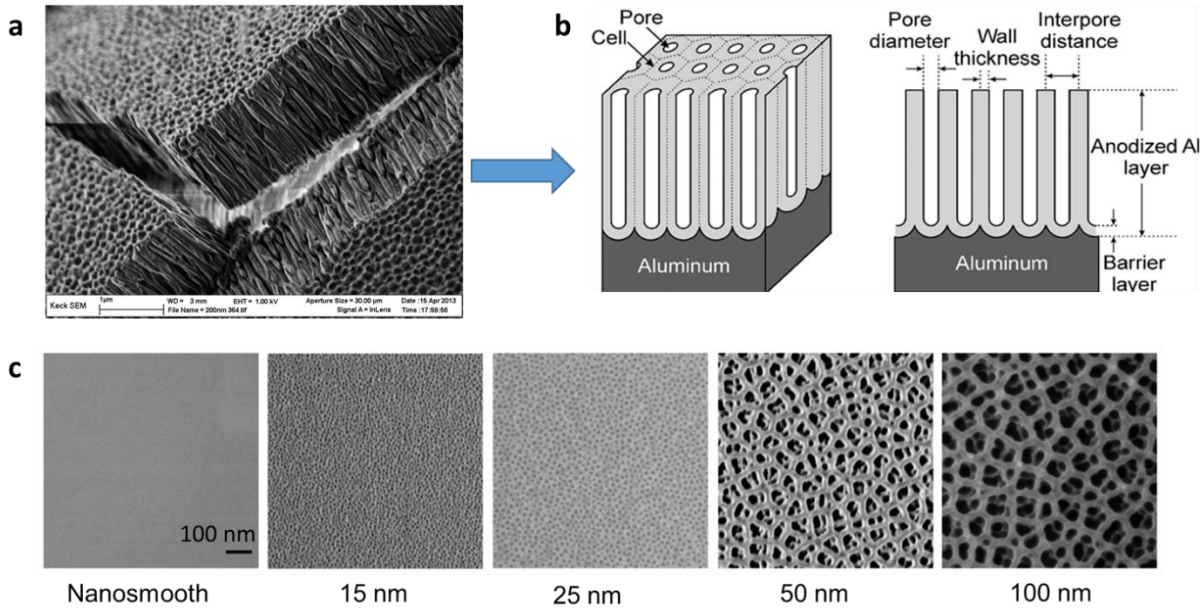

Figure 3. Surface topography of the anodized aluminum oxide substrates and its simplified model. **(a)** a SEM image featuring the surface topography as well as the cross-sectional structure of a typical AAO surface; **(b)** a simplified model capturing the characteristic cylindrical pores of the AAO surfaces; **(c)** representative SEM images of all alumina surfaces used in this study.

To verify the average pore size of each anodized nanoporous surface, the images in Figure 3c were converted to binary images using ImageJ and then subjected to the "Analyze Particles" function of ImageJ. The histograms for the pore diameter distribution of each anodized surface are presented in Figure 4. The average pore diameter of 15 nm, 25 nm, 50 nm, and 100 nm pore surface was 15.0 ± 3.1 nm (average ± standard error of means), 24.6 ± 8.4 nm, 46.9 ± 22.3 nm, and 95.9 ± 42.7 nm, respectively. Note that the variance in pore diameter of the 50 nm and 100 nm pore surface is larger than that of the 15 nm and 25 nm surfaces, and their size distribution is not Gaussian.

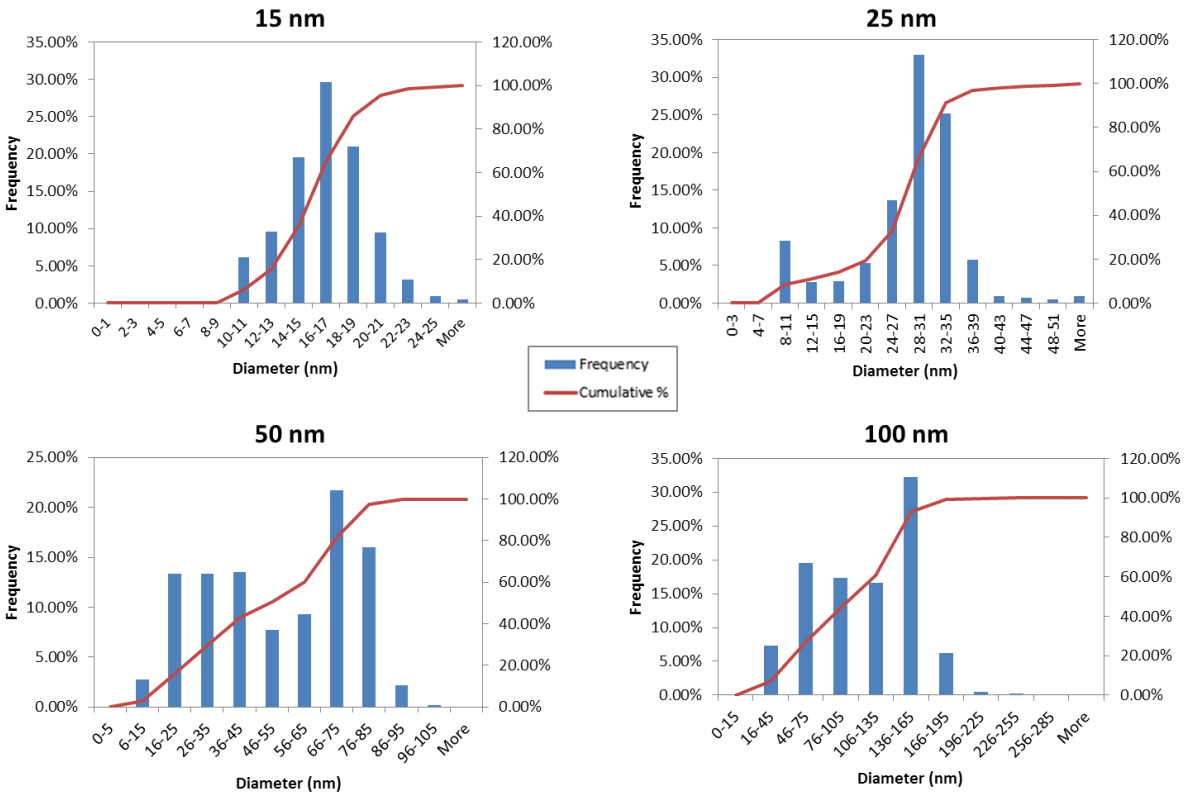

Figure 4. Histograms for the pore diameter distribution of each type of the AAO surfaces. The blue bars indicate percent frequency and the red line indicate cumulative percentage.

1.3.2. Development of the adjusted XDLVO model

The XDLVO theory is employed here as the foundation of a physicochemical model that describes the interaction forces between the nanostructured substratum and a bacterium cell. The total energy needed to bring a bacterium from an infinite distance to a surface is given by [22] :

$$U_{\mathrm{Total}}^{\mathrm{XDLVO}} = U_{\mathrm{LW}}^{\mathrm{Adj}} + U_{\mathrm{AB}}^{\mathrm{Adj}} + U_{\mathrm{EL}}^{\mathrm{Adj}} \quad (1)$$

The forces associated with these energies are:

$$F_{\mathrm{Total}}^{\mathrm{XDLVO}} = F_{\mathrm{LW}}^{\mathrm{Adj}} + F_{\mathrm{AB}}^{\mathrm{Adj}} + F_{\mathrm{EL}}^{\mathrm{Adj}} \quad (2)$$

where $F_{\mathrm{LW}}^{\mathrm{Adj}}$ represents the Lifertz-van der Waals attraction forces, $F_{\mathrm{AB}}^{\mathrm{Adj}}$ the acid-base interaction forces and, $F_{\mathrm{EL}}^{\mathrm{Adj}}$ the electrostatic repulsive forces.

Since the original XDLVO theory is based on the assumption of ideally smooth surfaces [26], "adjusted" (Adj) values of the component forces were calculated, taking into consideration the nanoporous structure of the surfaces used in this work. Contributions from the vertical surfaces and the bottoms of the cylindrical pores were also considered.

Moreover, a few simplifying assumptions were made: *(i) E. coli* ATCC 25922 and *L. innocua* cells were assumed to have a spherical shape of equivalent radius of 317 nm and 492 nm, respectively (these values measured previously for the same strains, under similar environmental conditions)[27]; *(ii)* surfaces were considered to have a fully wetting (Wenzel) behavior[28] ; and *(iii)* each surface was assumed to be an infinite planar surface relative to the dimension of a bacterial cell. The bacteria adhesion test was performed in tryptic soy broth (TSB), approximated to be a 1:1 type electrolyte solution of ionic strength IS = 0.1 M, at pH 7 and T = 310 K. The constants appearing in the expressions for energy, including the Hamaker constant, the characteristic wavelength of cell-surface interactions, the constants for the Lifshitz-van der Waals and acid–base interactions, and surface zeta potential of pure alumina were taken from literature [22,26,29–31]. The values of these constants and their sources are provided in Table 1.

The pore depth and radius, surface porosity and the diameters of the bacteria cells were all determined from SEM images; the zeta potential values of the bacterial cells were determined experimentally (Table 2).

Table 1. Values of the constants used for calculating bacteria-surface interaction forces

Symbols	Parameters / constants	Values	Source
λ	Characteristic wavelength of bacteria-surface interaction	100 nm	Gregory 1981 [29]
λ_1	Characteristic decay of acid-base interactions in water	0.6 nm	Bhattacharjee *et al.* 1996 [26]
ϵ	Permittivity of water	$80\times8.8854\times10^{-12}$ (C^2 J^{-1} m^{-1})	
h_0	Minimum separation between two bodies	0.158 nm	Bhattacharjee *et al.* 1996 [26]
k_B	Boltzmann constant	1.38×10^{23} (J K^{-1})	
C_e	The elementary charge	1.602×10^{-19} C	
γ	Surface tension of water, glycerol, diiodomethane	*(multiple values)*	Li *et al.* 2004 [22]

Table 2. Values of the geometrical parameters of the AAO surfaces

Anodic Alumina Type (Pore Size)	Porosity*	Pore Depth* (nm)
15 nm	0.176	2559
25 nm	0.260	875
50 nm	0.310	1189
100 nm	0.306	1406

* Measured values

The three interaction forces exerted on a bacterial cell by a nanostructured substratum was calculated as follows:

1) The Lifertz-van der Waals energy of attraction between the cells and the surfaces, assumed as infinite planar surfaces, and was calculated using the retarded Hamaker expression:

$$U_{\mathrm{LW}}(h,d) = \frac{-H\,a}{6(h+d)[1+14(h+d)/\lambda]} \qquad (3)$$

where *H* is the Hamaker constant, *a* the bacteria radius, *h* is the separation distance between the bacterium and the surface, *d* is the depth of cylindrical wells and λ the characteristic wavelength of interaction between the bacteria and the surfaces.

The Hamaker constant is given by:

$$H = -12\pi\, {h_0}^2\, \Delta G_{\mathrm{LW}} \qquad (4)$$

The interaction energy per unit area, ΔG_{LW}, between the bacterium and the surface, at the minimum separation distance h_0, is:

$$\Delta G_{\mathrm{LW}} = 2(\sqrt{\gamma_{\mathrm{w}}^{\mathrm{LW}}} - \sqrt{\gamma_{\mathrm{s}}^{\mathrm{LW}}})(\sqrt{\gamma_{\mathrm{b}}^{\mathrm{LW}}} - \sqrt{\gamma_{\mathrm{w}}^{\mathrm{LW}}}) \quad (5)$$

where superscript "LW" indicates the non-polar component of surface tension, and subscripts "w", "b", and "s" denote water, bacterium, and substrate, respectively.

After adjusting for the presence of nanopores in the substrate, Eq. (2) becomes:

$$U_{\mathrm{LW}}^{\mathrm{Adj}}(h, d, P) = P * U_{\mathrm{LW}}(h, d) + (1 - P) * U_{\mathrm{LW}}(h, 0) \quad (6)$$

where P is the porosity of the surface ($P = Area_{\mathrm{pores}}/Area_{\mathrm{total}}$).

The adjusted Lifertz-van der Waals force of attraction is then calculated as:

$$F_{\mathrm{LW}}^{\mathrm{Adj}} = -\frac{\partial U_{\mathrm{LW}}^{\mathrm{Adj}}}{\partial h} \quad (7)$$

2) The acid-base interaction between a sphere and infinite planar surface:

$$U_{\mathrm{AB}}(h, d) = 2\pi\, a\, \lambda_1 \Delta G_{\mathrm{AB}}\, e^{\left(\frac{h_0 - (h+d)}{\lambda_1}\right)} \quad (8)$$

$$\Delta G_{\mathrm{AB}} = 2\sqrt{\gamma_{\mathrm{w}}^{+}}\left(\sqrt{\gamma_{\mathrm{s}}^{-}} + \sqrt{\gamma_{\mathrm{b}}^{-}} - \sqrt{\gamma_{\mathrm{w}}^{-}}\right) + 2\sqrt{\gamma_{\mathrm{w}}^{-}}(\sqrt{\gamma_{\mathrm{s}}^{+}} + \sqrt{\gamma_{\mathrm{b}}^{+}} - \sqrt{\gamma_{\mathrm{w}}^{+}}) - 2(\sqrt{\gamma_{\mathrm{s}}^{+}\,\gamma_{\mathrm{b}}^{-}} + \sqrt{\gamma_{\mathrm{b}}^{+}\,\gamma_{\mathrm{s}}^{-}}) \quad (9)$$

where superscript "+" indicates the electron acceptor and "−" the electron donor.

According to van Oss [21], the contact angles of the three probe liquids (water, diiodomethane, and glycerol) on bacterial cells and nanosmooth alumina can be used to determine the surface energy parameters used in Eq. 9 by applying the extended Young equation:

$$(1 + cos\theta_{ij})\gamma_j^{\mathrm{total}} = 2\left(\sqrt{\gamma_i^{\mathrm{LW}}\,\gamma_j^{\mathrm{LW}}} + \sqrt{\gamma_i^{+}\,\gamma_j^{-}} + \sqrt{\gamma_i^{-}\,\gamma_j^{+}}\right) \quad (10)$$

The measured contact angle values used for calculating the polar and non-polar components of the surface energies are provided in Table 2. The contact angles measured on nanosmooth alumina surface are comparable to values found in literature [22,32]. The surface tensions of the three probe solutions, denoted by γ_j's, are known constants [21,33].

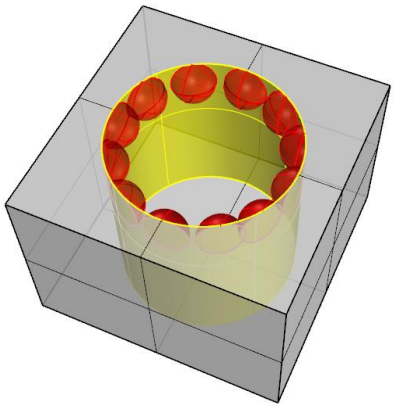

Figure 5. The impact of the vertical surface of the cylindrical wall on acid-base interaction was approximated by a ring of hemisphere distributed alongside the circumference, tangent to the substrate surface.

$U_{\mathrm{AB}}(h,d)$ was modified to account for the contribution of the vertical surface of the cylindrical nanopores. Because the acid-base interactions are short-ranged interactions, it was considered that only the very top rim of the vertical surface of the cylindrical nanopores (within 2 nm from the surface) provides additional contribution to the acid-base interaction. This portion of the internal surface of the cylindrical pores was approximated as a ring of N_{hs} number of hemispheres distributed uniformly along the circumference (Figure 5). The acid-base interaction energy between all these spheres (from *one* cylindrical pore) and the bacterium cell above it, $U_{\mathrm{AB}}^{\mathrm{ms}}(h,d)$ (the superscript "ms" denotes multi-sphere), was calculated by multiplying the

number of hemispheres per pore and the interaction energy of one single hemisphere and the bacterial cell according to Van Oss [21].

$$U_{\mathrm{AB}}^{\mathrm{ms}}(h,d) = N_{\mathrm{hs}} \cdot \frac{1}{2} U_{\mathrm{AB}}^{\mathrm{ss}}(h,d) = \pi^2 \lambda_1 \Delta G_{\mathrm{AB}} \, e^{\left(\frac{h_0 - h}{\lambda_1}\right)} \tag{11}$$

where $U_{\mathrm{AB}}^{\mathrm{ss}}(h,d)$ is the acid-base interaction energy between one hemisphere and the bacterium cell (the superscript "ss" denotes single-sphere).

The most rigorous treatment of the total interaction force would be a double integral over the infinite planar surface with *all* the cylindrical pores and a spherical object at certain separation distance away from the surface. However, such an algorithm is quite computationally demanding. For this reason, the concept of an effective interaction area (A_e) between the nanoporous surface and the spherical object was introduced, which reduced the computational resources while maintaining the computation accuracy. For F_{AB} and F_{EL}, A_e can be calculated using the Langbein approximation, which yields the effective interaction area between a sphere and a flat surface. Briefly, the AB interaction of a sphere and a surface is the same as that of two planar surfaces at *the same separation distance h* if their area is:

$$A_{\mathrm{e,AB}} = 2\pi a \lambda_1 \tag{12}$$

and for the EL interaction, the effective interaction area is:

$$A_{\mathrm{e,EL}} = 2\pi a \kappa^{-1} \tag{13}$$

where κ^{-1} is the Debye length, and κ is calculated as :

$$\kappa = \sqrt{\sum_i \frac{2\rho_{\infty i} e^2 z_i^2}{\epsilon k_B T}} \tag{14}$$

where $\rho_{\infty\, i}$ is the ionic concentration of ion i in bulk solution and z_i is the valence of that ion.

Note that for the AB and EL interaction, the effective interaction area is independent of the separation distance h. From the A_{e}, the effective radius R_{e} is derived as:

$$R_{\mathrm{e}} = \sqrt{A_e/\pi} \tag{15}$$

The number of cylindrical nanopores that contribute significantly to the repulsion force exerted on one bacterium is:

$$N_w = P * (R_{\mathrm{e}}/R)^2 \tag{16}$$

where R_{e} is the radius of the effective circular interaction area, P the porosity of the surface, and R the mean radius of the cylindrical pores.

Hence, the contribution of the N_w cylindrical walls to the total acid-base interaction can be calculated as:

$$U_{\mathrm{AB}}^{\mathrm{Wall}}(h,R,P) = N_w \cdot U_{\mathrm{AB}}^{\mathrm{ms}}(h,d) = P * (R_e/R)^2 * \pi^2 \lambda_1 \Delta G_{\mathrm{AB}}\, e^{\left(\frac{h_0-h}{\lambda_1}\right)} \tag{17}$$

The total acid-base interaction energy adjusted for the presence of the pores is then:

$$U_{\mathrm{AB}}^{\mathrm{Adj}}(h,d,R,P) = PU_{\mathrm{AB}}(h,d) + (1-P)U_{\mathrm{AB}}(h,0) + U_{\mathrm{AB}}^{\mathrm{Wall}}(h,R,P) \tag{18}$$

Finally, the adjusted acid-base interaction force is:

$$F_{\mathrm{AB}}^{\mathrm{Adj}} = -\frac{\partial U_{\mathrm{AB}}^{\mathrm{Adj}}}{\partial h} \tag{19}$$

3) The electrostatic interaction energy between a bacterium and the surface is:

$$U_{\mathrm{EL}}(h,d) = \pi\, \epsilon\, a\, \left\{2\psi_b\, \psi_s\, \mathrm{Log}\left[\frac{1+e^{-\kappa(h+d)}}{1-e^{-\kappa(h+d)}}\right] + \left({\psi_b}^2 + {\psi_s}^2\right) \mathrm{Log}\left[1-e^{-2\kappa(h+d)}\right]\right\} \tag{20}$$

and

$$F_{\mathrm{EL}}(\mathrm{h,d}) = -\frac{\partial U_{\mathrm{EL}}}{\partial h} \quad (21)$$

The total electrostatic force can be treated as the sum of three contributions: *(1)* from the surface, calculated as $(1-P) * F_{\mathrm{EL}}(h,0)$; *(2)* the bottom of the cylindrical wells, expressed as $P * F_{\mathrm{EL}}(h,d)$; and *(3)* the walls of the cylindrical wells, $F_{\mathrm{EL}}^{\mathrm{Walls}}$. $F_{\mathrm{EL}}^{\mathrm{Walls}}$ was obtained by first integrating the electrostatic force element (force exerted on an area element of the bacterium bottom surface by one element of the vertical surface of the pore) over the vertical surface of *one* cylindrical pore. Subsequently the result, $F_{\mathrm{EL}}^{\mathrm{Cen}}(h,d)$, was integrated over the circular interaction area (with radius R_{i}) of the bottom surface of a bacterium cell. Finally the contribution from each pore was multiplied by the number of nanopores within the effective interaction area, N_{w}, to obtain the electrostatic interaction contributed by the walls:

$$F_{\mathrm{EL}}^{\mathrm{Walls}}(h,d,R,P) = F_{\mathrm{EL}}^{\mathrm{Cen}}(h,d)\left(\pi {R_{\mathrm{i}}}^2\right) N_{\mathrm{w}} \quad (22)$$

where $F_{\mathrm{EL}}^{\mathrm{Cen}}(h,d)$ is the electrostatic force per unit bacterium surface area exerted by a cylindrical pore of depth d, and R_{i} is the radius of the circular interaction area on the bottom surface of a bacterium cell where the electrostatic interaction is significant.

To determine $F_{\mathrm{EL}}^{\mathrm{Cen}}(h,d)$, the surface charge density of the bacterial cell and the substrate were calculated using the Grahame equation:[34]

$$\sigma(\psi_i, M_1, M_2) = \sqrt{8\epsilon k_{\mathrm{B}}T}\ \mathrm{Sinh}(C_{\mathrm{e}}\psi_i/2k_{\mathrm{B}}T) * \left[M_1 + M_2\left(2 + e^{-C_{\mathrm{e}}\psi_i/k_{\mathrm{B}}T}\right)\right]^{1/2} \quad (23)$$

where M_1 and M_2 are the bulk concentration of monovalent cations and divalent cations, which were estimated to be 0.1 M and 0 for TSB, respectively; C_{e} corresponds to the elementary charge; and ψ_i, corresponds to the surface potential of the bacteria or the substrate. Here, surface potentials were assumed to be the same as the corresponding zeta potentials.[53]

The total electrostatic interaction force adjusted for the presence of the pores becomes:

$$F_{\mathrm{EL}}^{\mathrm{Adj}} = P * F_{\mathrm{EL}}(h,d) + (1-P) * F_{\mathrm{EL}}(h,0) + F_{\mathrm{EL}}^{\mathrm{Walls}} \quad (24)$$

The key steps involved in the construction of the adjusted XDLVO model are summarized in Figure 6. The adjusted XDLVO model was constructed and computed using Mathematica 9.0 (Wolfram, Champaign, IL).

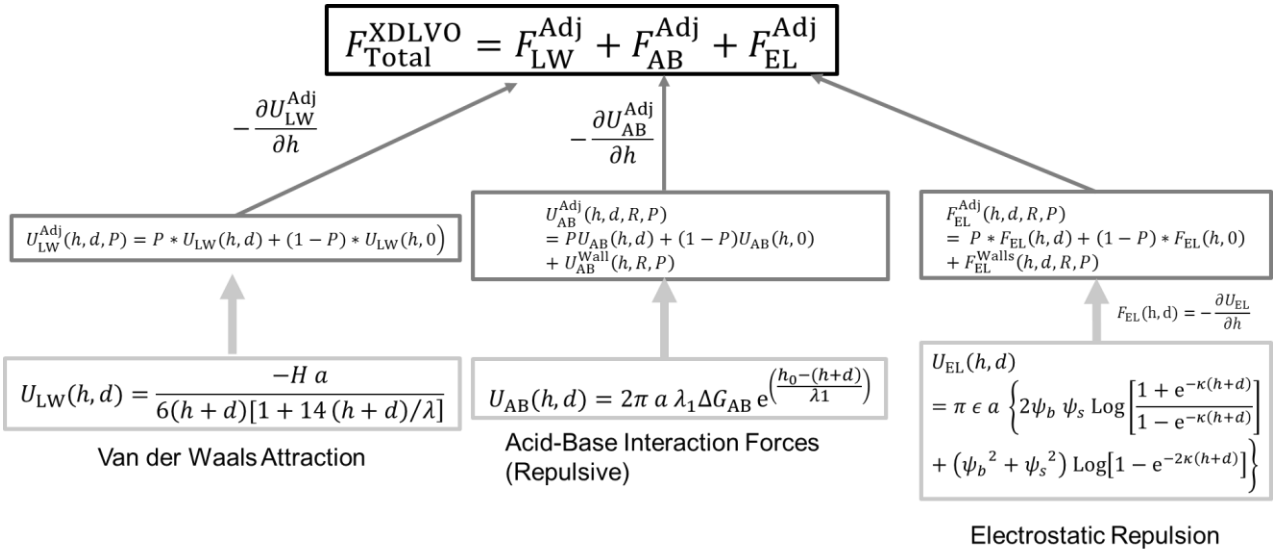

Figure 6. Key steps involved in the construction of the adjusted XDLVO model. The bottom panel contains the original formulae of the XDLVO theory; the middle panel contains the modified formulae that account for the impact of the cylindrical pores embedded in the AAO surfaces; the top panel shows the condensed formula for the adjusted XDLVO model.

1.4. Results and Discussions

1.4.1. The force-distance relationship for F_{EL}, F_{AB}, and F_{LW}

Figures Figure 7a and Figure 7b show examples of calculated interaction forces between a bacterium cell and the 15 nm anodic surface as a function of the separation distance from the surface, for *E. coli* ATCC 25922 and *L. innocua* cells, respectively. By convention, forces pointing towards the surface (attractive forces) are negative, while forces pointing away from the surface (repulsion forces) are positive [22].

In close proximity of the alumina surface, within fractions of a nanometer, the bacterium-surface interaction force for both *E. coli* and *L. innocua* is attractive for all surfaces, primarily due to the short-ranged attractive Lifertz-van der Waals forces, which are dominant at this length scale. The acid-base interaction force, which is dominant for a separation distance of several nanometers away from the surface, is strongly repulsive for *E. coli* (Figure 7a) at all separation distances from the surface, but mildly so for *L. innocua* (Figure 7b). For both microorganisms, the dominant contribution to $F_{\mathrm{Total}}^{\mathrm{XDLVO}}$ for a separation distance beyond a few nanometers comes from the repulsive electrostatic force, though the maximum of this electrostatic force is only about 1/40 of the maximum of the acid-base interaction force for *E. coli* ATCC 25922, or 1/5 for *L. innocua* on a 15 nm alumina surface. The values of the forces calculated here are in agreement with the relative magnitude of these forces reported in previous studies [21,33].

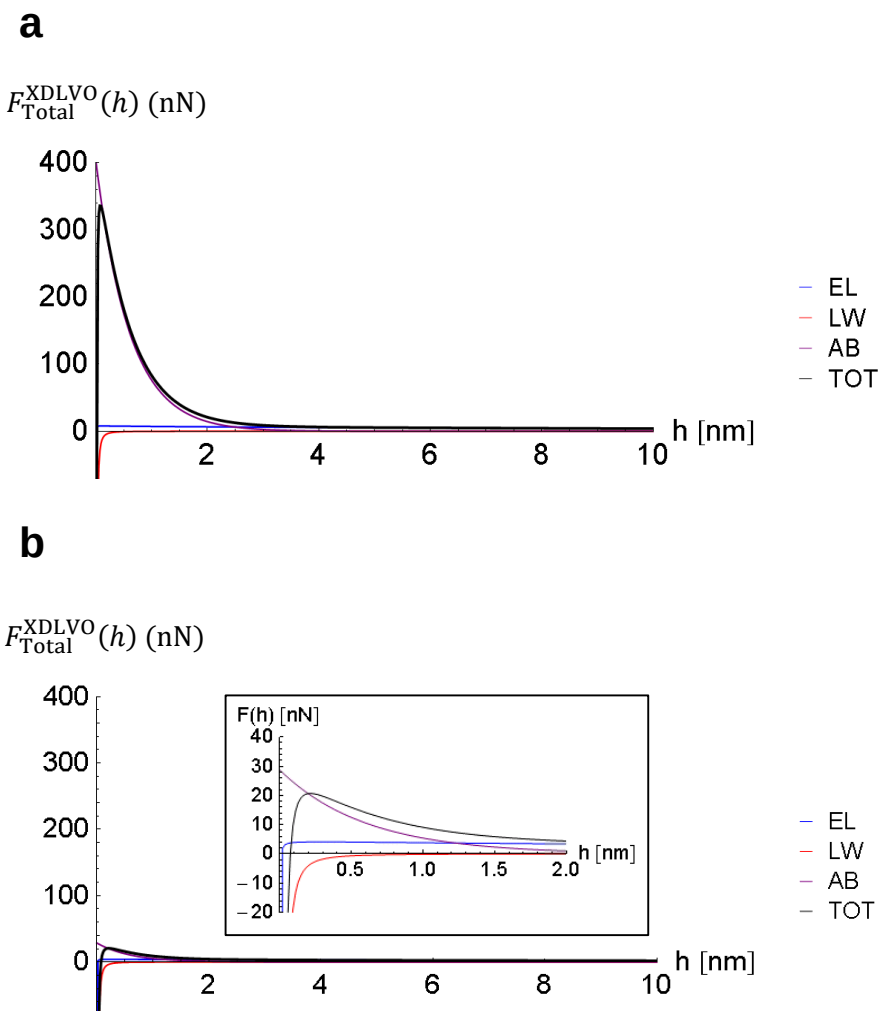

Figure 7. Interaction forces between bacterial cells and the 15 nm porous anodic alumina surface, as a function of separation distance between cells and the surface for **(a)** *E. coli* ATCC 25922 and **(b)** *L. innocua* (a magnified plot is shown in the insert). EL, electrostatic force; LW, Lifertz-van der Waals forces; AB, acid-base interaction force; TOT, total interaction force.

1.4.2. Effect of pore diameter on the total interaction force

Figure 8a and Figure 8b show the total force, $F_{\text{Total}}^{\text{XDLVO}}$, calculated for all five types of surfaces (nanosmooth control, 15 nm, 25 nm, 50 nm, and 100 nm pore AAO) as a function of the separation distance *h*. With regard to the interaction between *E. co*li ATCC 25922 or *L. innocua*

and the AAO substrates, the smaller pore surfaces (15 nm and 25 nm pore diameters) gave rise to greater maxima for $F_{\text{Total}}^{\text{XDLVO}}$ than the larger pore surfaces (50 nm and 100 nm pore diameters) (Figure 8). This maximum represents the apex of the force barrier a cell needs to overcome to further approach the surface, and will be referred to as "F_{max}" from here on.

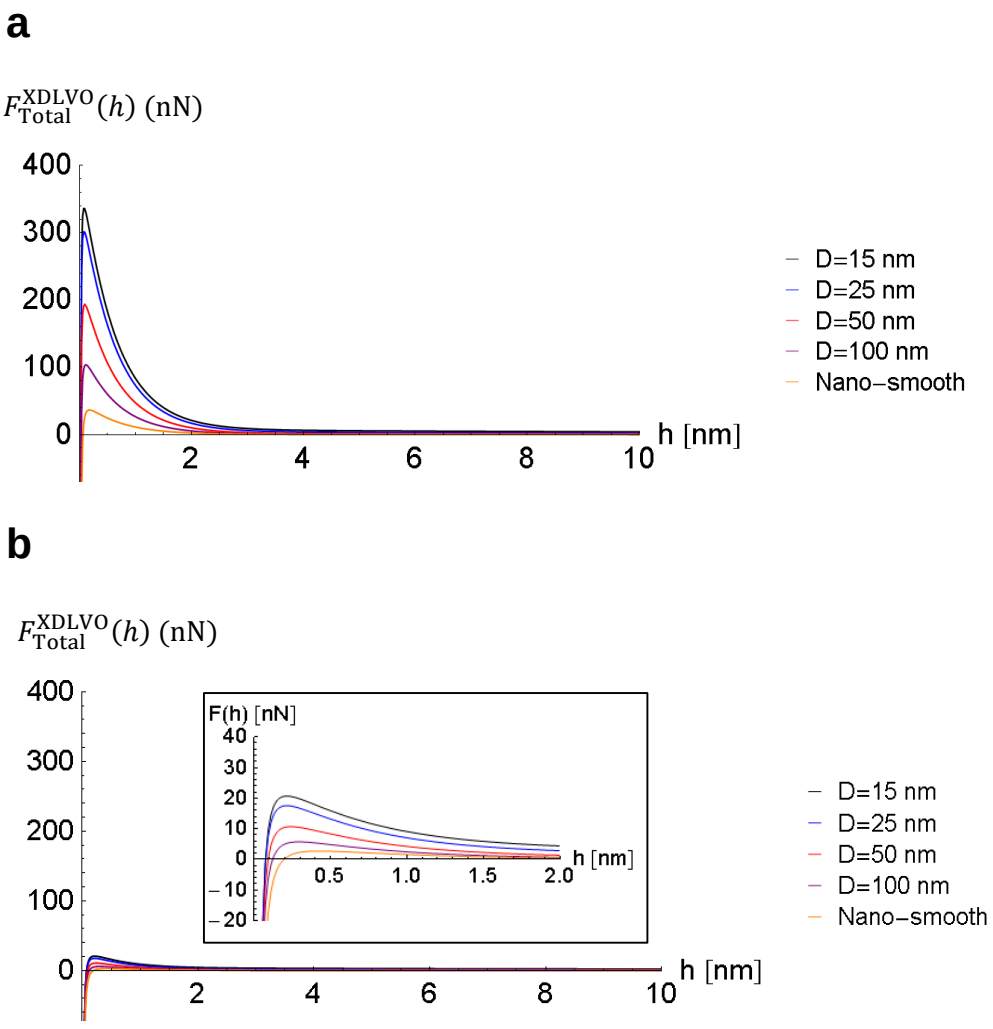

Figure 8. Total force exerted by the alumina surfaces on the bacterial cells as a function of distance from the substrate surface for **(a)** *E. coli* ATCC 25922 and **(b)** *L. innocua* (a magnified plot is shown in the insert). *D*, pore diameter.

It is worth noting that the force-distance curves in Figure 8a and Figure 8b were calculated using the real geometrical data of AAO surfaces obtained from the SEM images (Table 2). Besides pore diameter, porosity and pore depth also contributed to the observed differences in F_{max}. This is mainly because current anodization techniques do not allow the independent variation in pore size without changing the value of porosity, and thus the topographic parameters of the AAO surfaces are coupled. Therefore, we should be very cautious about oversimplifying the message, since both the surface porosity and the pore diameter, and to a lesser extent the pore depth, contributed to the greater magnitude of F_{max} of the 15 nm and 25 nm surfaces.

1.4.3. The additional repulsive force from the vertical pore walls

The next question that needs to be addressed is why do the smaller pore AAO surfaces generate greater total interaction force compared to the larger pore surfaces or the nanosmooth control? First, it should be emphasized that among the three key physicochemical forces, F_{EL} and F_{AB} are "surface forces", meaning that their magnitude is influenced by the surface area of the interacting objects, whereas F_{LW} is a "body force", meaning that its magnitude depends on the volume of the interacting objects. Therefore, it can be expected that F_{EL} and F_{AB} will increase as a result of the tremendous increase of the bacteria-surface interaction area contributed by the cylindrical walls, while F_{LW} decreases slightly due to the hollow volume represented by the pores. Consequently, due to the increase in magnitude of the repulsive force and the decrease of the attractive force, the total repulsive force, $F_{\mathrm{Total}}^{\mathrm{XDLVO}}$, increased drastically as the density of vertical pores per unit surface area increased, which was the case for the 15 nm and 25 nm pore surfaces.

To better explain this, the F_{EL} force field, chosen because of its well-defined physics, generated by a nanosmooth surface compared the porous AAO surfaces was plotted in Figure 9a.

It is apparent by comparing the top and bottom force fields that the internal vertical surface of the cylindrical pore gives rise to the peaks localized near the rim of each pore. The resulting repulsive electrostatic forces generated by a porous surface are schematically represented in Figure 9b. Since the 15 and 25 nm pore surfaces have more densely packed pore arrays, they lead to larger repulsive electrostatic forces per surface area as compared with the larger pore size surfaces.

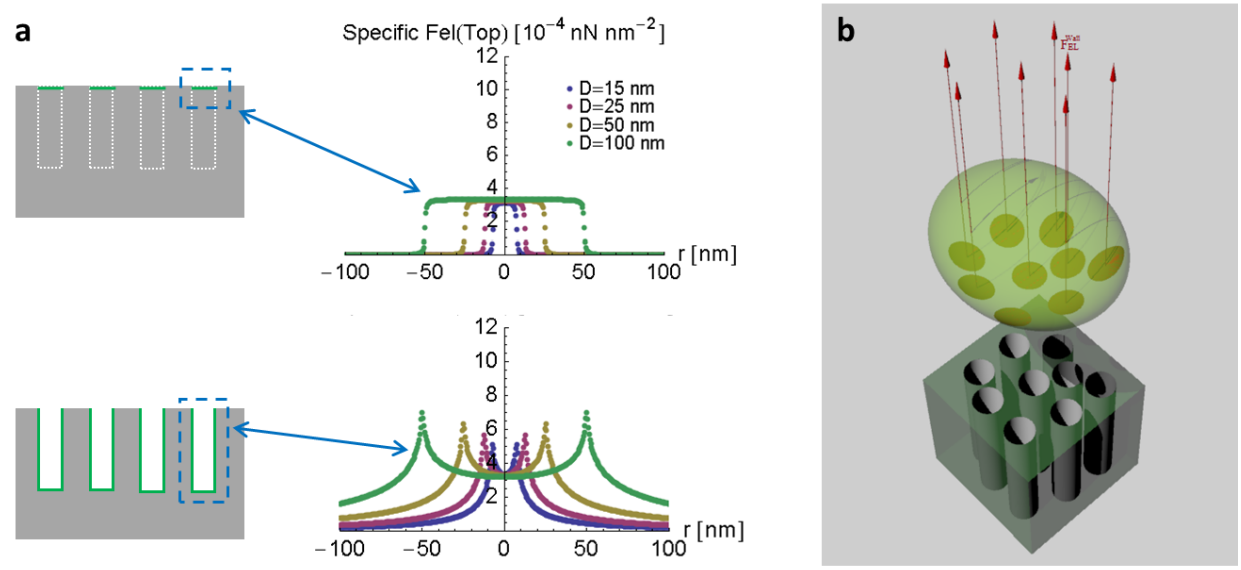

Figure 9. The mechanism underlying the higher repulsion force emanate from the small pore surfaces. **(a)** the electrostatic force field along an arbitrary diameter of a surface disc (top) and its respective cylindrical pores (bottom) for each AAO surface (i.e. 15 nm, 25 nm, 50 nm, and 100 nm) at a separation distance of 2 nm; **(b)** a schematic representation of the additional repulsive force arising from the vertical walls of the cylindrical pores.

The vertical surface of the pores also gives rise to a "high pressure" region along the rim of the pore, which may be perceived by the cell membrane's mechano-sensors as nanoscale roughness, triggering responses at genetic level[35]. Future research is needed to investigate the

transcriptomic changes that may occur before and after exposing bacterial cells to nanoporous AAO surfaces, in order to probe any biological response triggered the nanoscale topography.

1.4.4. The effect of pore depth on total interaction force

Force calculations conducted for a nanosmooth alumina surface and a bacterial cell indicate that the acid-base interactions are short-range (< 2 nm). Therefore, when incorporating $F_{\mathrm{AB}}^{\mathrm{Walls}}$ in the adjusted XDLVO model, it was considered that only the top rim of the vertical surface of the cylindrical nanopores (2 nm from the surface) effectively contributes to the acid-base interaction. For the simplicity of calculation, the internal surface of the cylindrical pores was approximated as a ring of hemispheres of 2 nm diameter distributed uniformly along the circumference of a pore. This should provide a sufficiently good approximation for large pore depth (>100 nm), as was the case in this study (Table 2).

To further investigate the impact of pore depth on the total interaction force for shallow pores, the one-ring model was extended to a k-ring model: k represents the maximum number of hemisphere layers that can be fit along the pore depth. The radius of each hemisphere was set to 0.2 nm because the radius of an oxygen atom and an aluminum atom are both close to 0.15 nm, and also because this radius allows the $F_{\mathrm{Total}}^{\mathrm{XDLVO}}$ resulting from a deep pore (> 100 nm) to be the same for the one-ring and k-ring model (Figure 10a). This modification enables the investigation of the relationship between $F_{\mathrm{Total}}^{\mathrm{XDLVO}}$ and pore depth below 2 nm, with a resolution of 0.2 nm. If we consider a single pore indenting into a flat surface (Figure 10b), the $F_{\mathrm{Total}}^{\mathrm{XDLVO}}$ first increases rapidly for the initial 5 nm under the surface, then the force increase slows down. Once the pore depth exceeds 20 nm, the additional surface area gained by the deepening of the pore virtually stops contributing to the magnitude of the total interaction force, likely due to the short effective range of the acid-base interaction.

This observation has two important implications: 1) pore depth has a significant impact on $F_{\text{Total}}^{\text{XDLVO}}$ below a pore depth of 10 nm; 2) the increase in pore depth has negligible influence on $F_{\text{Total}}^{\text{XDLVO}}$ when pore depth is large (> 100 nm). This means that a shallow pore of depth of 5 nm provides the large majority of the repulsive force contributed by a cylindrical pore. From a practical perspective however, when exposing such nanoporous surfaces to complex media (i.e. milk, juice, blood, etc.) shallow pores are more vulnerable to fouling caused by the adsorption of proteins and polysaccharides. This makes deeper pores more favorable for such applications.

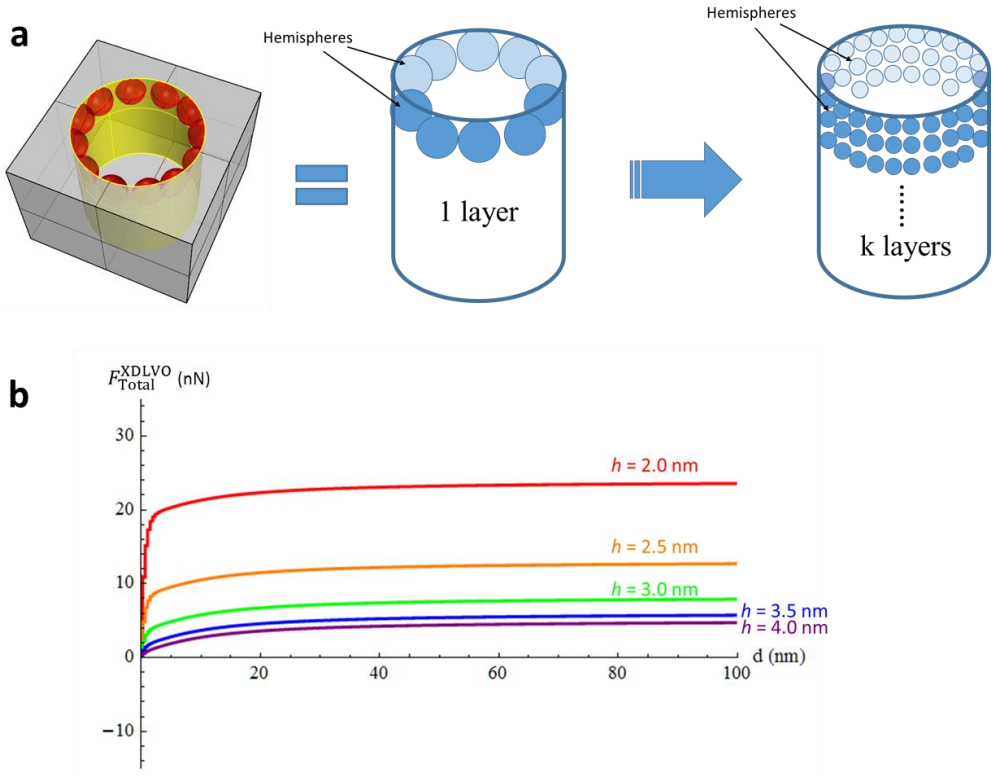

Figure 10. The effect of pore depth *d* on total interaction force F_{Total}^{XDLVO} at various separation distances *h* from the surface for an *E. coli* ATCC 25922 cell and a 15-nm pore AAO surface. **(a)** schematic representation of the extension of the one-ring model to the k-ring model; **(b)** F_{Total}^{XDLVO} as a function of pore depth at five different separation distances.

1.4.5. Verification of the adjusted XDLVO model in a model system

Verification of the predicted force-distance trajectory is critical to proving whether or not repulsive forces are responsible for the antifouling effect observed with the 15 nm and 25 nm pore anodic alumina surfaces. In this work, a verification of the model was conducted using single-cell force spectroscopy (SCFS), using Atomic Force Microscopy (AFM). While attempts were made to conduct these validations using single bacterial cells, due to challenges associated with functionalization of AFM tips with single bacterial cells, ultimately a validation was conducted using polydopamine (pD) -coated microspheres.

A single pD-coated microsphere was immobilized on an AFM cantilever using a UV-curable adhesive, and the interaction forces between the microsphere and the various nanostructured AAO surfaces were measured in TSB. This colloidal model system was selected for two reasons: first, the physicochemical properties – i.e. zeta potential, surface energy components, and geometry – of the pD-coated microsphere could be experimentally determined, and then plugged into the adjusted XDLVO model to generate theoretical force-distance (FD) curves. The model was then validated by directly comparing these force curves with the force curves recorded using the colloidal AFM probe. Secondly, pD-coated microspheres can potentially mediate the immobilization of a single live cell on a tipless triangular AFM cantilever, which would allow direct measurement of cell-surface or cell-cell interaction forces.[36,37] The force-distance curves generated with the pD-coated microsphere will provide a baseline value for future single bacterial cell FD curves.

1.4.5.1. Preparation of microsphere-modified AFM probes

The protocol published by Beaussart et. al.[36,37] was followed. Briefly, using an Asylum MFP-3D^{TM} AFM (Asylum Research, Goleta, CA), triangular shaped tipless cantilevers (NP-O10, Bruker, Santa Barbara, CA) were slowly brought into contact with a very thin layer of ultraviolet (UV)-curable glue (NOA 63, Norland Edmund Optics, NJ, USA) spread on a glass slide, and slowly touched down on silica microsphere of 6.1 μm average diameter (Bangs Laboratories, IN, USA) (Figure 11a). The appropriate amount of glue (2 μm in droplet diameter) is critical for the successful pickup of the sphere, since too much glue will result in submersion of the sphere in the glue. The microsphere-modified probe was immediately cured for 10 min at 365 nm using a hand-held 4-watt UV lamp (Norland Edmund Optics, NJ, USA). To accurately quantify the interaction between the microsphere and a solid substratum, it is critical for the microsphere to be fixated at the center point of the farthest edge of a triangular cantilever. For this reason, the quality of a microsphere-modified probe was examined under SEM (Figure 11b and 38c) and fluorescence microscopy (Figure 11d). Figure 11d was acquired using an invert 63 × oil lens of a Zeiss 710 laser scanning microscope with an excitation wavelength of 488 nm. These images indicated that the microsphere was securely fixated at the desired location. To coat the colloidal probe with a homogeneous layer of polydopamine, the microsphere-modified cantilever was immersed for 1 h in a 10 mM Tris Buffer solution (pH 8.5) containing 4 mg/mL dopamine hydrochloride (99%, Sigma). The incubation process was carried out in isolation from light to ensure optimal polymerization of dopamine.[37,38]

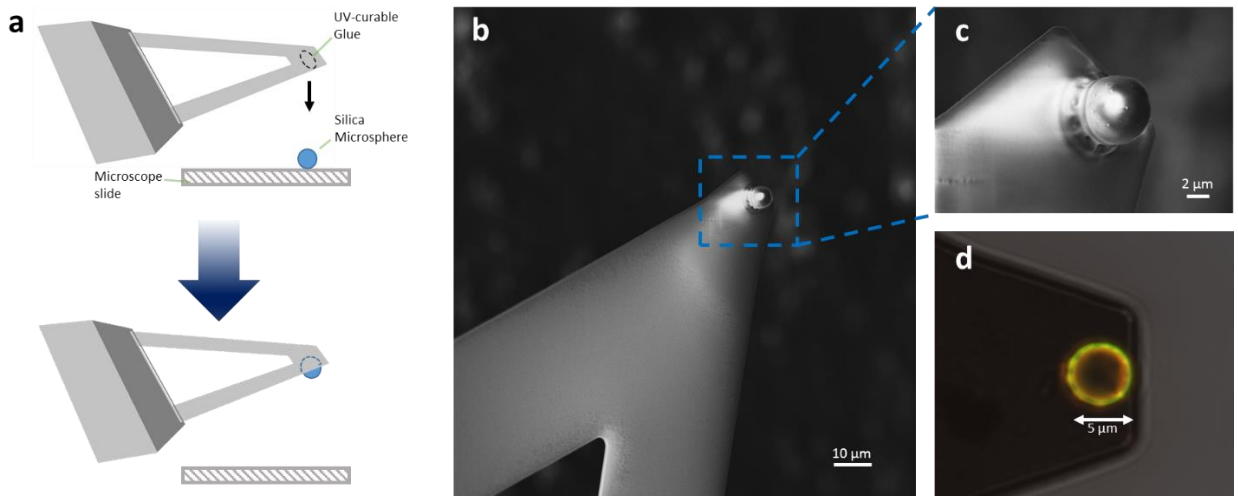

Figure 11. Modification of a tipless triangular AFM cantilever with a single silica microsphere. **(a)** Schematic representation of the adhesion process using an AFM; **(b)** SEM image of the microsphere modified AFM tip; **(c)** magnified image of the tip in (b); **(d)** fluorescence microscopy image of the tip. The green fluorescence came from the UV-curable glue used to mediate the adhesion.

1.4.5.2. Determination of the physicochemical parameters of the polydopamine coating

Before coating with polydopamine, glass cover slides (24 × 55 mm, Deckglaser, Guntersville, AL, USA) were carefully rinsed with copious acetone, isopropanol, and DI water, followed by 30 min of sonication in DI water, then air-dried under a biosafety hood for 30 min. These glass slides were then submerged in dopamine solution (2 mg mL^{-1}, in 10 mM Tris-HCl buffer, pH 8.5) and incubated for 24 h at 21 °C. Since the polymerization rate of dopamine solution is very light sensitive, the sample was carefully shielded from light using aluminum foil for the entire incubation process. Such incubation conditions were shown to result in a uniform

polydopamine coating with thickness around 40 nm on the glass cover slides.[38] The pD-coated glass slides were air-dried under a biosafety hood for at least 30 min before contact angle or surface zeta potential measurement.[39]

Contact angles (CA) on pD-coated glass slides were determined by the sessile drop method using a Rame-Hart 500 goniometer (Rame-Hart Inc., Succasunna, NJ) [11,22]. Three probe liquids were used: water (Mili-Q; Merck Millipore Ltd., Billerica, MA), glycerol (Mallinckrodt, St. Louis, MO), and diiodomethane (Sigma-Aldrich Corp., St. Louis, MO). The advancing angles of each liquid on polydopamine-coated glasses were recorded and then used for calculating the surface energy components of polydopamine. CA measurements of each probe liquid were repeated five times on independently coated glasses.

The surface zeta potential of polydopamine was measured using a Malvern Zetasizer nano-ZS (Malvern Instruments Ltd., Malvern, Worcestershire, UK) with a surface zeta potential cell (Malvern Instruments Ltd., Malvern, Worcestershire, UK). The glass slides were cut into rectangular pieces with the dimensions 5 mm × 3 mm × 1.5 mm (length × width × thickness), which were cleaned and coated with polydopamine (pD) using the protocol described above. After 30 min of drying in air under a biosafety hood, the pD glass slides were mounted onto the plastic stage of the surface zeta potential cell via a double-sided Scotch™ tape. The cell was submerged in a BPB buffer (pH 7, ionic strength = 0.1 M, 21 °C) that simulates the TSB medium used for the AFM experiment. The surface zeta potentials of the pD glasses were calculated by the Zetasizer Nanosize software based off of the apparent zeta potentials of the tracer particles at five positions: 125 μm, 250 μm, 375 μm, 500 μm, and 675 μm apart from the solid-liquid interface. The values of contact angles and zeta potentials of the polydopamine coating are summarized in Table 3.

Table 3. Contact angles (CA) and zeta potential values of the polydopamine coating

Substrate	Contact angles (°) in various liquids, N = 5			Zeta potential (mV), N = 3
	WCA (water)	DCA (diiodomethane)	GCA (glycerol)	
pD-coated glass	21.1±2.0	34.4±1.5	10.8±2.2	-32.9±1.1

1.4.5.3. Force-distance curves for a pD-coated microsphere interacting with various alumina substrates

I. Experimental methods: AFM setup and probe calibration

Nanosmooth alumina (controls) and AAO coupons (1 cm × 1 cm) were rinsed with acetone, isopropanol, and sonicated in DI water for 1 h to remove any surface contaminants. After that, each surface was dried with nitrogen gas and mounted onto a microscope glass slide using double-sided tape. A liquid droplet method was used to measure the interaction force between a colloidal probe and the surfaces in TSB (Figure 12). First, a volume of 50 µL of sterile TSB medium was deposited onto the AAO surface, followed by 10 min of equilibration. To calibrate the spring constant of the pD-coated colloidal probe, the entire AFM tip was slowly lowered into the equilibrated TSB medium. By using the thermal tune function, the spring constant of the pD-coated microsphere probe in TSB at 21 °C was determined to be 93.3±12.8 pN/nm (average ± standard deviation) (N = 3). Immediately after calibration, the forward (approach) F-D curves were determined by lowering the AFM probe towards the substrate surface at a constant speed of 1.00

μm s^{-1}, starting from a separation distance of 1000 nm until a 'trigger' force of 10 nN was reached, upon which the probe was retracted to the starting position. A low approaching speed of 1.00 μm s^{-1} was chosen to limit the hydrodynamic drag on the cantilever below 10 pN. This value was measured in water [40]; the viscosity of TSB at 21 °C is very close to that of water. This threshold value of the hydrodynamic drag is two orders of magnitude smaller than the measured surface forces. This process was repeated on five representative spots on each of the surfaces (nano-smooth, 15 nm, 25 nm, 50 nm, and 100 nm pore AAO), in a randomized order. A different colloidal tip was used for each set of surfaces, and three sets of surfaces were used for this study.

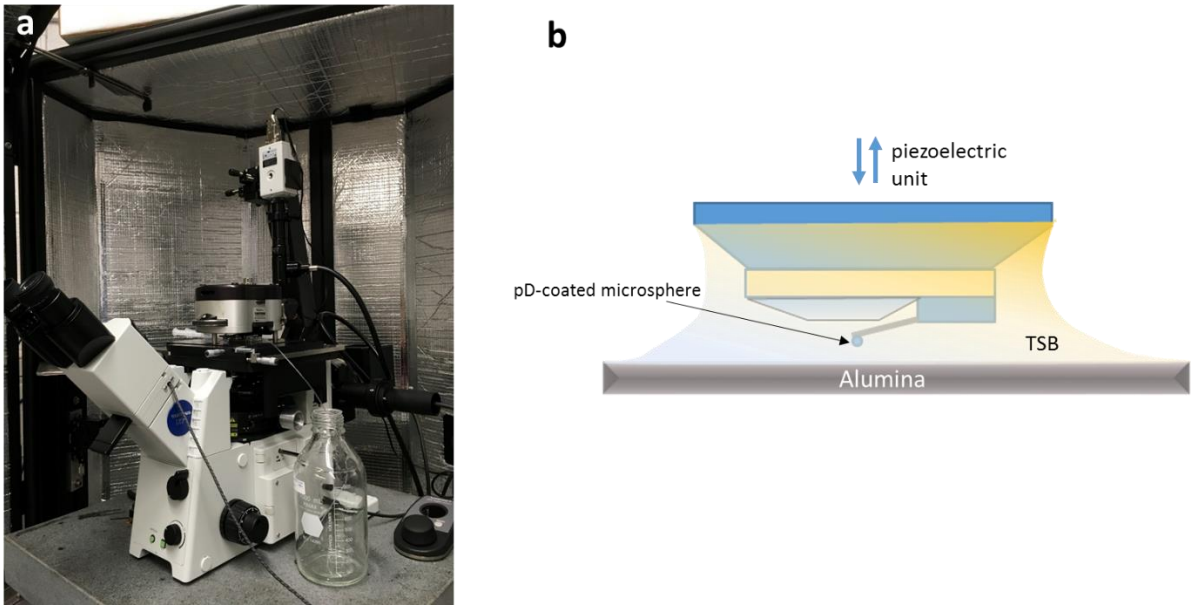

Figure 12. The experimental setup for AFM force-distance measurement using the liquid droplet method. **(a)** Photo of the AFM-Fluorescent microscope system; **(b)** schematic representation of a microsphere-modified probe interacting with an alumina substratum submerged in TSB.

II. Results and discussions

The F-D curves generated by AFM and the theoretical F-D curves predicted by the adjusted XDLVO model are shown in Figure 13a and Figure 13b, respectively. As predicted by the adjusted XDLVO model, the actual total microsphere-surface interaction force was the greatest for the 15 nm-pore AAO (black circles in Figure 13a), followed by the 25 nm-pore (blue circles), and then the 50 nm-pore (red circles) and the 100 nm-pore (purple circles). For all AAO surfaces, the experimental and the theoretical curves both show an increase in the magnitude of the total interaction force as the separation distance between the microsphere and the substrates decreases. However, the predicted peaks and the subsequent steep decrease in force due to the attractive acid-base interaction in close proximity to the surfaces were not found in the measured AFM curves.

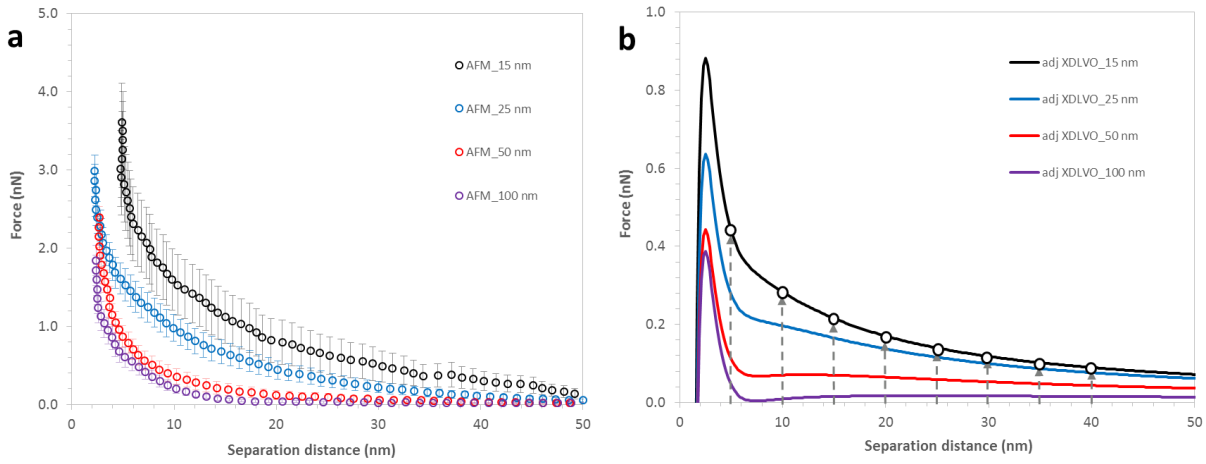

Figure 13. Force-distance curves measured experimentally with AFM and those predicted theoretically by the adjusted XDLVO model. The theoretical curves are calculated based on the interaction between a polydopamine-coated silica microsphere (R = 3.0 µm) and AAO substrates with different pore sizes.

One possibility for this disagreement is that the microspheres might have some surface roughness at the nanoscale and might also have large-scale polarity (imperfect spherical shape), which can be noticed in Figure 11c. Any surface irregularities of the microsphere could result in local physical contact between its surface topography and the substrate at an apparent separation distance greater than zero, leading to errors in the force measurements near the surfaces (a few nm separation distance).

To analyze the similarity between the two sets of curves, representative points from each AAO surface type were extracted from the actual and the predicted curves. These data points were sampled over a separation distance ranging from 5 nm to 40 nm, with a step size of 5 nm, which resulted in eight points per type of surface, as shown by the dashed arrows in Figure 13b. A correlation plot between these values was generated (Figure 14). A statistically significant linear correlation ($p < 0.001$) was obtained between the experimental and predicted force values, indicating that overall the model reflects well the actual force curves ($R^2 = 0.879$).

Despite the good correlation between predicted and measured values, as well as in the relative magnitude of the microsphere-surface interaction forces for the different surfaces, the absolute magnitude of the measured force was approximately five times larger than the predicted values ($y = 5.2\ x$). It is possible that some assumptions adopted by the model, such as the calculation of effective area by the Langbein approximation, may have led to this discrepancy in magnitude. The possibility that mechanism(s) other than those considered by the XDLVO theory could have contributed to the total interaction force, particularly the repulsive force, should not be excluded. For instance, Chapter Four of this dissertation will provide experimental evidence for a long-range phenomenon occurring at hydrophilic interfaces, known as “exclusion zone”, whose existence cannot be explained by the XDLVO theory alone.

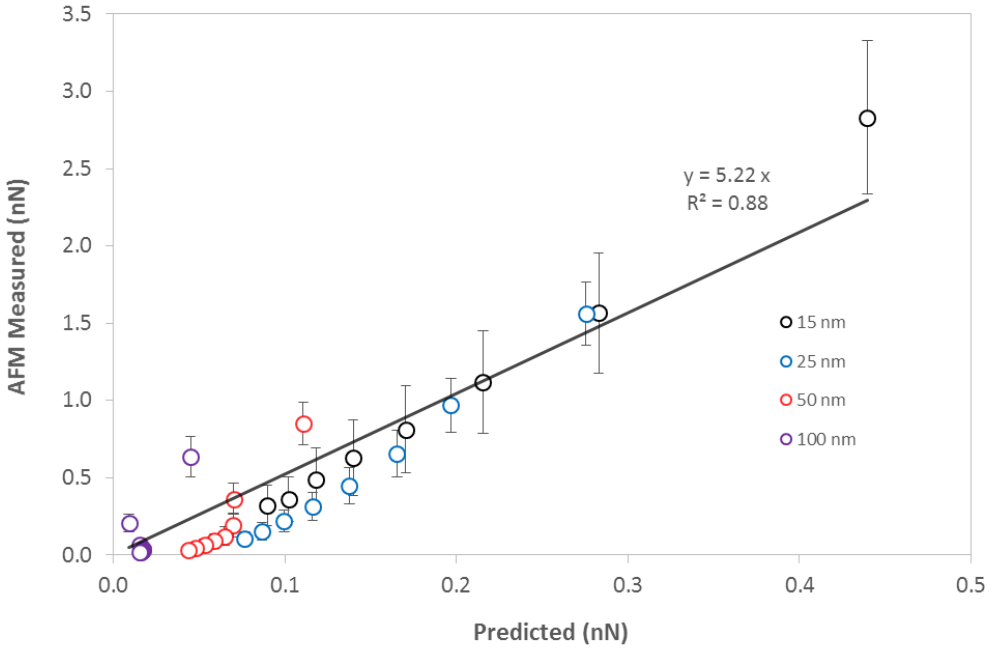

Figure 14. Correlation plot between the total interaction force measured by AFM and the force predicted by the adjusted XDLVO model for a pD-coated silica microsphere interacting with alumina surfaces, in TSB. For each surface force values at eight separation distances were sampled. The error bars present standard error of means (*N* = 15 for each data point).

It is also possible that the actual measurements may introduce some errors, and this has to be further explored in the near future.

1.5. Conclusions

In this work, the extended XDLVO model was adjusted by integrating the force components over the topography to account for the impact of surface nanoscale structures on bacterial attachment. The adjusted extended XDLVO model predicts that AAO surfaces with 15 nm and 25 nm pores exert greater repulsive force and higher maximum force barrier (F_{max}) than the larger pore AAO surfaces and the nanosmooth alumina.

The vertical internal surfaces of the densely-packed cylindrical pores of the smaller pore AAO surfaces were identified as the source of the additional repulsive force leads to the greater F_{max}. Pore depth was found to significantly affect total interaction force when the pore is shallow (< 5 nm), yet hardly influence the force when the pore is deep (> 100 nm).

AFM measurements verified the model prediction that the total repulsive force exerted on a micrometric scale object is greater for the 15 nm and 25 nm pore AAO surfaces than the 50 nm and 100 nm ones. Some differences in the magnitude of measured vs. predicted forces point to either some systematic model errors or the existence of additional repulsive mechanisms that may not have been accounted for by the model, which will be in part discussed later in this thesis.

REFERENCES

(1) Katsikogianni, M.; Missirlis, Y. F. Concise Review of Mechanisms of Bacterial Adhesion to Biomaterials and of Techniques Used in Estimating Bacteria-Material Interactions. *Eur. Cell. Mater.* **2004**, *8*, 37–57.

(2) Mafu, A. A.; Roy, D.; Goulet, J.; Savoie, L. Characterization of Physicochemical Forces Involved in Adhesion of Listeria Monocytogenes to Surfaces. *Appl. Environ. Microbiol.* **1991**, *57* (7), 1969–1973.

(3) Carpentier, B.; Cerf, O. Biofilms and Their Consequences, with Particular Reference to Hygiene in the Food Industry. *J. Appl. Microbiol.* **1993**, *75* (6), 499–511.

(4) Zhao, Q.; Liu, Y.; Wang, C.; Wang, S.; Müller-Steinhagen, H. Effect of Surface Free Energy on the Adhesion of Biofouling and Crystalline Fouling. *Chem. Eng. Sci.* **2005**, *60* (17), 4858–4865.

(5) Baier, R. E. Substrata Influences on the Adhesion of Micro-Organisms and Their Resultant New Surface Properties. In *Adsorption of micro-organisms to surfaces*; Bitton, G., Marshall, K. C., Eds.; John Wiley & Sons Inc: New York, 1980; pp 59–104.

(6) Zhao, Q.; Liu, Y.; Wang, C. Development and Evaluation of Electroless Ag-PTFE Composite Coatings with Anti-Microbial and Anti-Corrosion Properties. *Appl. Phys. Lett.* **2005**, *252* (5), 1620–1627.

(7) Zhao, Q.; Wang, C.; Liu, Y.; Wang, S. Bacterial Adhesion on the Metal-Polymer Composite Coatings. *Int. J. Adhes. Adhes.* **2007**, *27* (2), 85–91.

(8) Pereni, C. I.; Zhao, Q.; Liu, Y.; Abel, E. Surface Free Energy Effect on Bacterial Retention. *Colloids Surf. B Biointerfaces* **2006**, *48* (2), 143–147.

(9) Zhao, Q.; Wang, S.; Müller-Steinhagen, H. Tailored Surface Free Energy of Membrane Diffusers to Minimize Microbial Adhesion. *Appl. Surf. Sci.* **2004**, *230* (1–4), 371–378.

(10) Liu, W.; Fryer, P. J.; Zhang, Z.; Zhao, Q.; Liu, Y. Identification of Cohesive and Adhesive Effects in the Cleaning of Food Fouling Deposits. *Innov. Food Sci. Emerg. Tech.* **2006**, *7* (4), 263–269.

(11) Busscher, H. J.; Weerkamp, a. H.; van der Mei, H. C.; van pelt, A. W.; de jong, H. P.; Arends, J. Bacterial Cell Surfaces and Its Relevance for Measurement of the Surface Free Energy of Bacterial Cell Surfaces and Its Relevance for Adhesion. *Appl. Environ. Microbiol.* **1984**, *48* (5), 980–983.

(12) Bos, R.; van der Mei, H. C.; Busscher, H. J. Physico-Chemistry of Initial Microbial Adhesive Interactions--Its Mechanisms and Methods for Study. *FEMS Microbiol. Rev.* **1999**, *23* (2), 179–230.

(13) Baier, R. E. Surface Behaviour of Biomaterials: The Theta Surface for Biocompatibility. *J. Mater. Sci. Mater. Med.* **2006**, *17* (11), 1057–1062.

(14) Marshall, K. C.; Stout, R.; Mitchell, R. Mechanism of the Initial Events in the Sorption of Marine Bacteria to Surfaces. *J. Gen. Microbiol.* **1971**, *68* (3), 337–348.

(15) Hori, K.; Matsumoto, S. Bacterial Adhesion: From Mechanism to Control. *Biochem. Eng. J.* **2010**, *48* (3), 424–434.

(16) van Loosdrecht, M. C. M.; Lyklema, J.; Norde, W.; Zehnder, A. J. B. Bacterial Adhesion : A

Physicochemical Approach. *Microb. Ecol.* **1989**, *17* (1), 1–15.

(17) Bunt, C. R.; Jones, D. S.; Tucker, I. G. The Effects of pH, Ionic Strength and Polyvalent Ions on the Cell Surface Hydrophobicity of Escherichia Coli Evaluated by the BATH and HIC Methods. *Int. J. Pharm.* **1995**, *113* (2), 257–261.

(18) Vigeant, M. a; Ford, R. M. Interactions between Motile Escherichia Coli and Glass in Media with Various Ionic Strengths, as Observed with a Three-Dimensional-Tracking Microscope. *Appl. Environ. Microbiol.* **1997**, *63* (9), 3474–3479.

(19) Otto, K.; Elwing, H.; Hermansson, M. Effect of Ionic Strength on Initial Interactions of Escherichia Coli with Surfaces, Studied on-Line by a Novel Quartz Crystal Microbalance Technique. *J. Bacteriol.* **1999**, *181* (17), 5210–5218.

(20) Bolster, C. H.; Mills, A. L.; Hornberger, G. M.; Herman, J. S. Effect of Surface Coatings, Grain Size, and Ionic Strength on the Maximum Attainable Coverage of Bacteria on Sand Surfaces. *J. Contam. Hydrol.* **2001**, *50* (3–4), 287–305.

(21) van Oss, C. J. Acid—base Interfacial Interactions in Aqueous Media. *Colloids Surfaces A Physicochem. Eng. Asp.* **1993**, *78*, 1–49.

(22) Li, B.; Logan, B. E. Bacterial Adhesion to Glass and Metal-Oxide Surfaces. *Colloids Surf. B. Biointerfaces* **2004**, *36* (2), 81–90.

(23) Feng, G.; Cheng, Y.; Wang, S.; Hsu, L. C.; Feliz, Y.; Borca-Tasciuc, D. a.; Worobo, R. W.; Moraru, C. I. Alumina Surfaces with Nanoscale Topography Reduce Attachment and Biofilm Formation by Escherichia Coli and Listeria Spp. *Biofouling* **2014**, *30* (November), 1253–1268.

(24) Bos, R.; Van Der Mei, H. C.; Gold, J.; Busscher, H. J. Retention of Bacteria on a Substratum Surface with Micro-Patterned Hydrophobicity. *FEMS Microbiol. Lett.* **2000**, *189*, 311–315.

(25) Sharma, P. K.; Hanumantha Rao, K. Adhesion of Paenibacillus Polymyxa on Chalcopyrite and Pyrite: Surface Thermodynamics and Extended DLVO Theory. *Colloids Surfaces B Biointerfaces* **2003**, *29* (1), 21–38.

(26) Bhattacharjee, S.; Sharma, A.; Bhattacharya, P. K. Estimation and Influence of Long Range Solute. Membrane Interactions in Ultrafiltration. *Ind. Eng. Chem. Res.* **1996**, *35*, 3108–3121.

(27) Hsu, L.; Fang, J.; Borca-Tasciuc, D.; Worobo, R.; Moraru, C. I. The Effect of Micro- and Nanoscale Topography on the Adhesion of Bacterial Cells to Solid Surfaces. *Appl. Environ. Microbiol.* **2013**.

(28) Ran, C.; Ding, G.; Liu, W.; Deng, Y.; Hou, W. Wetting on Nanoporous Alumina Surface: Transition between Wenzel and Cassie States Controlled by Surface Structure. *Langmuir Acs J. Surfaces Colloids* **2008**, *24* (18), 9952–9955.

(29) Gregory, J. Approximate Expression for Retarded van Dar Waals Interaction. *J. Colloid Interface Sci.* **1981**, *83* (1), 138–145.

(30) Silva, S.; Teixeira, P.; Oliveira, R.; Azeredo, J. Adhesion to and Viability of Listeria Monocytogenes on Food Contact Surfaces. *J. Food Prot.* **2008**, *71* (7), 1379–1385.

(31) Meagher, L.; Klauber, C.; Pashley, R. M. The Influence of Surface Forces on the Fouling of Polypropylene Microfiltration Membranes. *Colloids Surf A Physicochem. Eng. Asp.* **1996**, *106* (1), 63–81.

(32) Edy, R.; Huang, X.; Guo, Y.; Zhang, J.; Shi, J. Influence of Argon Plasma on the Deposition of Al2O3 Film onto the PET Surfaces by Atomic Layer Deposition. *Nanoscale Res. Lett.* **2013**, *8* (1), 79.

(33) Brant, J. a.; Childress, A. E. Membrane–Colloid Interactions: Comparison of Extended DLVO Predictions with AFM Force Measurements. *Environ. Eng. Sci.* **2002**, *19* (6), 413–427.

(34) Grahame, D. C. Diffuse Double Layer Theory for Electrolytes of Unsymmetrical Valence Types. *J. Chem. Phys.* **1953**, *21* (6), 1054–1060.

(35) Rizzello, L.; Galeone, A.; Vecchio, G.; Brunetti, V.; Sabella, S.; Pompa, P. P. Molecular Response of Escherichia Coli Adhering onto Nanoscale Topography. *Nanoscale Res. Lett.* **2012**, *7* (1), 575.

(36) Beaussart, A.; El-Kirat-Chatel, S.; Sullan, R. M. A.; Alsteens, D.; Herman, P.; Derclaye, S.; Dufrêne, Y. F. Quantifying the Forces Guiding Microbial Cell Adhesion Using Single-Cell Force Spectroscopy. *Nat. Protoc.* **2014**, *9* (5), 1049–1055.

(37) Beaussart, A.; El-Kirat-Chatel, S.; Herman, P.; Alsteens, D.; Mahillon, J.; Hols, P.; Dufrêne, Y. F. Single-Cell Force Spectroscopy of Probiotic Bacteria. *Biophys. J.* **2013**, *104* (9), 1886–1892.

(38) Terrill, H. Optimization of Polydopamine Coatings. *Honor. Res. Proj.* **2015**.

(39) Busscher, H. J.; van Pelt, A. W. J.; de Boer, P.; de Jong, H. P.; Arends, J. The Effect of Surface Roughening of Polymers on Measured Contact Angles of Liquids. *Colloids and Surfaces* **1984**, *9* (4), 319–331.

(40) Janovjak, H.; Struckmeier, J.; Müller, D. J. Hydrodynamic Effects in Fast AFM Single-Molecule Force Measurements. *Eur. Biophys. J.* **2005**, *34* (1), 91–96.

CHAPTER TWO

ALUMINA SURFACES WITH NANOSCALE TOPOGRAPHY REDUCE ATTACHMENT AND BIOFILM FORMATION BY *ESCHERICHIA COLI* AND *LISTERIA* SPP [1]

2.1. Abstract

Prevention of bacterial biofilm formation is of critical importance to areas like medicine, dentistry, food processing, or water treatment. This work reports on a simple, robust and scientifically sound method to develop surfaces able to reduce microbial attachment and biofilm development. Anodic surfaces with cylindrical nanopores of 15 to 100 nm diameter were manufactured and incubated with *Escherichia coli* ATCC 25922 and *Listeria innocua*. Surfaces with 15 nm and 25 nm pore diameter significantly repressed attachment and biofilm formation. Surface-bacteria interaction forces calculated using the extended Derjaguin Landau Verwey-Overbeek (XDLVO) theory indicate that reduction in attachment and biofilm formation is due to a synergy between electrostatic repulsion and surface effective free energy. An attachment study using *E. coli* K12 strains unable to express appendages also suggests that the small-pore surfaces may inhibit flagella-dependent attachment. These results can have immediate, far-reaching implications and commercial applications, with great benefits for human health and life.

2.2. Introduction

Biofilm formation by pathogenic bacteria has harmful, sometimes fatal, consequences and can pose severe contamination problems in medicine, dentistry, food processing, and water

[1] The main content of this chapter is published in the *Biofouling* paper: Alumina surfaces with nanoscale topography reduce attachment and biofilm formation by *Escherichia coli* and *Listeria* spp. Biofouling 2014, 30 (November), 1253–1268. Authors: Guoping Feng, Yifan Cheng, Shu-Yi Wang, Lillian C. Hsu, Yazmin Feliz, Diana A. Borca-Tasciuc, Randy W. Worobo, and Carmen I. Moraru.

treatment. For instance, colonization by bacteria on medical devices and biofilm-related infections account for 80% of all human bacterial infections [1]. Nosocomial infections in hospital settings, commonly associated with contaminated medical devices, represent one of the leading causes of death in the US [2]. Biofilms formed by pathogenic organisms in food processing plants are a major culprit in foodborne diseases, which claim thousands of lives and amount to financial losses of about $78 billion/year in the US alone [3]. Therefore, significant efforts are made to develop solutions for preventing biofilm formation, in order to effectively combat microbial contamination in environments that directly affect human health and life.

Bacterial adhesion to surfaces is the first step in the development of biofilms. Microbial biofilms are cohesively structured, three-dimensional matrices that are notoriously difficult to remove by physical and chemical means. Besides microbial cell surface properties and environmental factors, the physicochemical properties of the surface, including topography and roughness, free surface energy and surface charge are critical to attachment of bacteria cells and subsequent biofilm formation [4–8].

The effects of surface topography and roughness at the microscale on attachment have been extensively studied, sometimes with contradictory findings. Several studies conducted with microorganisms of interest for medical and food processing environments, including *Streptococcus thermophilus*, *Streptococcus waiu*, *Listeria monocytogenes*, and *Flavobacterium odoratum*, reported inconclusive correlations between surface roughness and bacterial adhesion [5,9,10]. In contrast, other studies indicated a significant impact of surface roughness on attachment [11,12]. Apart from roughness, a defined surface topography has also been shown to influence bacterial attachment. In general, surfaces with channels, pits or pillars of dimensions comparable to bacteria cells appear to impact bacterial attachment, while surface details at a scale larger than

the cell size do not affect it significantly [13–16]. Some of these effects are in part due to the interaction between the adhesins on bacteria surface, including flagella, fimbriae, or curli, with elements of surface topography [17–19]. A recent study by Friedlander et al. reported that flagella expressed by *E. coli* can reach into surface crevices and act as structural elements in attachment and biofilm formation [20]. Recent studies from our group indicate significant differences in expression of cellular appendages as a response to surface topography in the micro- and nanoscale range [21].

Adhesion of bacteria cells to nanostructured surfaces is recognized to be significantly different from that on bulk or microstructured materials [22,23]. Typically, explanations of this behavior allude to the fact that nanostructured materials possess greatly altered surface chemical and physical properties. For instance, nanostructuring can induce significant changes in effective surface charge and effective surface free energy, which affect attachment and biofilm formation [24].

The ability to induce changes of surface properties using nanostructuring represents a great opportunity to design materials able to effectively repel microorganisms. However, in most cases nanostructuring requires expensive nanofabrication methods, which render the approach prohibitively expensive for many practical applications. Nanostructured surfaces can also be extremely delicate and incompatible with the stringent cleaning procedures used in many industrial or medical applications. Compared to other nanofabrication methods, anodization is a widely available surface treatment that produces an oxide which, under well-controlled conditions, exhibits a nanoporous structure. The anodic oxide is chemically inert to many cleaning agents and has excellent wearing properties. Anodization is used on an industrial scale and can be applied to large surface areas, as well as three-dimensional parts. Aluminum anodization in particular is a

widely used process, with countless industrial applications [25]. By controlling the applied anodizing voltage and bath composition, Al anodization produces cylindrical, parallel pores oriented perpendicular to the surface, of defined pore diameter and surface porosity [26,27]. Using two-step anodization, cylindrical pores organized in a hexagonal array can be obtained [26].

This study explores the effect of nanoscale topography created by anodization on the attachment and biofilm formation by gram-positive and gram-negative bacteria, the mechanisms responsible for the impact of nanoscale surfaces on attachment, and demonstrates a simple yet robust solution to prevent bacteria attachment by controlling surface properties.

2.3. Materials and Methods

2.3.1. Surface Fabrication

Nanoporous aluminum oxide surfaces with pore diameters of 15 nm, 25 nm, 50 nm and 100 nm were prepared by two-step anodization of high purity aluminum substrate (99.99%, Alfa Aesar). The Al substrate was first subjected to mechanical and electrochemical polishing, to obtain a smooth surface. An annealing process was performed between the two polishing steps to release internal stresses [27]. Prior to the first anodization step, the Al substrate was immersed in an etchant to remove the thin alumina layer formed during electrochemical polishing. After that, the first anodization step was carried out. The voltage and anodizing mixture depended on the desired pore size. For anodization, a setup similar to the one used for electrochemical polishing was employed, with the difference that the reaction was carried out at room temperature. The pores formed during the first anodization are usually disorganized at the surface, but self-organize as they grow deep into the substrate. Hence, this first porous alumina layer was etched away and a second anodization step was performed [26]. In the second step, pore growth was initiated from dents left over by the nanopores in the first layer which lead to regular surface features [26,27]. Nano-smooth aluminum

oxide with dimensions of 10×10×0.5 mm (Alfa Aesar, Ward Hill, MA) was used as the control surface.

2.3.2. Bacterial cultures and media

The bacterial strains used in this study were the gram-negative *E. coli* ATCC 25922, which has been used before as a surrogate for *E. coli* O157:H7 in attachment studies [28], and the gram positive bacteria *L. innocua* FSL C2-008; *L. innocua* strains have been used in previous attachment studies as surrogates for pathogenic *L. monocytogenes* [29]. In addition, four strains of *E. coli* K12 wild-type (WT), flagellum-deficient (*ΔflgA*), fimbriae-deficient (*ΔfimH*) and curli-deficient (*ΔcsgA*) mutants were used to study the impact of surface adhesins on attachment. The *E. coli* K12 strains were obtained from National BioResource Project at National Institute of Genetics in Japan. All cultures were maintained at -80°C in TSB (Difco, Becton Dickinson and Company, Sparks, MD) with 20% (v/v) glycerol. *E. coli* K12 mutant strains were maintained in same medium with 30 µg/ml of kanamycin. The strains were reactivated on tryptic soy agar (TSA, Difco). Bacteria cultures were grown in capped culture tubes with TSB at 37°C, with shaking at a speed of 225 rpm.

2.3.3. Characterization of surfaces by scanning electron microscopy (SEM)

The surface topographic features and bacteria attachment were visualized using a Zeiss LEO 1550 field emission scanning electron microscope (Carl Zeiss Microscopy, LLC, Germany). For analyzing the bare surfaces, small coupons of each substrate were cleaned using two cycles of 30-min sonication in Milli-Q water, then rinsing in absolute ethanol. For visualizing surfaces with attached bacteria cells, alumina surfaces were retrieved at 48 h of incubation and rinsed in sterile water to remove unattached cells. Bacteria on surfaces were initially fixed using 2.5% (w/v) glutaraldehyde in 0.05 M sodium cacodylate buffer at 4°C for 2 h. Samples were rinsed in

cacodylate buffer three times, for 5 min each time, then subjected to a secondary fixation step using 1% (w/v) osmium tetroxide in cacodylate buffer, for 1 h. The fixated samples were rinsed in cacodylate buffer three times as described above, then dehydrated using gradient ethanol solutions of 25% (v/v), 50%, 70%, 95%, 100% and 100% for 10 min each. Samples in 100% ethanol were critical point-dried with carbon dioxide. Dried surfaces were mounted on SEM stubs with carbon tape and coated with evaporated carbon. A voltage of 1-5 kV and working distance of 2-3 mm were used, depending on the sample. Images were acquired using the accompanying software SmartSEM (Carl Zeiss Microscopy).

2.3.4. Bacterial attachment and biofilm formation

Bacteria strains were subcultured from freshly streaked colonies on TSA in 4 ml of TSB for 24 h. A volume of 10 µl culture was transferred to 3 ml of fresh TSB and incubated for 12-15 h. The alumina surfaces were cleaned using two cycles of 30-min sonication in Milli-Q water, and sterilized by rinsing in absolute ethanol. The clean and sterilized alumina surfaces were vertically placed in TSB containing the *E. coli* or *L. innocua* culture, without shaking, and incubated at 37°C for up to 96 h.

2.3.5. Visualization and quantification of biofilm matrices using confocal laser scanning microscopy (CLSM)

Surfaces prepared as above were sampled at 30 min, 48 h and 96 h of incubation. The nanosmooth (control), 15 nm, 25 nm, 50 nm and 100 nm pore size surfaces were vertically placed in stationary-phase *E. coli* ATCC 25922 and *L. innocua* cultures at 37°C for 30 min. TSB with a 1:100 (v/v) inoculation from 16-h old cultures were used for incubation with surfaces for the 48-h and 96-h time points. The alumina surfaces with attached cells were removed gently from the bacteria culture and rinsed using a swirling motion in sterile saline solution (0.15 M NaCl) 3 times,

to remove unattached cells. The surfaces were then submerged in 2 ml of the saline solution containing 4 µl/ml of the Live/Dead BacLight 1:1 mixture of the Syto 9 and red-fluorescent propidium iodide (Molecular Probes Inc., Eugene, OR). The nucleic acid stains were allowed for integration for at least 15 min prior to CLSM. Surfaces were then removed from the Live/Dead BacLight solution and rinsed in sterile saline solution another 3 times before being used for CLSM. Surfaces were then placed with the surface of interest facing down in saline solution in glass-bottom culture dishes (MatTek Corporation, Ashland, MA) during CLSM analysis so that the integrity of the biofilm matrix and its architecture was maintained.

A Zeiss 710 confocal laser scanning microscope with upright objectives was used for image acquisition. An excitation wavelength of 488 nm with two channels was used for both fluorophores. Images were acquired with a Plan-Apochromat 25× oil immersion objective lens at a scanning speed of 9 and frame pixels of 512×512 (pixel size = 0.66 µm), corresponding to a surface area of 338.4×338.4 μm^2. The laser power and pinhole were set to 2.8% and 1.0 airy unit, respectively. Laser gain for both channels was continuously adjusted to eliminate and minimize oversaturation or undersaturation of the fluorophores. The attached cells and biofilms attached to the surface were scanned in 3D mode (z-stack scanning) from the surface to the highest point of the biofilm matrix. The step size for z-stack scanning was 1.0 µm. Five randomly selected, but evenly spaced spots per surface were chosen for scanning. Three-dimensional structures of biofilm matrices were constructed and visualized using the image analysis software Volocity (version 5.2.1, PerkinElmer, Waltham, MA).

Quantification of the biofilm volume and thickness was performed using the software package COMSTAT, developed by Heydorn et al.[30] Threshold values (2 to 3) were assigned to individual image stacks. The biomass volume ($\mu m^3/\mu m^2$) and the thickness of the layer of attached

bacteria were quantified. Since the biomasses formed by live and dead cells were similar in trend, the quantification of biofilm matrices was based only on live cells.

2.3.6. Assessing the role of bacterial appendages in initial attachment to nanoporous alumina surfaces

E. coli K12 isogenic mutant strains of wild type (WT) and genes of *flgA*, *fimH* and *csgA* were selected from the Keio mutant library consisting of single-gene knockouts [31]. The selection of the genes was based on previous findings that knockout of these related genes resulted in significant reduction in biofilm formation, suggesting their possible role in attachment and early biofilm formation [19]. These genes encode essential structural proteins in flagella, fimbriae and curli. Specifically, *flgA*, *fimH* and *csgA* encode major assembly protein for flagellar basal-body periplasmic P ring, Type 1 fimbriae adhesin unit, and curlin major unit, respectively. Bacterial attachment was quantified by plating the cells detached from surfaces to tryptic soy agar (TSA) and calculated as CFU/cm^2 (i.e. CFU/surface) according to a method described previously [9] with minor modifications. All strains were loop-inoculated and cultured in TSB at 37 °C for 16 h with aeration (225 rpm). The strains were subcultured in a fresh medium by a 1:100 (vol./vol.) inoculation until cell density reached OD_{600nm} = 1.1 (10^9 cells/mL), which took approximately 3.5 h. The 15 nm and 100 nm pore size surfaces were vertically placed in 3 ml of TSB containing each strain at 37 °C for 30 min. The surfaces were retrieved after 30 min and rinsed three times by gently swirling in 15 ml of 0.15 M NaCl solution to remove loosely attached cells. The rinsed surfaces were sonicated in 2 ml of 0.15 M NaCl for 10 min to detach the attached cells. The recovered cell suspension was serially diluted and plated on TSA, which was then incubated overnight at 37 °C. The experiments were repeated independently for at least three times.

2.3.7. Measurement of contact angles

Contact angles on bacterial cell lawns and alumina substrates were determined by the sessile drop method using a Rame-Hart 500 goniometer (Rame-Hart Inc., Succasunna, NJ) [32,33]. To measure the contact angles of bacterial cells, *E. coli* ATCC 25922, *L. innocua* and *E. coli* K12 strains were cultured as described above. They were harvested at stationary phase by centrifugation at 4 °C and 5,000 rpm for 10 min using a Hettich 32R benchtop centrifuge (Hettich Instruments, Beverly, MA). The cells were washed by resuspending in 30 mL of Butterfield's phosphate buffer (BPB; *pH* 7.0 ± 0.2, ionic strength = 0.01 M) and subsequently subjected to centrifugation under the same conditions. The harvested cells were re-suspended in BPB prior to filtration. *E. coli* ATCC 25922 and *L. innocua* cell lawns were then prepared by filtering 30 mL of the cell suspension under vacuum through a polyethersulfone (PES) membrane (0.45 μm pore size, 47 mm diameter, Millipore Express Plus; Merck Millipore Ltd., Billerica, MA) using a magnetic filtering funnel (300 mL, 47 mm diameter; Pall Corp., Port Washington, NY). This was followed by drying under vacuum in the same funnel for at least 1 h. Each PES membrane, containing approximately 70 layers of bacteria, was mounted onto a microscope slide with double-sided tape and allowed to dry under a biosafety hood for another 10 min. Contact angles were measured with deionized ultrapure water (Mili-Q; Merck Millipore Ltd., Billerica, MA), glycerol (Mallinckrodt, St. Louis, MO), and diiodomethane (Sigma-Aldrich Corp., St. Louis, MO), using the dynamic mode of the goniometer. Stable advancing angles were averaged to determine the contact angle. For each strain, three independently grown cultures were used. At least two lawns of each strain were prepared and measured with all three liquids. Contact angles for the *E. coli* K12 cell lawns (i.e. WT, Δ*flgA,* Δ*csgA*, and Δ*fimH*) were determined following the same protocol,

with the exception that the lawns were not subjected to the 10-min drying step in order to avoid cracking.

Contact angle measurements on nano-smooth alumina substrates were performed in triplicate, using the same set of probe liquids as for the bacterial cells.

2.3.8. Surface charge measurements

The zeta potential of bacterial cells was measured using a Malvern Zetasizer nano-ZS (Malvern Instruments Ltd., Malvern, Worcestershire, UK) with disposable folded capillary cells (Malvern Instruments Ltd., Malvern, Worcestershire, UK). Briefly, a 1:10 dilution of cells (prepared as described above) was prepared using MiliQ water and the cell suspension was gently vortexed to ensure homogeneity. A 1-mL sample was then aliquoted into the cuvette and inserted into the measurement chamber. Zeta potential values were measured at 20 °C three times using 20 cycles per analysis on each of the biological triplicates.

2.3.9. Statistical analysis and mathematical modeling

Experiments were repeated independently at least three times, with each experiment having two biological samples per surface group and technical duplicates for each sample. Five random areas per surface were sampled for CLSM and data obtained from these technical repeats was averaged to obtain a mean value for each surface. Student's *t* test was used to compare two populations. To compare means of more than two sample populations, one-way ANOVA analysis was performed, which was followed by post-ANOVA Tukey's test. All statistical tests were performed using JMP 8.0 (SAS Institute, Cary, NJ). The adjusted XDLVO model was constructed and computed using Mathematica 9.0 (Wolfram, Champaign, IL).

2.4. Results and Discussions

2.4.1. Bacterial attachment and biofilm formation

A two-step anodization process as described above was used to produce alumina surfaces with average pore diameters of 15 nm, 25 nm, 50 nm and 100 nm, respectively, and micrometer-size pore length. As control, nanosmooth alumina was used. Surfaces were submerged in nutritive broth inoculated with the challenge organisms, and bacterial attachment and biofilm formation on these surfaces were observed at 30 min, 48 h, and 96 h. Three-dimensional images of biofilm matrices obtained by confocal laser scanning microscopy (CLSM) are shown in Figure 15 and Figure 16 for *E. coli* ATCC 25922 and *L. innocua* FSL C2-008, respectively.

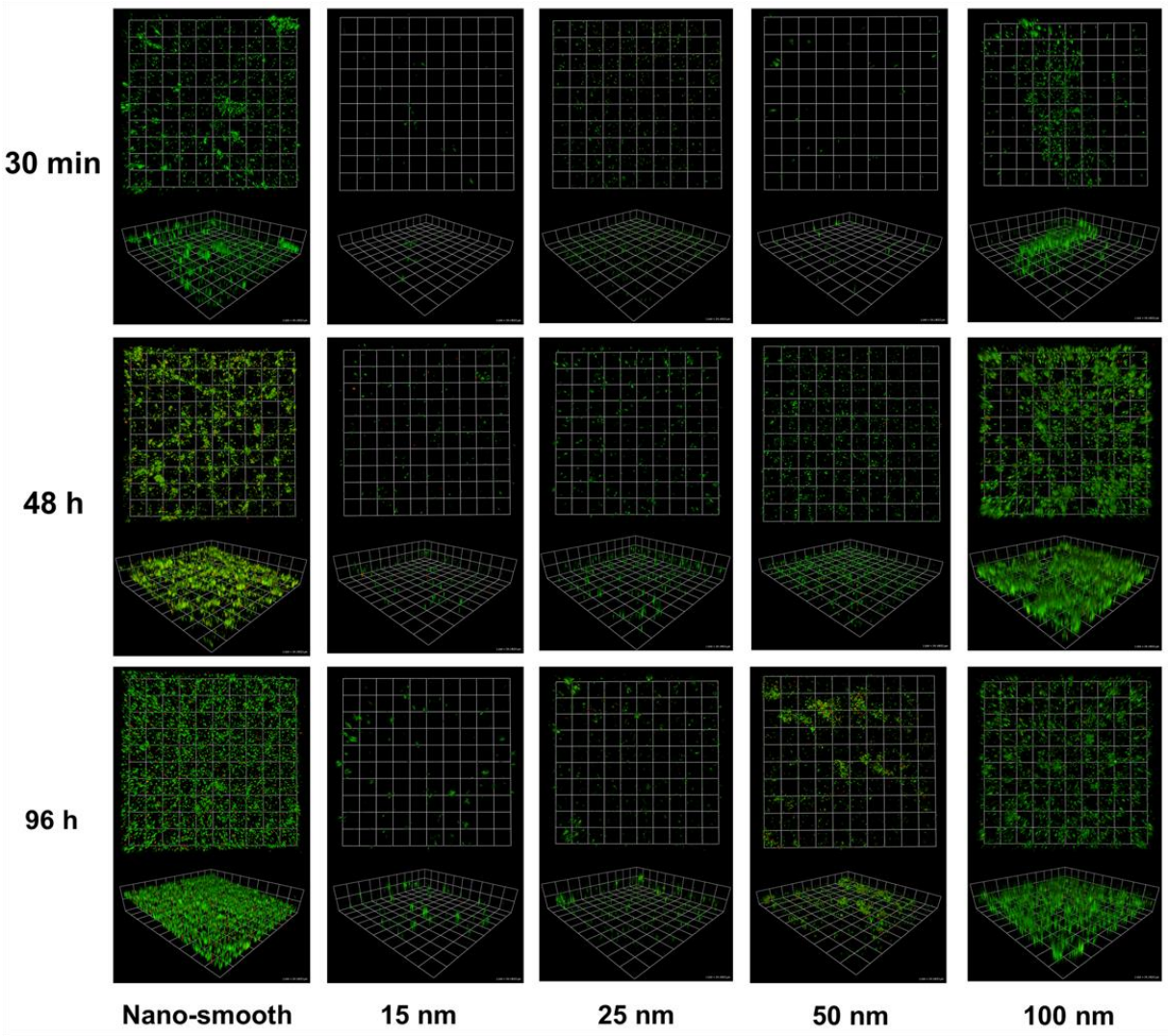

Figure 15. Constructed confocal laser scanning microscopy (CLSM) 3D images of attachment and biofilm formation by *E. coli* ATCC 25922 at 30 min, 48 h, and 96 h on nano-smooth alumina (control) and anodized surfaces of 15 nm, 25 nm, 50 nm and 100 nm pore diameter. The top and bottom images in each panel represent top and side views of the same scanned area. The presented images have biomass accumulation close to the average of their surface type. Scale units (small grid) are 34 µm in length.

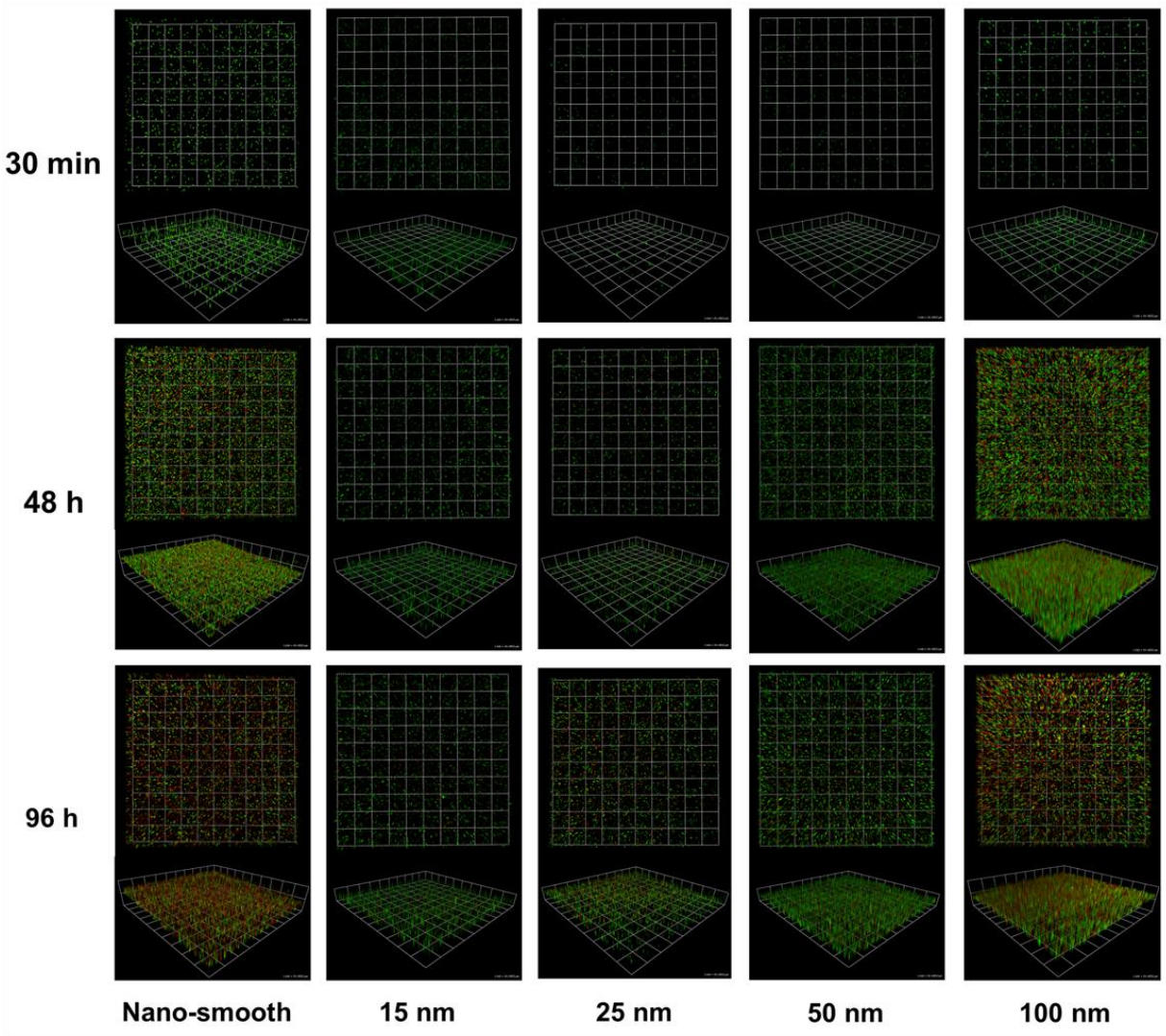

Figure 16. Constructed CLSM 3D images of attachment and biofilm formation by *L. innocua* FSL C2-008 at 30 min, 48 h, and 96 h on nano-smooth alumina (control) and anodized surfaces of 15 nm, 25 nm, 50 nm and 100 nm pore diameter. The top and bottom images in each panel represent top and side views of the same scanned area. The presented images have biomass accumulation close to the average of their surface type. Scale units (small grid) are 34 µm in length.

As seen in Figure 15 & Figure 16, *E. coli* had an astonishingly low presence on the 15 nm and 25 nm pore surfaces, for the entire period probed while *L. innocua* displayed the same trend despite less pronounced differences at early stages (30 min and 48 h) of biofilm formation. For *E. coli*, a limited presence was also observed on the 50 nm surfaces after 30 min and 48 h; biofilm formation appeared to some extent at 96 h. In contrast, on the nanosmooth control and 100 nm pore surfaces *E. coli* adhered at a significantly ($P<0.05$) higher level than on the small pore surfaces, and a well-developed biomass was observed. The biofilm matrices formed on these two surfaces were highly structured laterally and vertically at 48 h and 96 h, as evidenced by both the volume of biofilm formed on the surfaces and the thickness of the biofilm layer. The 100 nm surface retained a significantly ($P<0.05$) higher amount of *E. coli* cells and a more cohesively structured biofilm than the nanosmooth surface.

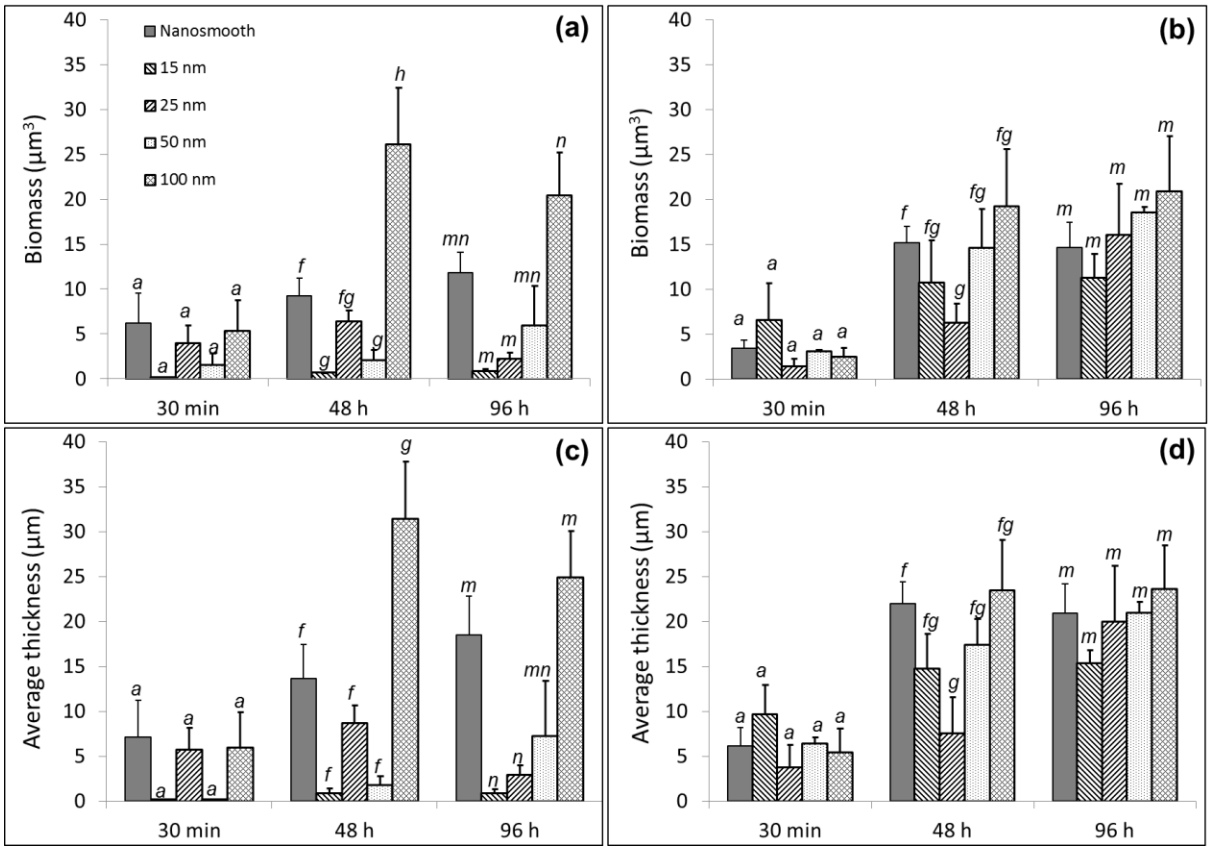

Figure 17. Average values (*N* = 3) of biomass and thickness of biofilm matrices formed by *E. coli* ATCC 25922 (a and c) and *L. innocua* FSL C2-008 (b and d) at 30 min, 48 h and 96 h on nanosmooth alumina, and anodized surfaces of 15 nm, 25 nm, 50 nm and 100 nm pore diameter. For any given time point, values not connected by the same letter are statistically different from each other ($P<0.05$). Error bars represent standard error of means.

A quantitative assessment of the three-dimensional biofilm made using the software COMSTAT [30] is shown in Figure 17. For all three time points, the volume of biomass formed by *E. coli* on the 15 nm surface was the least of all surfaces. At 96 h, the average biomass on this surface was 0.8 $\mu m^3/\mu m^2$. In contrast, the biomass volume for the 100 nm surface was about 15 times larger (11.8 $\mu m^3/\mu m^2$), while for the nanosmooth control it was about 25 times larger (20.4 $\mu m^3/\mu m^2$). At 48 h the 15 nm and 25 nm surfaces retained significantly less biomass than the

nanosmooth control, while the biomass on the 100 nm surface was significantly higher than all others ($P < 0.05$); the same trend was observed at 96 h. The biomass accumulation on the control was comparable to that on the 100 nm surface, for both time points.

Vertical growth often comes with a complex 3D architecture of the biofilm matrix, which renders the biofilm more resistant to environmental stresses. In this study, average thickness was used as an indicator of vertical growth of the biofilms. The average thickness of the biofilms formed by *E. coli* on all surfaces followed a trend similar as the biomass, with the 15 nm and 25 nm surfaces showing the smallest thickness, and the nanosmooth and 100 nm surfaces the largest thickness (Figure 17c). At 96 h the average thickness on the 15 nm surface was 0.9 μm, which suggests the presence, in average, of a monolayer of cells. At the same time point, the thickness for the 100 nm pore size and nanosmooth control was 24.9 μm and 18.5 μm, respectively, which indicates the presence of 20 to 30 layers of cells in the biofilm architecture.

L. innocua showed similar trends to *E. coli* in biofilm formation, although the antifouling effects on the 15 and 25 nm pore surfaces were less pronounced for this microorganism in terms of magnitude of difference (Figure 16 and Figure 17b&d). At 96 h, the volume and the thickness of biomass formed by *L. innocua* on the 15 nm pore surface were 11.2 μm^3 and 15.3 μm, respectively. On average, the 15 nm surface showed about 40% less biomass than the control and the larger pore diameter surfaces although statistically significant difference from the control was observed only with the 25 nm surfaces (Figure 17b) at 48 h. The significant reduction in biomass and thickness by *L. innocua* may be partly due to the initial interaction that could be different from *E. coli* because it is known that *Listeria* spp. could not express mobility appendages such as flagella at 37°C that would otherwise help *L. innocua* cells penetrate the energy barrier and subsequently approach the surface.

Overall, the quantitation of biofilm structures and the CLSM observations demonstrates that anodized alumina surfaces with 15 nm and 25 nm pores reduced attachment and biofilm formation by *E. coli* and *L. innocua*, while the 100 nm surface promoted biofilm formation at a level similar or higher than the nanosmooth control.

2.4.2. Effect of anodized surfaces on bacterial cells

In the previous section, it was shown that the physicochemical interactions between the substrate and the bacterial cells play a major role in attachment. Nonetheless, this attachment behavior is likely also due to biological changes experienced by the cells in response to surface topography. Surface topography has been shown to induce morphological, transcriptomic and proteomic shifts in bacteria [17,18,21,34–36]. A comprehensive understanding of how nanoscale topography affects the expression of biomolecular entities that play a role in bacterial interaction with nanostructured surfaces is not available at the moment. An aspect somewhat well understood is the surface effect on cellular adhesins. Rizzello et al. reported that *E. coli* cells grown on nanostructured surfaces lost the expression of fimbriae [37], which are considered critical virulence factors required for initial attachment [38]. *E. coli* is known for its ability to develop cellular appendages, such as pili and flagella, which have a strong role in the later stages of microbial attachment and biofilm formation [24]. Bacteria may use these small diameter cellular appendages to penetrate the energy barrier produced by the repulsive physicochemical forces, facilitating cell attachment to an otherwise repelling surface.

The SEM examination of the surfaces with attached cells shows a striking difference between the type and number of appendages expressed by *E. coli* on the various surfaces (Figure 21). This is consistent with earlier observations from our group, which showed that expression of cellular appendages by *E. coli* and *P. fluorescens* was strongly affected by surface topography [21].

The appendages observed in this study resemble closely those observed by other researchers [17] for curli-producing *E. coli* strains. The structure of these appendages was distinct from that of extracellular polymeric substances (EPS) produced by *E. coli* (Figure 18). The *E. coli* cells imaged on the nanosmooth control (Figure 21a) and the larger pore anodic surfaces (Figure 21 d-e) appear clustered in a complex architecture and feature a large number of long, intertwined appendages. In contrast, the *E. coli* cells on the 15 nm and 25 nm pore surfaces appear as isolated cells and feature only very few, relatively short appendages (Figure 21 b-c). From the SEM images, the diameter of the appendages expressed by the *E. coli* cells was estimated between 30-60 nm. For surfaces with pore diameters above this size, the appendages can easily penetrate inside the pores, which will help anchor the cells and the biofilms onto the surface. This was clearly observed for the 50 nm and 100 nm surfaces, for which appendages were seen to penetrate inside the pores (Figure 21 d-e). *E. coli* may be able to sense the surface topography, use appendages to explore surface features and attach to surfaces.

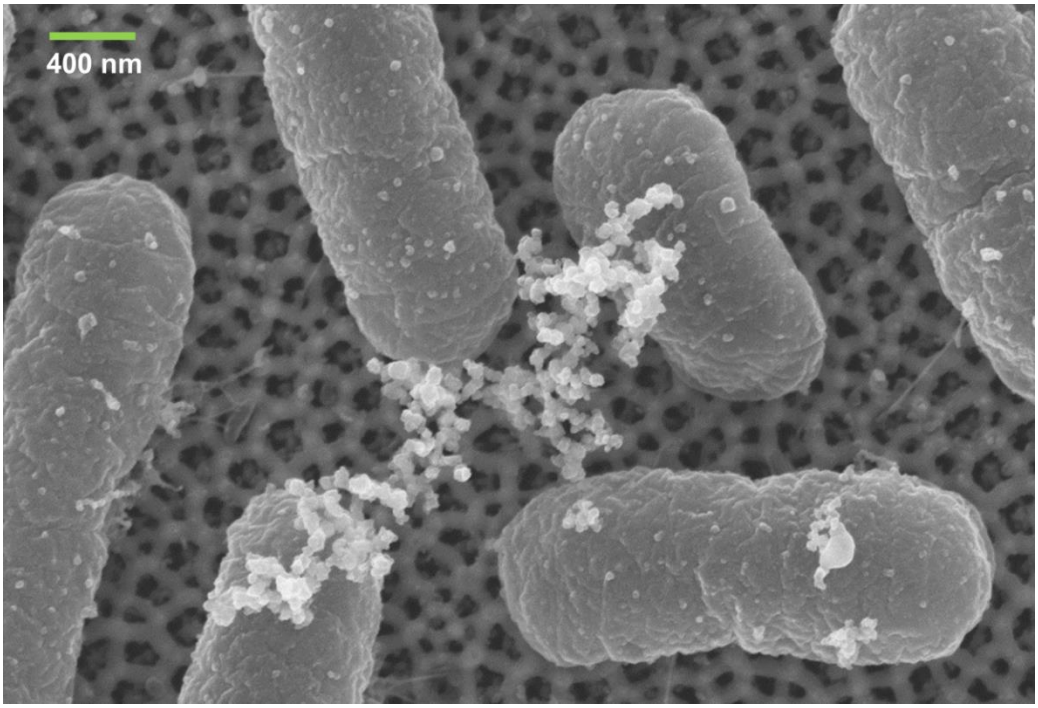

Figure 18. Sample SEM image of *E. coli* K12 wild-type cells producing extracellular polymeric substances (EPS) on alumina surfaces with 100 nm pores.

2.4.3. A physicochemical explanation of bacterial attachment and biofilm formation

The construction of the adjusted XDLVO model was described in detail in section 1.3. of Chapter One. The maximum total repulsive force ($F_{\max}$) was found to correlate very well with the number of cells attached to the surface / forming the biofilm, as shown in Figure 19. The number of cells was estimated by dividing the biomass volume for each strain–surface pair by the volume of an individual cell of that particular strain. The average cell volumes were calculated based on the cell size data [21], and were 0.50 μm^3/cell for *E. coli* ATCC 25922 and 0.13 μm^3/cell for *L. innocua.*

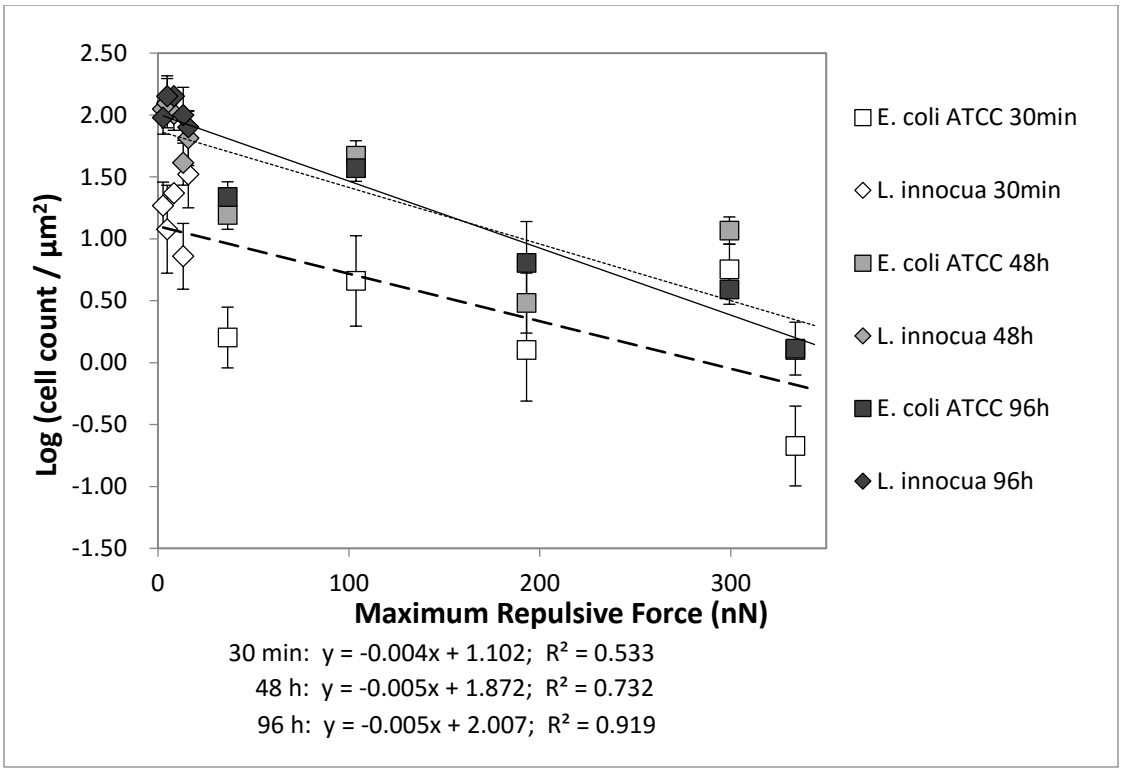

Figure 19. Correlation between cell count per unit area and the peak value of the total interaction force (repulsive) between bacteria and the alumina surfaces (calculated according to Eq (2)) at 30 min, 48 h, and 96 h. Error bars represent standard error of means.

For both microorganisms, the 15 nm pore surfaces exerted the largest peak repulsive force ($F_{\max}$) followed by the 25 nm pore surfaces, with the 50 nm pore surface, 100 nm pore surface and the control exerting comparable, and relatively low $F_{\max}$. Figure 19 shows a linear decrease of cell counts (expressed as log CFU per unit area) as a function of $F_{\max}$, for both organisms and all three time points. The $F_{\max}$ exerted on *E. coli* is stronger as compared to that on *L. innocua*, hence the biomass accumulation is less.

The R^2 value of the regression lines was the weakest at 30 min, and the highest at 96 h. This can be explained at least in part by the improvement of the signal-to-noise ratio of the data

from 30 min (which showed the lowest number of cells attached) to 96 h (the highest number of cells). This correlation is very important, as it relates the bacterium-surface interaction forces with attachment and subsequent biofilm formation on the alumina surfaces for both microorganisms used in this study. This correlation offers significant insight into the mechanisms that control bacterial attachment and may be used as a predictive tool for the development of antifouling and antimicrobial surfaces.

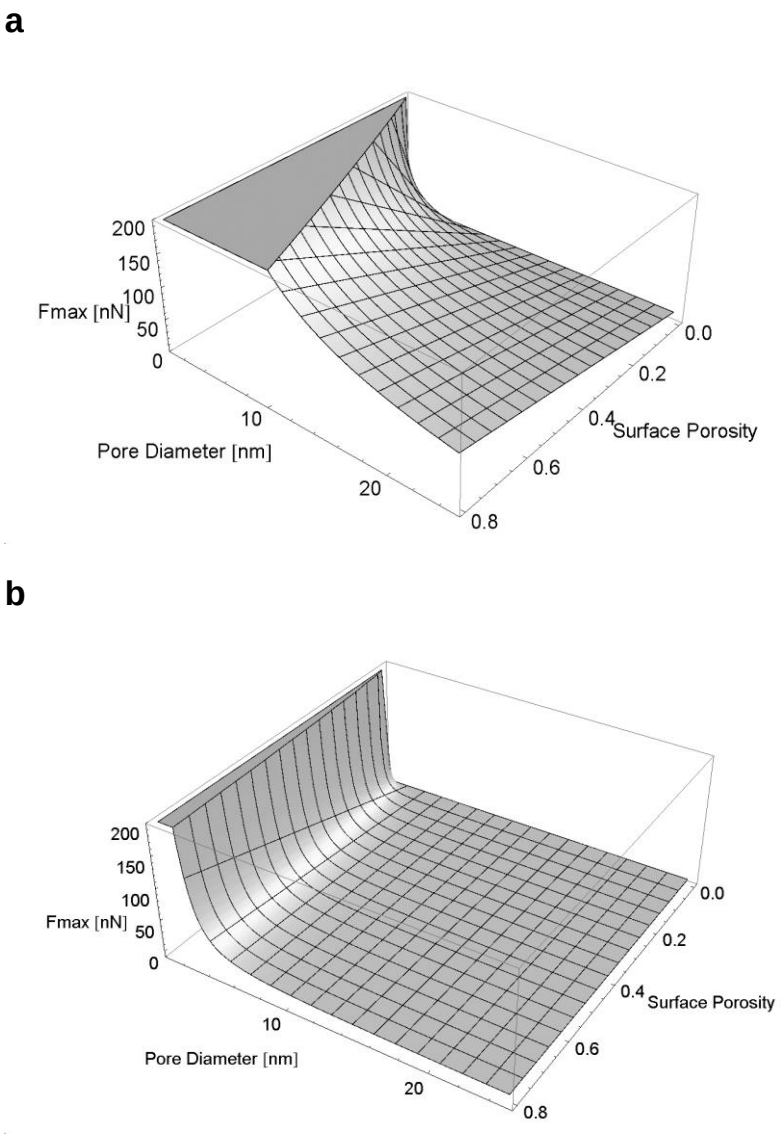

Figure 20. Theoretical predictions of the change in maximum (peak) repulsion force as a function of pore diameter and surface porosity, at fixed pore depth (1 μm) calculated for **(a)** *E. coli* and **(b)** *L. innocua*.

Furthermore, theoretical calculations have been performed to better understand the effect of various surface topological characteristics on the total interaction force. Figure 20 summarizes these calculations by showing the effect of pore diameter and surface porosity on $F_{\max}$ for both

challenge organisms used in this study. Pore diameter has a tremendous effect on the repulsive force, particularly at pore diameters below 20 nm, with repulsive forces increasing exponentially as pore diameter decreases at a fixed surface porosity. An increase in porosity at a fixed diameter induces a linear increase in the value of the repulsive force, while pore depth does not seem to have a significant effect above several tens of nanometers. This is well below the typical depth of pores of anodized surfaces, which are several micrometers deep. Hence, controlling the pore diameter, porosity and number of pores per unit area is key in tuning the total repulsive force and preventing initial attachment. It must also be noted that $F_{\max}$ exerted on *E. coli* ATCC 25922 varies more drastically in response to changes in porosity and pore diameter as compared to *L. innocua*, illustrating the significant role of cell surface properties in the attachment process. This suggests that theoretical calculations of the physicochemical interaction between each specific bacterium-surface pair are essential to making accurate predictions of bacterial attachment.

2.4.4. Role of bacterial appendages in the attachment process

To determine the effect of nanoscale surfaces on appendage-dependent attachment, an attachment assay was conducted using *E. coli* K12 strains of wild-type (WT) and appendage-deficient mutants. In the attachment assay, the number of cells attached per surface after 30 min of incubation with the 15 nm and 100 nm pore sizes surfaces was quantified. *E. coli* K12 was used for this study since there were no appendage-deficient mutants available for *E. coli* ATCC 25922, which was used in the rest of the study.

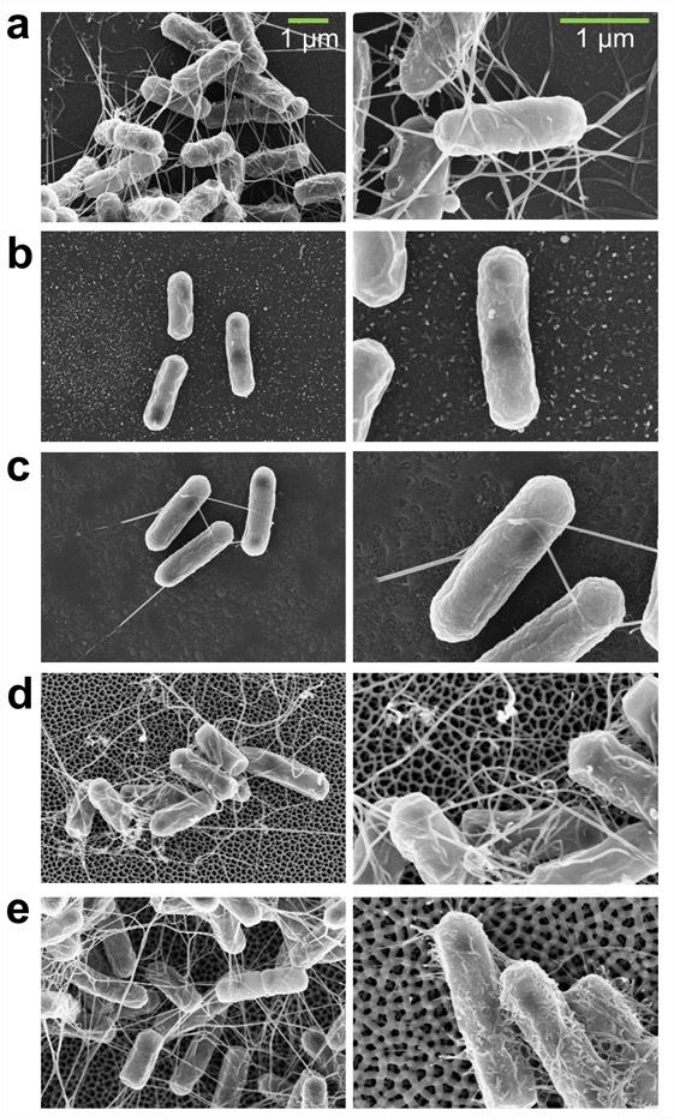

Figure 21. SEM images of *E. coli* cells attached to **(a)** nanosmooth, **(b)** 15 nm, **(c)** 25 nm, **(d)** 50 nm, and **(e)** 100 nm pore surfaces. Lower magnification images (left column) show microbial communities and higher magnification images (right column) show details of bacteria structures that physically interact with the surfaces.

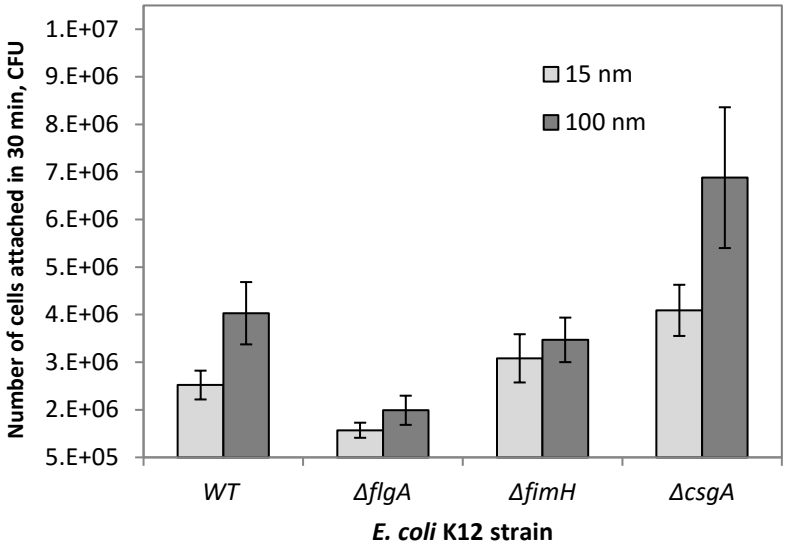

Figure 22. Attachment at 30 min by *E. coli* K12 wild-type, flagella-, fimbria- and curli-deficient mutants on 15 nm and 100 nm surfaces. Error bars represent standard error of means.

Compared to the wild-type strain, the flagellum-deficient mutant (*ΔflgA*) showed much lower attachment to both 15 nm and 100 nm surfaces as compared to the wild-type strain (Figure 22), suggesting that flagella have a significant role in attachment to the anodized surfaces. The difference in attachment between WT and the fimbriae-deficient mutant (*ΔfimH*) was negligible on either surface type, implying that fimbria may play a minor role in the initial attachment. Interestingly, the curli-deficient mutant (*ΔcsgA*) attached to both surfaces at the highest level among all *E. coli* K12 strains. Previous findings revealed that the loss of *csgA* expression could result in reduction of biofilm formation [39,40] and that curli have a significant role in the structural integrity of mature biofilm matrices [41]. The discrepancy could be due to the fact that short-term attachment rather than biofilm formation was assessed in this study.

Regarding the differences in behavior between the two surfaces, attachment to the 100 nm surface was higher than on the 15 nm surface, consistent with the observations from the attachment

study with *E. coli* ATCC 25922 and *L. innocua*. However, differences in attachment were statistically significant only for the wild type and the curli-deficient strains.

Measurements of water contact angles and zeta potential values of the wild-type and mutant *E. coli* K12 strains indicated that the genetic modifications did not result in any significant change in cell hydrophobicity or electrical charge. Therefore, the differences in attachment observed between the WT and appendage-deficient mutants were most likely biological in nature, highlighting the role of surface adhesins in the attachment. It is possible that the strength of attachment by the different strains to the two surfaces was different, with a potentially stronger attachment to the 100 nm surfaces, but this hypothesis will have to be tested in future experiments.

2.5. Conclusions

This study reveals the direct effect of the pore diameter of nanoporous anodic alumina on the attachment behavior and biofilm formation by Gram positive and Gram negative bacteria strains. Specifically, engineered nanoporous surfaces with pore diameters of 15 nm and 25 nm and relatively large surface porosity were able to effectively minimize attachment by *E. coli* spp. and *Listeria* spp., and possibly of other microorganisms. The physicochemical properties of the anodized surfaces, which are directly affected by pore diameter and surface porosity, and the cell surface, as well as surface appendages expressed by the bacterial cells, were shown to play an important role in attachment.

These findings can be used to design and fabricate affordable antifouling surfaces for food and water processing, dentistry or biomedical applications, with tremendous public health and economic benefits. Engineering nanoporous anodized surfaces with antifouling properties could

translate into virtually immediate applications, since technology transfer for using anodic surfaces in numerous applications can be very rapid.

REFERENCES

(1) Taylor, P.; Jorge, P.; Lourenço, A.; Pereira, M. O. New Trends in Peptide-Based Anti-Biofilm Strategies : A Review of Recent Achievements and Bioinformatic Approaches. *Biofouling* **2012**, *28* (November), 1033–1061.

(2) Bryers, J. D. Medical Biofilms. *Biotech. Bioeng.* **2009**, *100* (1), 1–18.

(3) Scharff, R. L. Economic Burden from Health Losses due to Foodborne Illness in the United States. *J. Food. Prot.* **2012**, *75* (1), 123–131.

(4) Rijnaarts, H. H. M.; Norde, W.; Lyklema, J.; Zehnder, A. J. B. DLVO and Steric Contributions to Bacterial Deposition in Media of Different Ionic Strengths. *Colloids Surf. B Biointerfaces* **1999**, *14* (1–4), 179–195.

(5) Verran, J.; Boyd, R. D. The Relationship between Substratum Surface Roughness and Microbiological and Organic Soiling : A Review. *Biofouling* **2001**, *17* (1), 59–71.

(6) Oliveira, R.; Azeredo, J.; Teixeira, P.; Fonseca, A. P. The Role of Hydrophobicity in Bacterial Adhesion. In *Biofilm community interactions: chance or necessity?*; BioLine for the Biofilm Club, 2001; pp 11–22.

(7) Mauclaire, L.; Brombacher, E.; Bünger, J. D.; Zinn, M. Factors Controlling Bacterial Attachment and Biofilm Formation on Medium-Chain-Length Polyhydroxyalkanoates (Mcl-PHAs). *Colloids Surf. B. Biointerfaces* **2010**, *76* (1), 104–111.

(8) Singh, A. V.; Vyas, V.; Patil, R.; Sharma, V.; Scopelliti, P. E.; Bongiorno, G.; Podestà, A.; Lenardi, C.; Gade, W. N.; Milani, P. Quantitative Characterization of the Influence of the Nanoscale Morphology of Nanostructured Surfaces on Bacterial Adhesion and Biofilm Formation. *PLoS One* **2011**, *6* (9), e25029.

(9) Boulangé-Petermann, L.; Rault, J.; Bellon-Fontaine, M. Adhesion of Streptococcus Thermophilus to Stainless Steel with Different Surface Topography and Roughness. *Biofouling* **1997**, *11* (3), 201–216.

(10) Tide, C.; Harkin, S. R.; Geesey, G. G.; Bremer, P. J.; Scholz, W. The Influence of Welding Procedures on Bacterial Colonization of Stainless Steel Weldments. *J. Food Eng.* **1999**, *42*, 85–96.

(11) Arnold, J. W.; Bailey, G. W. Surface Finishes on Stainless Steel Reduce Bacterial Attachment and Early Biofilm Formation: Scanning Electron and Atomic Force Microscopy Study. *Poult. Sci.* **2000**, *79* (12), 1839–1845.

(12) Medilanski, E.; Kaufmann, K.; Wick, L. Y.; Wanner, O.; Harms, H. Influence of the Surface Topography of Stainless Steel on Bacterial Adhesion. *Biofouling* **2002**, *18* (3), 193–203.

(13) Whitehead, K. a; Colligon, J.; Verran, J. Retention of Microbial Cells in Substratum Surface Features of Micrometer and Sub-Micrometer Dimensions. *Colloids Surf. B Biointerfaces* **2005**, *41* (2–3), 129–138.

(14) Verran, J.; Packer, A.; Kelly, P.; Whitehead, K. A. The Retention of Bacteria on Hygienic Surfaces Presenting Scratches of Microbial Dimensions. *Lett. Appl. Microbiol.* **2010**, *50* (3), 258–263.

(15) Díaz, C.; Schilardi, P. L.; Salvarezza, R. C.; de Mele, M. F. L. Nano/microscale Order Affects the Early Stages of Biofilm Formation on Metal Surfaces. *Langmuir* **2007**, *23* (22), 11206–11210.

(16) Xu, L.-C.; Siedlecki, C. A. Submicron-Textured Biomaterial Surface Reduces Staphylococcal Bacterial Adhesion and Biofilm Formation. *Acta Biomater.* **2012**, *8* (1), 72–81.

(17) Prigent-Combaret, C.; Prensier, G.; Le Thi, T. T.; Vidal, O.; Lejeune, P.; Dorel, C. Developmental Pathway for Biofilm Formation in Curli-Producing Escherichia Coli Strains: Role of Flagella, Curli and Colanic Acid. *Environ. microbiol.* **2000**, *2* (4), 450–464.

(18) Lemon, K. P.; Higgins, D. E.; Kolter, R. Flagellar Motility Is Critical for Listeria Monocytogenes Biofilm Formation. *J. Bacteriol.* **2007**, *189* (12), 4418–4424.

(19) Niba, E. T. E.; Naka, Y.; Nagase, M.; Mori, H.; Kitakawa, M. A Genome-Wide Approach to Identify the Genes Involved in Biofilm Formation in E. Coli. *DNA Res.* **2007**, *14* (6), 237–246.

(20) Friedlander, R. S.; Vlamakis, H.; Kim, P.; Khan, M.; Kolter, R.; Aizenberg, J. Bacterial Flagella Explore Microscale Hummocks and Hollows to Increase Adhesion. *Proc. Natl. Acad. Sci. U. S. A.* **2013**, *110* (14), 1–6.

(21) Hsu, L.; Fang, J.; Borca-Tasciuc, D.; Worobo, R.; Moraru, C. I. The Effect of Micro- and Nanoscale Topography on the Adhesion of Bacterial Cells to Solid Surfaces. *Appl. Environ. Microbiol.* **2013**.

(22) Park, M. R.; Banks, M. K.; Applegate, B.; Webster, T. J. Influence of Nanophase Titania Topography on Bacterial Attachment and Metabolism. *Int J Nanomedicine* **2008**, *3* (4), 497–504.

(23) Puckett, S. D.; Taylor, E.; Raimondo, T.; Webster, T. J. The Relationship between the Nanostructure of Titanium Surfaces and Bacterial Attachment. *Biomaterials* **2010**, *31* (4), 706–713.

(24) Hori, K.; Matsumoto, S. Bacterial Adhesion: From Mechanism to Control. *Biochem. Eng. J.* **2010**, *48* (3), 424–434.

(25) Thomas, P.; Benaben, P. Preparation of Highly Ordered Nanoporous Alumina by Two Step Anodising: Process and Industrial Applications. *Trans. Inst. Met. Finish.* **2007**, *85* (4), 212–216.

(26) Masuda, H.; Yada, K.; Osaka, A. Self-Ordering of Cell Configuration of Anodic Porous Alumina with Large-Size Pores in Phosphoric Acid Solution. *Jpn. J. Appl. Phys.* **1998**, *37* (11A), L1340–L1342.

(27) Jessensky, O.; Müller, F.; Gösele, U. Self-Organized Formation of Hexagonal Pore Arrays in Anodic Alumina. *Appl. Phys. Lett.* **1998**, *72* (10), 1173.

(28) Kim, J. K.; Harrison, M. A. Surrogate Selection for Escherichia Coli O157:H7 Based on Cryotolerance and Attachment to Romaine Lettuce. *J. Food Prot.* **2009**, *72* (7), 1385–1391.

(29) Saini, J. K.; Marsden, J. L.; Fung, D. Y. C.; Crozier-Dodson, B. A. Evaluation of Potential for Translocation of Listeria Monocytogenes from Floor Drains to Food Contact Surfaces in the Surrounding Environment Using Listeria Innocua as a Surrogate. *Adv. Microbiol.* **2012**, *2* (4), 565–570.

(30) Heydorn, A.; Nielsen, a T.; Hentzer, M.; Sternberg, C.; Givskov, M.; Ersbøll, B. K.; Molin, S. Quantification of Biofilm Structures by the Novel Computer Program COMSTAT. *Microbiology* **2000**, *146*, 2395–2407.

(31) Baba, T.; Ara, T.; Hasegawa, M.; Takai, Y.; Okumura, Y.; Baba, M.; Datsenko, K. a; Tomita, M.; Wanner, B. L.; Mori, H. Construction of Escherichia Coli K-12 in-Frame, Single-Gene Knockout Mutants: The Keio Collection. *Mol. Syst. Biol.* **2006**, *2*, 2006.0008.

(32) Busscher, H. J.; Weerkamp, a. H.; van der Mei, H. C.; van pelt, A. W.; de jong, H. P.; Arends, J. Bacterial Cell Surfaces and Its Relevance for Measurement of the Surface Free Energy of Bacterial Cell Surfaces and Its Relevance for Adhesion. *Appl. Environ. Microbiol.* **1984**, *48* (5), 980–983.

(33) Li, B.; Logan, B. E. Bacterial Adhesion to Glass and Metal-Oxide Surfaces. *Colloids Surf. B. Biointerfaces* **2004**, *36* (2), 81–90.

(34) Whitchurch, C. B.; Tolker-Nielsen, T.; Ragas, P. C.; Mattick, J. S. Extracellular DNA Required for Bacterial Biofilm Formation. *Science (80-.).* **2002**, *295*, 1487.

(35) Harmsen, M.; Lappann, M.; Knøchel, S.; Molin, S. Role of Extracellular DNA during Biofilm Formation by Listeria Monocytogenes. *Appl. Environ. Microbiol.* **2010**, *76* (7), 2271–2279.

(36) Schilling, K. M.; Bowen, W. H. Glucans Synthesized in Situ in Experimental Salivary Pellicle Function as Specific Binding Sites for Streptococcus Mutans. *Infect. Immun.* **1992**, *60* (1), 284–295.

(37) Rizzello, L.; Sorce, B.; Sabella, S.; Vecchio, G.; Galeone, A.; Brunetti, V.; Cingolani, R.; Pompa, P. P. Impact of Nanoscale Topography on Genomics and Proteomics of Adherent Bacteria. *ACS Nano* **2011**, *5* (3), 1865–1876.

(38) Naves, P.; del Prado, G.; Huelves, L.; Gracia, M.; Ruiz, V.; Blanco, J.; Dahbi, G.; Blanco, M.; Ponte, M. D. C.; Soriano, F. Correlation between Virulence Factors and in Vitro Biofilm Formation by Escherichia Coli Strains. *Microb. Pathog.* **2008**, *45* (2), 86–91.

(39) Dorel, C.; Vidal, O.; Prigent-Combaret, C.; Vallet, I.; Lejeune, P. Involvement of the Cpx Signal Transduction Pathway of E. Coli in Biofilm Formation. *FEMS Microbiol. Lett.* **1999**, *178* (1), 169–175.

(40) Vidal, O.; Longin, R.; Prigent-combaret, C.; Hooreman, M.; Lejeune, P. Isolation of an Escherichia Coli K-12 Mutant Strain Able To Form Biofilms on Inert Surfaces : Involvement of a New ompR Allele That Increases Curli Expression. *J. Bacteriol.* **1998**, *180* (9), 2442–2449.

(41) Serra, D. O.; Richter, A. M.; Klauck, G.; Mika, F.; Hengge, R. Microanatomy at Cellular Resolution and Spatial Order of Physiological Differentiation in a Bacterial Biofilm. *MBio* **2013**, *4* (2), e00103-13.

CHAPTER THREE

BACTERIAL ATTACHMENT AND BIOFILM FORMATION ON SURFACES ARE REDUCED BY SMALL-DIAMETER NANOSCALE PORES [2]

3.1. Abstract

Prevention of biofilm formation by bacteria is of critical importance to areas that directly affect human health and life including medicine, dentistry, food processing and water treatment. This work showcases an effective and affordable solution for reducing attachment and biofilm formation by several pathogenic bacteria commonly associated with foodborne illnesses and medical infections. Our approach exploits anodization to create alumina surfaces with cylindrical nanopores with diameters ranging from 15 to 100 nm, perpendicular to the surface. The anodic surfaces were evaluated for attachment by Escherichia coli, Listeria monocytogenes, Staphylococcus aureus and Staphylococcus epidermidis. Cell–surface interaction forces were calculated and related to attachment. We found that anodic alumina surfaces with pore diameters of 15 and 25nm were able to effectively minimize bacterial attachment or biofilm formation by all the microorganisms tested. Using a predictive physicochemical approach on the basis of the extended Derjaguin and Landau, Verwey and Overbeek (XDLVO) theory, we attributed the observed effects largely to the repulsive forces, primarily electrostatic and acid–base forces, which were greatly enhanced by the large surface area originating from the high density, small-diameter pores. We also demonstrate how this predictive approach could be used to optimize different elements of surface topography, particularly pore diameter, and density, for further enhancing the

[2] The main content of this chapter (except section 3.5.2) is published in the *npj Biofilms and Microbiomes* paper: Bacterial attachment and biofilm formation on surfaces are reduced by small-diameter nanoscale pores: how small is small enough? *npj Biofilms Microbiomes* 2015, 1 (August), 15022. Authors: Guoping Feng, Yifan Cheng, Shu-Yi Wang, Diana A. Borca-Tasciuc, Randy W. Worobo, and Carmen I. Moraru.

observed bacteria-repelling effects. We demonstrate that anodic nanoporous surfaces can effectively reduce bacterial attachment. These findings are expected to have immediate, far-reaching implications and commercial applications, primarily in health care and the food industry.

3.2. Introduction

Biofilms are the prevailing lifestyle of bacteria in most natural environments. They consist of microbial communities that usually accumulate at solid-liquid interfaces and are entrapped in a matrix of highly hydrated extracellular polymeric substances (EPS) [1]. The quiescent lifestyle of microbial cells living in such a densely packed diffusion barrier is responsible for their high tolerance to environmental stresses [2]. Cells in biofilms have been deemed 100 to 1000 times more resistant to antibiotics and disinfecting agents than planktonic cells [3,4]. Biofilm formation by pathogenic bacteria has deleterious, sometimes fatal consequences, and leads to severe contamination problems in medicine, dentistry, food processing, water treatment and other areas that directly affect human health and life. For instance, it is estimated that approximately 80% of all medical infections are derived from biofilm growth of pathogens [5]. Biofilms formed by pathogens in food processing plants are a major culprit in spreading of foodborne diseases, which claim thousands of lives and amount to losses of about $78 billion/year in the US alone [6].

Most studies attempting to mitigate the effects of biofilms focus on interventions aimed to kill microbial cells in biofilms already present on solid surfaces [7,8]. However, such strategies have limited efficacy due to bacterial persistence and resistance in preformed biofilms [9,10]. Surface modification is emerging as a promising strategy for preventing biofilm formation on abiotic surfaces. There is increasing evidence that bacterial attachment and subsequent biofilm formation are significantly impacted by surface topography [11–13]. For surfaces with topographic features at the micrometric scale, comparable with the size of prokaryotic cells, cells tend to positions

themselves such that they maximize contact area with the surface, which favors attachment [11,12]. Surfaces with topographic features of dimensions much smaller than microbial cells, in the submicrometric or nanometric range, have been reported to inhibit attachment by reducing the contact area between bacteria cells and the surface [11,13]. Additionally, surface topography at the nanoscale can create energetic situations unfavorable for bacterial attachment, and induce repulsive surface-bacteria interaction forces that impair attachment and subsequent biofilm formation [14,15]. While most nanostructuring methods available today require cleanroom technologies and are prohibitively expensive for large scale applications, anodization is an inexpensive, commercially available electrochemical method that allows relatively easy control of surface features in the nanometer range [11].

A recent study by our research group showed that anodic alumina surfaces with nanoscale cylindrical pores of diameters smaller than 25 nm are able to minimize bacterial attachment by the nonpathogenic *Escherichia coli* and *Listeria innocua* [15]. The observed effects were largely attributed to additional repulsive forces contributed by the large surface area of the surfaces with a high density of small diameter pores. The current report builds on these promising findings and tests the ability of anodic alumina surfaces to minimize bacterial attachment for several pathogenic strains. A quantitative prediction of bacteria – surface interaction forces is used to understand how to further optimize surface topographical features and physicochemical properties and thus create surfaces with a stronger ability to prevent bacterial attachment and biofilm formation.

As challenge organisms, four of the most feared pathogens associated with medical, biomedical or food processing environments were selected: *E. coli* O157:H7, *L. monocytogenes*, *Staphylococcus aureus* and *Staphylococcus epidermidis*, along with the non-pathogenic *E. coli* K12. *L. monocytogenes* can cause illness, death, and abortion, and is of particular concern for

immuno-compromised individuals and pregnant women. CDC estimates that about 2,500 listeriosis and 500 associated deaths occur yearly [16]. The ubiquitous *L. monocytogenes* can be transmitted through raw foods, the environment, utensils or processing equipment [17–19]. Infection with *E. coli* O157:H7 can lead to severe foodborne illness, specifically hemorrhagic diarrhea and hemolytic uremic syndrome [16,20,21]. Contamination with *S. aureus* is the root cause for a range of illnesses, from food poisoning to infections of the skin and soft tissue, to respiratory, bone, joint and endovascular disorders; *S. aureus* is the most frequently isolated pathogen from wound infections [22,23]. *S. epidermidis* has been associated with bacteremia, catheter-related infection, central nervous system shunt infection, endocarditis, urinary tract infection, surgical site infection and endophthalmitis [24].

3.3. Materials and Methods

3.3.1. Surface fabrication

Nanoporous aluminum oxide (alumina) surfaces with pore diameters of 15 nm, 25 nm, 50 nm and 100 nm were prepared by two-step anodization of high purity aluminum (99.99%, Alfa Aesar), which has been described in detail before [15,25]. The aluminum substrate was first subjected to mechanical and electrochemical polishing, with an intermediate annealing process meant to release internal stresses. The polished substrate was immersed in an etchant to remove the thin alumina layer formed during electrochemical polishing. The first anodization step was carried out at room temperature using a setup similar to that used for electrochemical polishing. The voltage and anodizing mixture depended on the pore size. The first porous alumina layer was etched away and a second anodization step was performed, during which pore growth was initiated from dents left over by the nanopores in the first layer, resulting in regular surface features [25,26]. Nanosmooth alumina surfaces (R_{rms} < 1 nm) of 10×10×0.5 mm (Alfa Aesar, Ward Hill, MA) were used as a

control. The nanosmooth control used here was not identical to that used in our previous study [15], and its surface properties were slightly different.

3.3.2. Bacteria attachment

Cultures of *E. coli* O157:H7 ATCC 43894, *E. coli* K12, *L. monocytogenes* 10403S, *S. aureus* 9144, *S. epidermidis* ATCC 35984 were maintained in tryptic soy broth (TSB) with 20% (v./v.) glycerol at -80°C. Cultures were reactivated on tryptic soy agar (TSA) at 37°C for 24 h. They were grown in TSB for 24 h and sub-cultured in TSB for 16 h at 37°C. The experimental procedure was described in detail before [15]. Briefly, 16 h-old cultures of planktonic cells at a diluted concentration of ~10^7 CFU/ml were incubated statically for 48 h with vertically placed alumina surfaces (with pores of 15 nm, 25 nm, 50 nm, 100 nm, and a nanosmooth alumina surface as a control), at the optimal growth temperature for each bacterial strain, then retrieved and evaluated for bacterial attachment. An incubation time of 48 h was chosen since it was previously observed that this time point allowed bacteria to attach to the surfaces in sufficient numbers for a meaningful quantitative assessment, but without significant biofilm formation [15]. Surfaces were placed vertically to reflect true attachment and minimize the effect of cell sedimentation due to gravity.

3.3.3. Confocal laser scanning microscopy (CLSM)

The surfaces with attached cells were gently removed from the culture and rinsed in sterile saline solution (0.15 M NaCl), 3 times, to remove lightly attached cells. The bacterial biomass was labelled with Syto 9 (Molecular Probes Inc., Eugene, OR). A Zeiss 710 CLSM equipped with inverted objectives was used to acquire 3D images of live bacteria, as described before [15]. For every type of surface, six replicates (two surfaces per each of three independent experiments) were used. On each sampled surface, at least 5 randomly selected and evenly spaced fields (338.4×338.4

μm^2) were scanned. Three-dimensional images of biomass matrices were constructed using Volocity (version 5.2.1, PerkinElmer, Waltham, MA).

3.3.4. Biomass quantification

The total biomass and surface coverage were quantified using COMSTAT, a computer program designed specifically for this purpose [27]. A threshold value of 3 was assigned to all individual image stacks. Quantified parameters were: biomass accumulation ($\mu m^3/\mu m^2$), obtained by dividing the overall biomass volume by the substratum area; and layer coverage, given by the percentage of the area occupied by bacteria in each optical layer.

3.3.5. Scanning electron microscopy (SEM)

Visualization of biomass structures was conducted with a Zeiss LEO 1550 field emission SEM, and images acquired with the SmartSEM software (Carl Zeiss Microscopy, LLC, Germany). Surfaces were retrieved at 48 h and rinsed in saline solution to remove lightly attached cells. The biomass on the surfaces was fixed using 2.5% (w/v) glutaraldehyde in 0.05 M sodium cacodylate buffer at 4°C for 2 h. Samples were then rinsed in cacodylate buffer three times, 5 min each time, and subjected to secondary fixation with 1% (w/v) osmium tetroxide in cacodylate buffer, for 1 h. The fixated samples were rinsed in cacodylate buffer 3 times, then dehydrated using gradient ethanol solutions of 25% (v/v), 50%, 70%, 95%, 100% and 100%, for 10 min each, followed by critical point-drying with carbon dioxide. Dried surfaces were mounted to SEM stubs and coated with evaporated carbon. A voltage of 1 to 5 kV was used, depending on the sample.

3.3.6. Contact angle measurement

Contact angles of water, glycerol, and diiodomethane on both bacterial cell lawns and alumina substrates were determined by the sessile drop method with a Rame-Hart 500 goniometer (Rame-Hart Inc., Succasunna, NJ, USA), as described before [15].

3.3.7. Surface electric charges

The zeta potential of the bacterial cells was measured using a Malvern Zetasizer nano-ZS with disposable folded capillary cells (Malvern Instruments, Malvern, UK), as described previously [15]. Zeta potential of the alumina was taken from Li and Logan (2004) [28].

3.3.8. Statistical analysis

One-way analysis of variance (ANOVA) and post-ANOVA Tukey's test were used to compare multiple means. All analyses were performed with JMP Pro 11 (SAS Institute, Cary, NJ). The adjusted XDLVO model was constructed and computed using Mathematica 9.0 (Wolfram, Champaign, IL).

3.4. Results

Consistent with our previous observations [15], presence of bacteria on the anodic surfaces with pores of 15 nm and 25 nm was largely reduced compared to the anodized surfaces with larger pore sizes, for all strains. Both visual observations (Figure 23) and the quantitative biomass evaluation (Figure 24) showed that the extent of biomass accumulation varied considerably among the tested microorganisms. For *E. coli* K12, *E. coli* O157:H7 and *L. monocytogenes*, a thin layer of uniformly distributed cells was observed on all surfaces, while for *S. aureus* and *S. epidermidis*, both prolific biofilm formers, biomass accumulation was much more significant, particularly on the surfaces with pore diameters above 50 nm (Figure 24, left panels). At 48 h the biomass accumulation for *E. coli* O157:H7 on the nanosmooth, 15 nm, 25 nm, 50 nm and 100 nm surfaces was 0.32 $\mu m^3/\mu m^2$, 0.36 $\mu m^3/\mu m^2$, 0.47 $\mu m^3/\mu m^2$, 0.86 $\mu m^3/\mu m^2$ and 1.51 $\mu m^3/\mu m^2$, respectively. The biomass accumulation for *E. coli* K-12 was slightly lower than for *E. coli* O157:H7. For *L. monocytogenes*, the biomass accumulation was about one order of magnitude higher than for the

E. coli strains, ranging from 4.27 $\mu m^3/\mu m^2$ on 15 nm surfaces to 16.40 $\mu m^3/\mu m^2$ on 100 nm surfaces. Biomass accumulation by *S. aureus* and *S. epidermidis* followed a similar trend but was much more pronounced compared to the two *E. coli* strains and *L. monocytogenes*. *S. aureus* had the lowest biomass accumulation on the 15 nm surface (16.91 $\mu m^3/\mu m^2$) and the highest on the 100 nm surface (28.19 $\mu m^3/\mu m^2$). *S. epidermidis* had the lowest biomass on the 25 nm surface (25.54 $\mu m^3/\mu m^2$) and the highest on the nanosmooth control (50.56 $\mu m^3/\mu m^2$). The thickness of the *S. epidermidis* biomass often exceeded 100 µm, several times higher than for any of the other strains tested. For the 100 nm surfaces, 48 h biomass accumulation by *S. epidermidis* had the clear traits of a dense biofilm and often included microcolonies (Figure 23, bottom right). As a note, the nanosmooth controls used in the current work were different than those used in our previous study [15]. This resulted in slightly different levels of biomass accumulation than previously reported for the nanosmooth alumina, but the attachment trends were maintained.

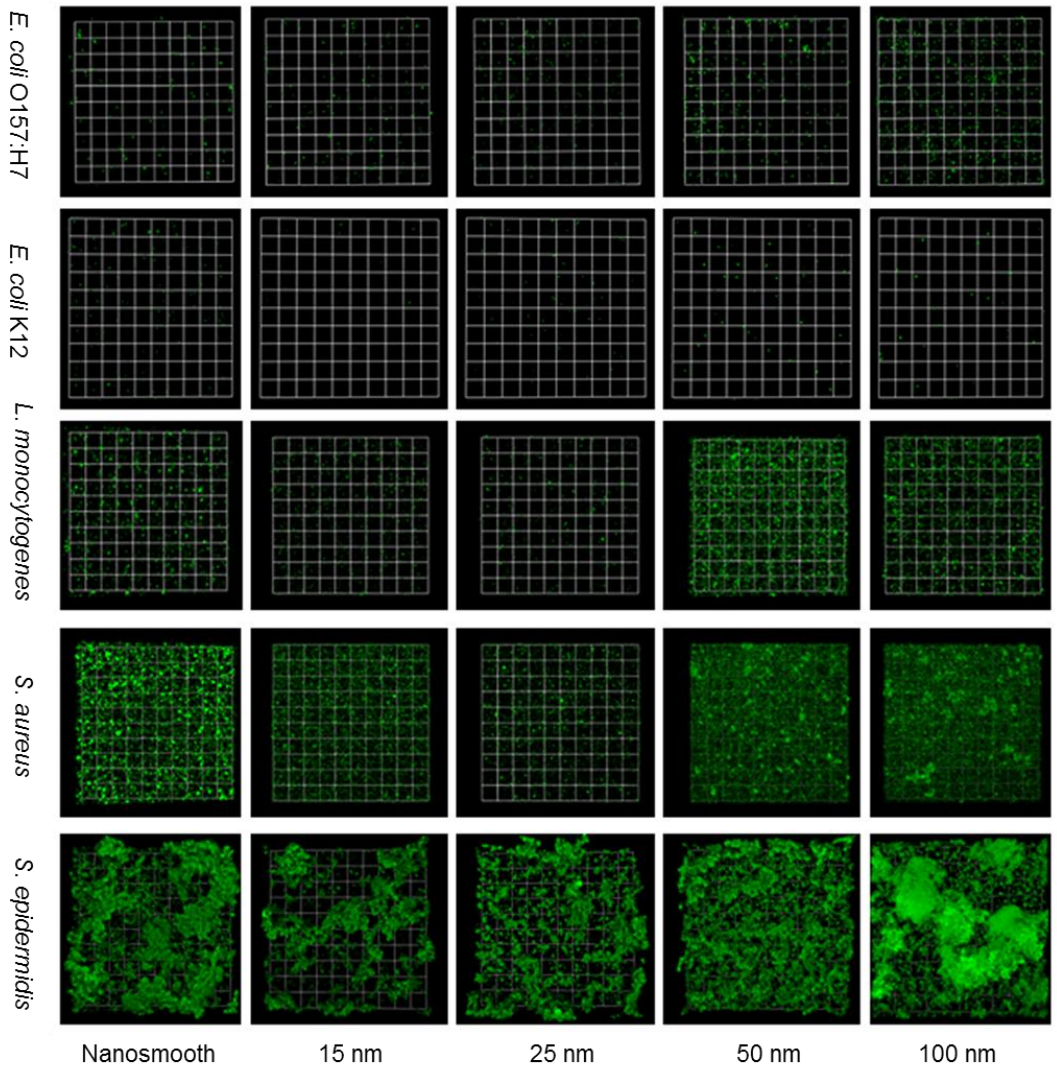

Figure 23. Constructed confocal laser scanning microscopy (CLSM) three-dimensional images of 48-hour-old biofilms of *E. coli* O157:H7, *E. coli* K12, *L. monocytogenes*, *S. aureus* and *S. epidermidis* on nanosmooth alumina (control) and anodized surfaces of 15, 25, 50 and 100nm pore diameter. The presented images have biomass accumulation close to the average for their surface type so that images are representative. Scale units (small grid) are 34 µm in length.

Overall, the trend in biomass accumulation on the anodic alumina surfaces by all strains agrees with our previous observations [15]. Due to some variability in the data, not all differences in biomass accumulation among surface types were statistically significant ($P<0.05$). Nonetheless, a

closer analysis of the biomass structure further substantiates the differences among surface types. We generated vertical three-dimensional CLSM scans of the biomass structure for all anodic alumina surfaces, in 1 µm vertical increments, and calculated the surface coverage by biofilm for each layer. The right panels in Figure 24 show surface coverage at different distances from the substratum for the four pathogenic strains. For all strains, biofilm surface coverage was lowest for the 15 nm and 25 nm surfaces and highest for the 50 nm and 100 nm surfaces. For the weak biofilm former *E. coli* O157:H7, maximum coverage ranged between 1% on the 15 nm surfaces and 4% on the 100 nm surfaces. The most striking differences in coverage among surfaces were observed for *L. monocytogenes*, for which maximum coverage on the surfaces with small pore sizes (about 20%) was fourfold smaller than on surfaces with larger pore sizes (about 80%). The prolific biofilm former *S. epidermidis* had high coverage on all surfaces, ranging from a low 61% on the 25 nm surfaces to a high 90% on the 50 nm surfaces. While for the other strains significant coverage was found mostly within a few µm from the surface, for *S. epidermidis* biomass coverage was very high even tens of µm from the surface.

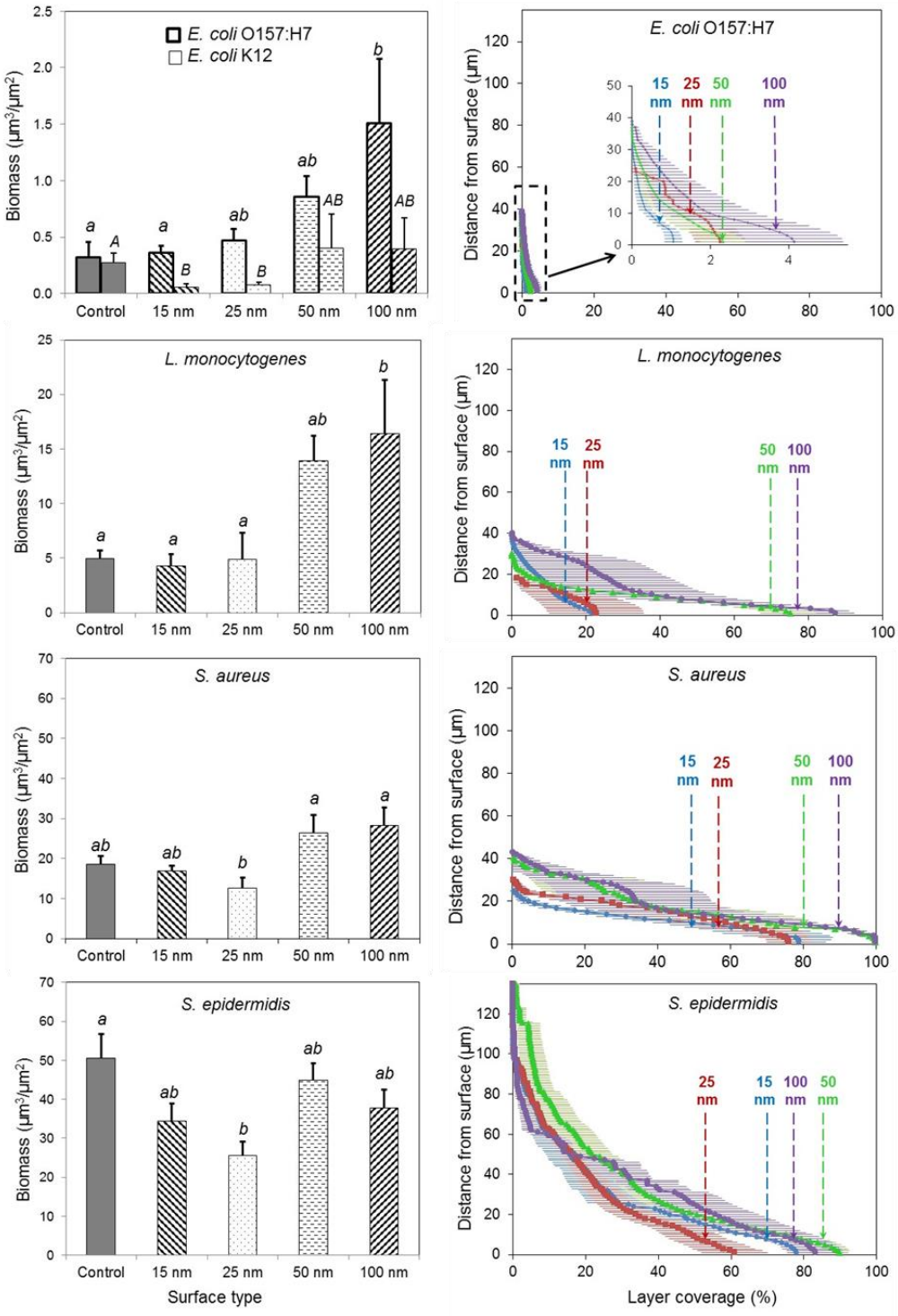

Figure 24. Differences in biomass accumulation over 48 h by *E. coli*, *L. monocytogenes*, *S. aureus* and *S. epidermidis* among alumina surfaces. Left panels: Quantified average values of biomass ($\mu m^3/\mu m^2$) accumulated on nanosmooth alumina, and anodized surfaces of 15 nm, 25 nm, 50

nm and 100 nm pore diameter. Values not connected by the same letter are statistically different from each other (P<0.05). Right panels: Layer coverage as a function of distance from the surface.

To further investigate the biomass structure, we conducted SEM visualization of the surfaces with the largest pore size (100 nm), which had either the largest or second largest biomass accumulation. It should be noted that the SEM images cannot be used for quantitative purposes, since some cell detachment from the surfaces may have occurred during SEM sample preparation. Figure 25 shows SEM micrographs for *S. aureus* (left) and *S. epidermidis* (right). For *S. aureus*, a single layer of cells was generally observed, with a minimal amount of extracellular material. *S. epidermidis*, on the other hand, showed substantial, highly structured, vertically grown biofilms, with a high density of bacterial cells tightly intertwined in a matrix of extracellular material, which is very typical of *S. epidermidis* biofilms [29]. The tremendous biofilm forming ability of *S. epidermidis* has been attributed to a large extent to the contribution of specific biological factors, mainly the polysaccharide intercellular adhesin (PIA) encoded by the intercellular adhesion (*ica*) locus [30,31]. All other bacterial strains showed a single layer of cells and no significant indication of extracellular substances (images not shown). Based on this corroborated evidence, in the subsequent discussion we will refer to the biomass accumulation as attached cells for all strains except *S. epidermidis,* for which a biofilm was formed.

Overall, this study confirms our previous findings [15], and clearly shows that the small nanoscale pore anodic alumina surfaces can effectively limit cell attachment and biofilm formation by a range of bacteria relevant for medical, biomedical and food processing applications. The trend was similar regardless of Gram-positive or Gram-negative status, rod or coccus shape, or the ability of the cells to express appendages under the conditions tested.

Bacterial attachment correlates with surface – bacteria interaction forces

Previously, we found strong evidence of a correlation between attachment by two bacteria strains and the overall cell-surface interaction force, calculated using the extended Derjaguin and Landau, Verwey and Overbeek (XDLVO) theory [15]. One important prediction made using this model was the maximum repulsive force that a bacterial cell needs to overcome in order to come into direct contact with a surface, termed "F_{max}". We were able to show that as F_{max} increased, the number of bacteria attached to a surface decreased [15]. Therefore, the XDLVO predictive approach was used to estimate bacteria-surface interaction forces for the strains tested in this study. Predictions were limited to those strains that did not show biofilm formation over the 48 h duration of the test: *E. coli* O157:H7, *E. coli* K-12, *L. monocytogenes*, and *S. aureus*. *S. epidermidis* was not included in these predictions because the presence of a significant amount of extracellular material did not allow an accurate estimation of the number of cells (**Figure 25**).

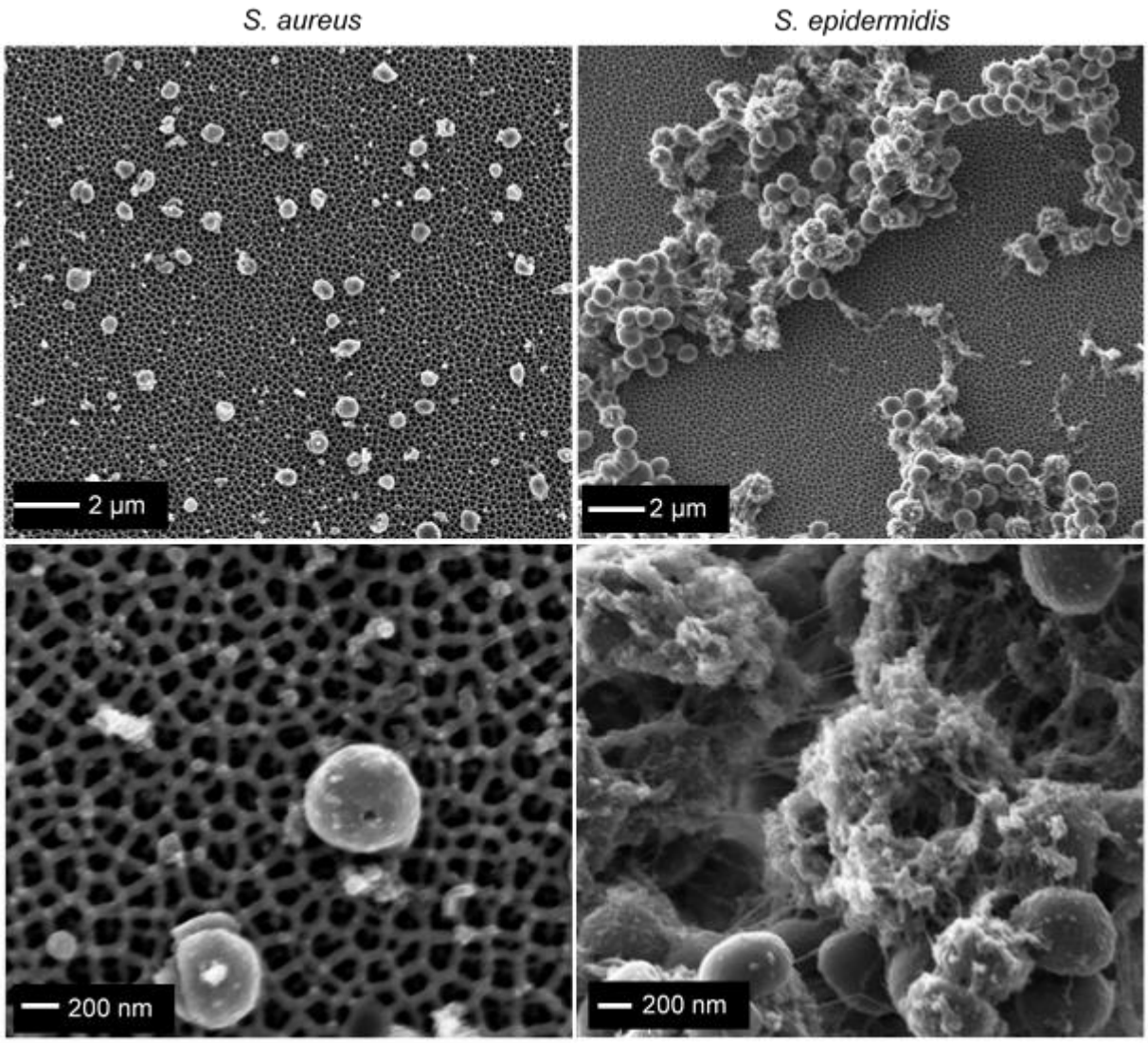

Figure 25. Scanning electron microscopy images of *S. aureus* (left images) and *S. epidermidis* cells (right images) at low magnification (upper) and high magnification (lower) after 48 h contact time with anodic alumina surfaces with 100 nm pore diameter. Bottom right image shows *S. epidermidis* cells entrapped in a matrix of extracellular material.

Cell properties required by the model were determined experimentally as described in the Methods section, and their measured values are summarized in **Table 4**. When applying the XDLVO model, the following simplifying assumptions were made: *(i)* all cells were assumed of spherical shape, and for rod-shaped bacteria (*E. coli* and *Listeria*) an equivalent radius was

calculated; *(ii)* surfaces have a fully wetting (Wenzel) behavior [32] and *(iii)* each surface was assumed to be an infinite planar surface relative to a bacterial cell. The nutritive broth was approximated as a 1:1 type electrolyte solution of ionic strength 0.1 M, at pH 7 and a temperature of 310 K (or 37 ºC). The surface properties are included in Table 2 (Chapter One), and the other constants used in the calculations in Table 1 (Chapter One).

The overall interaction force between a bacterium cell and the anodic alumina surfaces, $F_{\mathrm{Total}}^{\mathrm{XDLVO}}$, was calculated by the vector addition of three force components: electrostatic force (F_{EL}), acid-base interaction force (F_{AB}), and Lifshitz-van der Waals interaction force (F_{LW}). Since all forces are affected by the nanopores underneath the cells, they were adjusted to take into consideration this effect (denoted as 'Adj'), as previously shown in eq.(2) of Chapter One:

$$F_{\mathrm{Total}}^{\mathrm{XDLVO}} = F_{\mathrm{LW}}^{\mathrm{Adj}} + F_{\mathrm{AB}}^{\mathrm{Adj}} + F_{\mathrm{EL}}^{\mathrm{Adj}}$$

The full expression of Eq.1 and the derivation of its components are presented in detail in our previous study [15]. Briefly, the Lifshitz-van der Waals interaction force between the cells and the surfaces ($F_{\mathrm{LW}}^{\mathrm{Adj}}$) was calculated using the retarded Hamaker expression. The acid-base interaction force ($F_{\mathrm{AB}}^{\mathrm{Adj}}$), which incorporated the effect of surface energy, was calculated using the extended Young equation [33]. Since acid-base interactions are short range interactions, it was considered that only the top rim of the vertical surface of the cylindrical nanopores (2 nm from the surface) effectively contributes to the acid-base interaction. This portion of the internal surface of the cylindrical pores was approximated as a ring of hemispheres distributed uniformly along the circumference. The repulsion force exerted on one bacterium by the total number of cylindrical walls underneath that cell was calculated considering the pore diameter and surface porosity, as well as the radius of the effective circular interaction area for each type of bacteria.

The electrostatic interaction force ($F_{\mathrm{EL}}^{\mathrm{Adj}}$) was calculated for each pore and its surrounding area and the total force was determined by multiplying the value of this force by the number of pores underneath one bacterium cell. An example of the contribution of nanoscale topographical features to the magnitude and spatial distribution of interaction forces, the specific F_{EL} (electrostatic force per unit area, or "electrostatic pressure") exerted on a bacterial cell by the surface, plotted as a function of the radial distance from the center of a cylindrical pore, is shown in Figure 9a. Regardless of pore size, the vertical walls of the cylindrical pores from the porous anodic surfaces contributed to an increase in the electrostatic force compared to that generated by a smooth surface. Figure 26 shows both a schematic representation of the total electrostatic forces acting on a *E. coli* O157:H7 cell (left), and the field of electrostatic forces contributed by a surface area equivalent to a hexagonal array of 15 nm pores (right), at a cell-surface separation distance where electrostatic forces are significant for this bacterial strain. The force field plot on the right clearly shows that the repulsion exerted by the 15 nm surface greatly exceed the repulsion by the nanosmooth surface for *E. coli* O157:H7, which is consistent with the biomass accumulation shown in Figure 23 and Figure 24. Similar plots can be generated for the other forces.

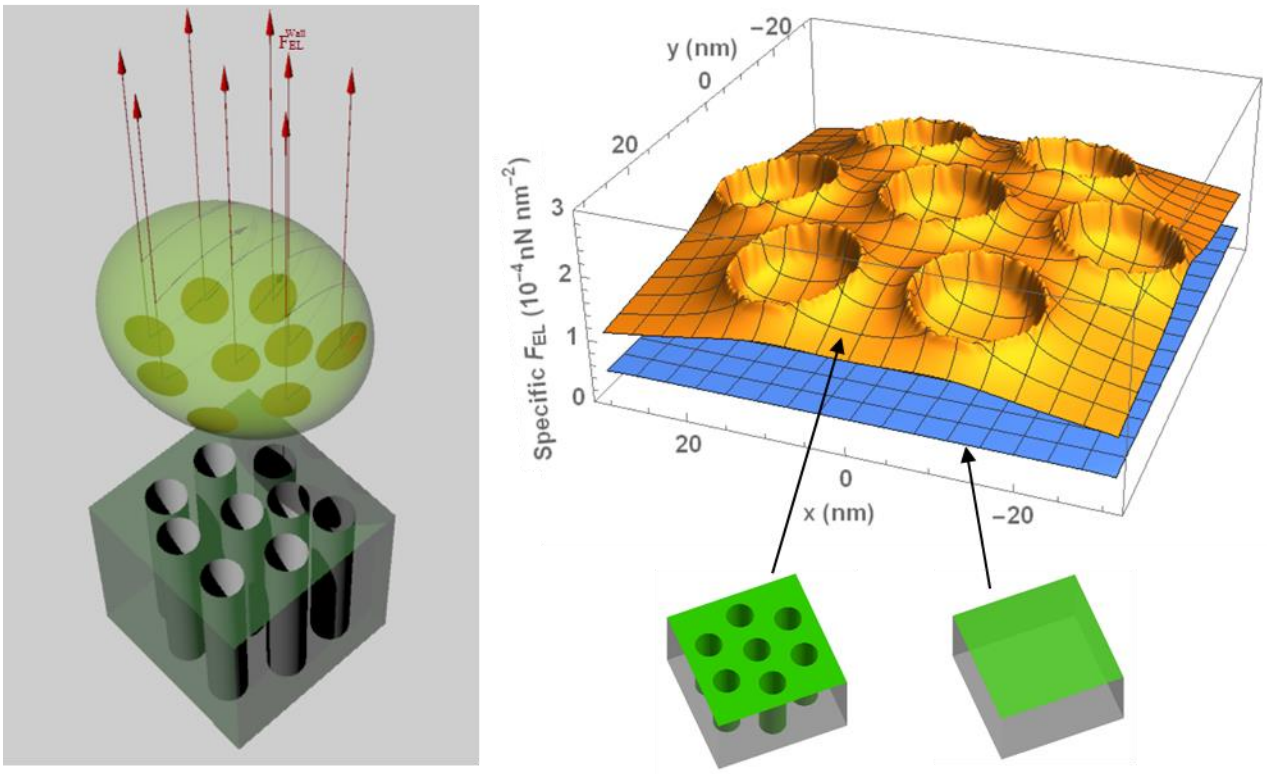

Figure 26. Electrostatic repelling force field exerted on bacterial cells by the nanoporous surface. **Left**: schematic representation of the electrostatic repelling forces exerted on a bacterial cell by the nanopores located directly underneath the cell. **Right**: spatial distribution of the electrostatic repulsive force field exerted on *E. coli* O157:H7 cells by an anodic alumina surface with cylindrical pores of 15 nm diameter and 2259 nm pore depth (top plot) compared to a smooth alumina surface (bottom plot), at a cell-surface separation distance of 0.2 nm. The surface components contributing to the force fields are illustrated in green.

The total cell-surface interaction force was then calculated as a function of the cell-surface separation distance (Figure 27). In close proximity of the surface, ranging from fractions of a nanometer to several nanometers, depending on the bacterial strain, the bacterium-surface interaction force was attractive for all surface-strain pairs, due to the short range attractive Lifshitz-

van der Waals forces. At separation distances beyond a few nanometers, the repulsive electrostatic and acid-base forces become dominant for all strains. For the anodic surfaces with the smallest pores, this contribution is particularly significant due to the large number of cylindrical pores per surface area. Consequently, the total repelling force ($F_{\text{Total}}^{\text{XDLVO}}$) is particularly high for the 15 nm and 25 nm pore surfaces, which have a high density of vertical pores per unit surface area.

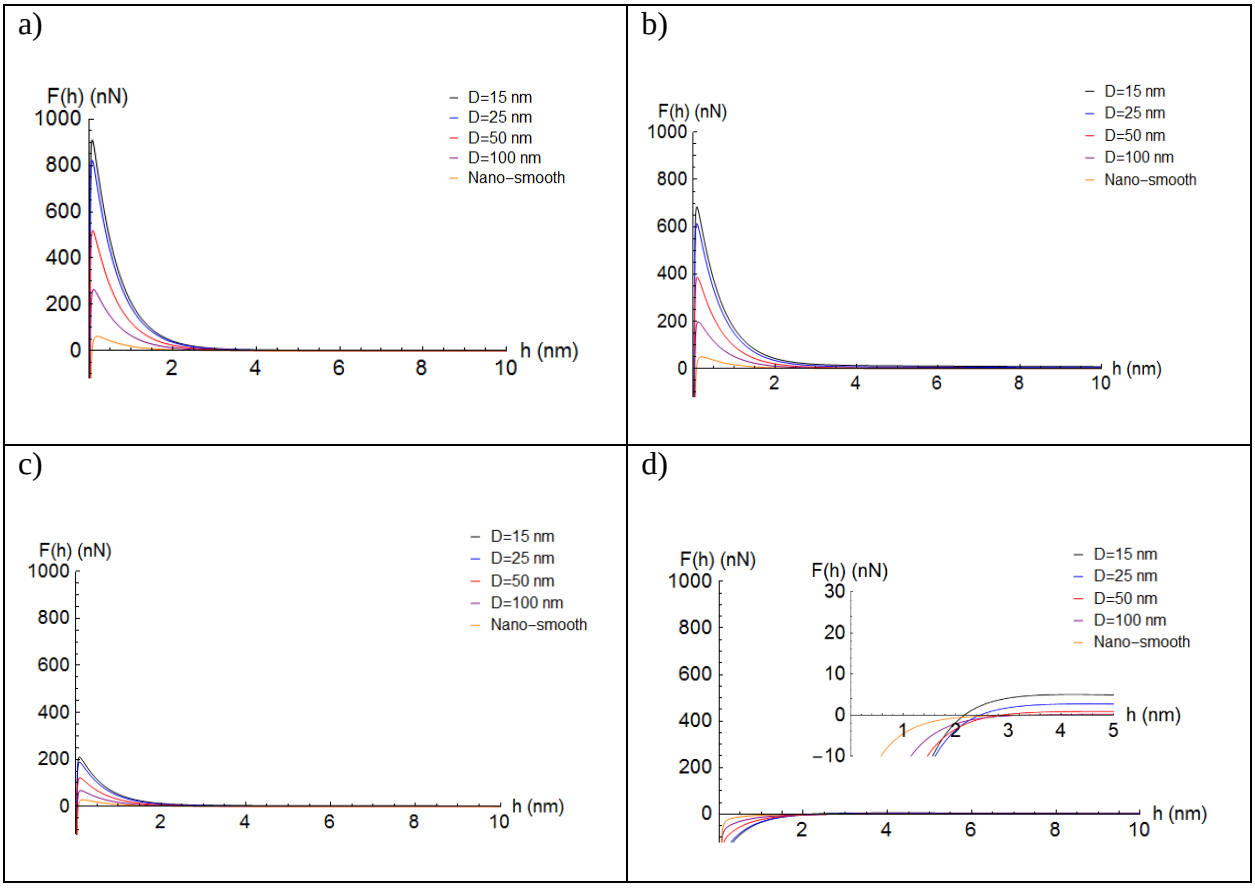

Figure 27. Example of total cell-surface interaction force as a function of distance from the surface for one **(a)** *E. coli* O157:H7 cell; **(b)** *E. coli* K12; **(c)** *S. aureus*; **(d)** *L. monocytogenes* - the inset shows a zoomed-in plot.

Table 4. Physicochemical parameters used in the XDLVO model calculations for all bacterial strains tested

Bacterial strain	Contact angles (°) in various liquids			Zeta potential (mV)	Cell size	
	WCA	DCA	GCA		Volume (μm^3)	Equivalent radius (nm)
L. innocua	46.5±1.2	65.9±2.3	46.4±1.7	-21.5±0.5	0.13	318
L. monocytogenes	56.7±0.5	50.4±1.2	70.1±0.9	-21.1±0.5	0.73	559
E. coli O157:H7	25.5±1.5	46.1±0.5	62.4±1.5	-4.8±0.4	1.65	733
E. coli K12	41.1±1.0	47.2±2.8	71.5±1.4	-29.0±0.1	1.48	707
E. coli ATCC 25922	41.4±0.5	55.6±3.4	75.7±2.0	-22.4±0.3	0.50	494
S. aureus	47.0±1.9	60.0±3.5	76.4±0.9	-23.4±0.4	0.27	399
S. epidermidis	15.8±1.4	62.1±0.5	91.3±1.1	-16.3±0.4	0.20	361

F_{max} for all bacteria - anodic surface pairs used in the study was plotted against the cell counts (**Figure 28**), calculated based on the biomass volume and the measured cell size (**Table 4**). The data points for the two non-pathogenic strains (*L. innocua* and *E. coli* ATCC 25922) from our previous work [15] were also included in this analysis. This plot allowed several important observations. First, for all strains, the greater the magnitude of the repulsive energetic barrier,

represented by F_{max}, the fewer cells accumulated on the surface. A linear correlation between F_{max} and the number of attached cells was obtained for each strain. Since only 4 data points per strain were available, and because of the variability of some data points, not all correlations were statistically significant. For the strains tested in this study, the values for the coefficient of determination were as follows: R^2= 0.743 for *S. aureus*, R^2= 0.864 for *L. monocytogenes*, R^2= 0.815 for *E. coli* K12, and R^2=0.998 for *E. coli* O157:H7. **Figure 28** also illustrates a clustering of bacteria from different species. The two *Listeria* strains (diamond symbols) showed the strongest dependence on F_{max}, which means that small increases in the repulsive force can be extremely effective in reducing the attachment by these bacteria to the anodic surfaces. The three *E. coli* strains (circle symbols), while showing a good correlation between attachment and F_{max}, were less sensitive to the magnitude of F_{max} compared to *Listeria. S. aureus* (triangle symbols) had a behavior intermediate between *Listeria* and *E. coli*. The similar response to F_{max} of bacteria from the same species is indicative of the role of biological factors in attachment, but also shows that the physicochemical approach used here is able to reflect these differences.

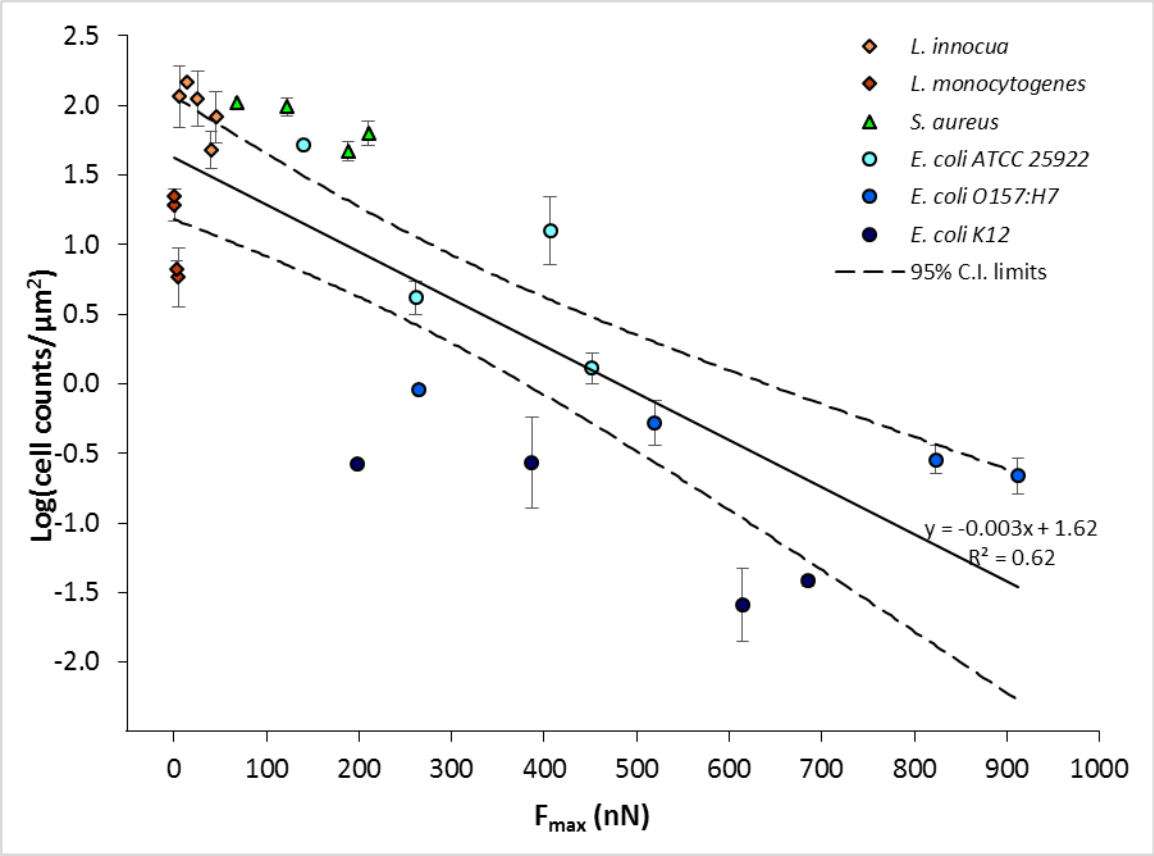

Figure 28. Bacteria cell counts in the biofilm per unit area of surface as a function of F_{max}, after 48 h of incubation

The other very important observation is that a statistically significant ($P < 0.001$) linear correlation between F_{max} and the number of attached cells from all bacterial strains was obtained. The solid line in Figure 28 represents the linear regression line and the dotted lines the 95% confidence interval (C.I.) range for the linear regression. The C.I. accounts for both the variance of the experimental data and the uncertainty in the numerical coefficients of the linear regression. The 95% C.I. lines are the closest in the middle of the F_{max} range, and further apart towards the ends of the F_{max} range, which indicates that the uncertainty of the prediction increases for both very low and very high attachment.

3.5. Discussion

Bacterial attachment to abiotic surfaces and subsequent biofilm formation are complex processes, controlled by the interplay between biological factors, such as secretion of extracellular materials by the bacteria, bacterial appendages and other cell surface structures that can contribute to bacterial sensing of the surface [10], and physicochemical factors, such as surface topography, surface charge, and surface energy [14]. Since it is practically impossible to alter the properties of naturally occurring bacteria and make them less likely to attach to abiotic surfaces, the more feasible approach to tackling biofouling is to reduce the propensity of the abiotic surfaces to bacterial attachment, by altering their surface chemistry and topography.

3.5.1. Effect of surface topography on antifouling ability

The correlation between bacteria attachment and surface topography has been investigated for a long time. Commonly used surface roughness parameters such as average and root mean square roughness describe only the height variation of the surface, but not the spatial distribution or the shape of surface features [34]. Donoso et. al. demonstrated that neither parameter is a reliable predictor for the interfacial area from which surface-based forces (i.e. F_{AB} and F_{EL}) arise, as the relationship between these parameters and the interfacial area is not monotonic [35]. These results explain at least in part why despite the volume of work in this area, the mechanisms by which surface roughness and topography modulate attachment remain largely unclear, especially at a scale smaller than the dimension of a bacterial cell [28,34].

The present study shows that attachment by *E. coli* O157:H7, *E. coli* K12, *L. monocytogenes*, *S. aureus* and *S. epidermidis* was largely impaired on anodic alumina surfaces with pore sizes of 15 nm and 25 nm in diameter, as compared to surfaces with larger pores or

nanosmooth surfaces (**Figure 23**). The visual CLSM observations were validated by quantitative assessment of the biofilm matrices (**Figure 24**).

This study also allowed us to make several very useful observations regarding the effect of abiotic surface properties on bacterial attachment. To date, many biofouling studies used surface energy values calculated from apparent contact angles as a predictor of attachment. Several studies suggest that highly hydrophobic surfaces, which have water contact angles (WCA) higher than 90°, have a lower propensity for microbial attachment and biofouling [36]. Nonetheless, the conventional hydrophobic-hydrophilic dichotomic categorization of surfaces and bacterial cells has been proved insufficient to make accurate predictions about bacterial attachment. Hook et. al. found no correlation between bacterial attachment and WCA for 496 polymeric materials. Rather, they suggested that surface chemical groups dictated the propensity of bacterial attachment onto polymer surfaces rather than WCA alone [37]. Our results also show that neither hydrophobicity nor chemistry alone cannot be used as a predictor for attachment. Despite the fact that all porous surfaces used in our study were chemically identical, the measured contact angles of three probe liquids varied notably among surfaces (**Figure 29**).

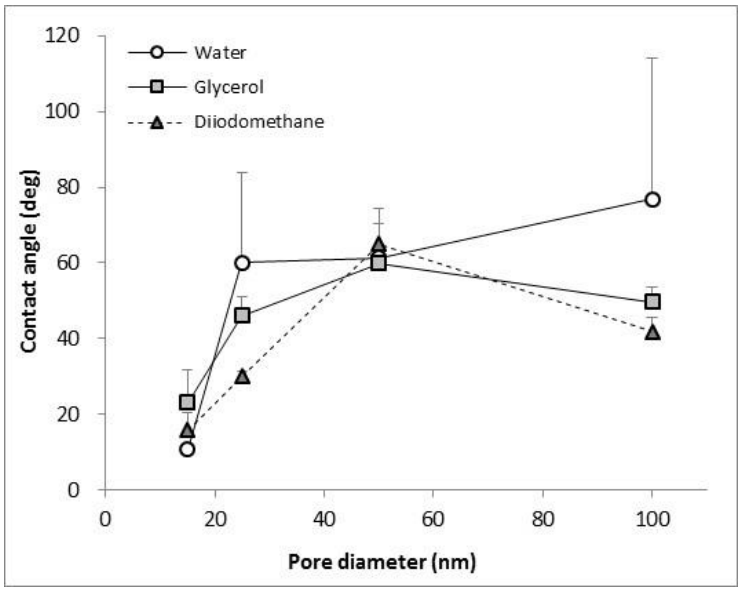

Figure 29. Measured contact angles in water, glycerol, and diiodomethane for anodic alumina surfaces, as a function of pore diameter

Furthermore, the surfaces that were most effective against bacterial attachment had the smallest contact angles in all three liquids and a clear hydrophilic behavior, while surfaces with the largest pores were more hydrophobic, yet allowed higher attachment by bacteria. To understand the change in contact angle with pore size, it is important to consider the fundamental factors that dictate the apparent contact angles, namely the intrinsic (Young's) contact angle of a liquid droplet on an ideal (rigid, flat, chemically homogeneous, insoluble, nonreactive) solid surface, and surface topography, which can enhance both hydrophobic and hydrophilic reactions [38,39]. The trends in Figure 29 agree with the Wenzel relation, which dictates that surface topography on hydrophilic surfaces (WCA < 90°) enhances their apparent hydrophilicity [39]. For alumina surfaces under consideration here this was likely due to the capillary effects caused by the cylindrical pores [40].

A quantitative prediction of the propensity of bacteria to attach to surfaces is not straightforward. In this work, such a prediction was obtained by using the comprehensive XDLVO model, which considers the role of cell-surface physicochemical interaction forces in attachment.

This model has been used before, with varing degrees of success, in describing the interaction between colloidal particles and patterned surfaces [41,42], or the interaction between microbial cells and surfaces [43–45]. One element lacking in previous applications of this model is that contributions from surface elements perpendicular to the surface were not considered. Taking this into account allowed us to explain the extraordinary bacteria-repelling effect of the 15 nm and 25 nm alumina surfaces. Specifically, this effect is attributed to the vertical sidewalls of the densely distributed cylindrical pores, which exerted additional electrostatic repulsion and acid-base repulsive forces on the bacterial cells found in the proximity of the surfaces.

The fact that the correlation between cell-surface interaction force, represented by F_{max}, and attachment holds across several bacteria strains (**Figure 28**) is of considerable importance in that, despite the different cell wall structure, shape, presence or absence of cellular appendages, the adjusted XDLVO model is capable of predicting the trends in bacteria attachment with reasonable accuracy. This is also very relevant from a practical perspective. While this study has been conducted on individual strains, in both natural and man-made environments bacteria are present in multi-microbial communities. The overall correlation between $F_{\max}$ and attachment found here indicates that an increase in the repulsive force will be able to reduce attachment by multiple bacteria, albeit to different degrees.

As an example of how this model can be used as a design tool, we generated predictions of changes in cell-surface interaction forces induced by changes in the elements of surface topography. Our calculations show that pore diameter has a tremendous effect on the repulsive forces, with $F_{\max}$ increasing exponentially as pore diameter decreases. Increasing surface porosity at a fixed pore diameter results in a proportional increase in $F_{\max}$, while pore depth does not seem to have a significant effect beyond several tens of nanometers (**Figure 10**). Figure 30 illustrates

how changing pore diameter and surface porosity affects F_{max} for all bacteria strains used in this study, except *S. epidermidis*. What is remarkable is that the effect of surface topography is similar for all microorganisms, even if the magnitude of F_{max} varies among the different strains. This is extremely meaningful from a practical perspective because it indicates that further decreasing pore size and increasing the surface porosity will improve the anti-attachment ability of anodic surfaces.

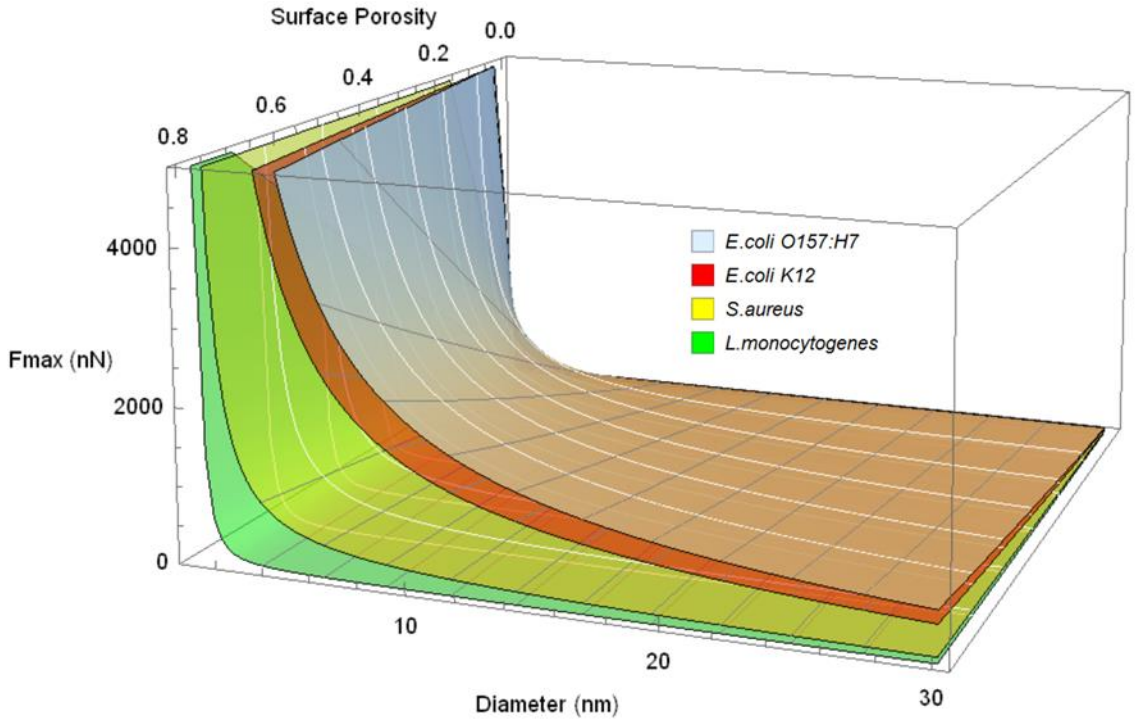

Figure 30. Predicted values of the maximum repelling cell-surface interaction force as a function of pore diameter and surface porosity of the alumina anodic surfaces for *E. coli* O157:H7, *E. coli* K12, *S. aureus* and *L. monocytogenes*

3.5.2. Effect of surface energy on antifouling ability

The intrinsic surface energy of material is extremely important for its antifouling properties because it determines the direction and magnitude of the interaction forces exerted on potentially fouling species (i.e. molecules, colloidal particles, microorganisms). In a sense, surface nanoscale topography serves as a "multiplier" of the intrinsic antifouling ability determined by the intrinsic

surface energy of the material. An excellent antifouling material surface could be obtained by achieving an intrinsic surface energy conducive to large repulsive forces and large surface area expansion resulting from surface nanoscale topography. Therefore, a predictive tool that enables fast screening for intrinsically effective antifouling surfaces would be of great value for selecting or designing antifouling materials for various applications.

To achieve this, a "F_{max} Cloud" was developed here based on the XDLVO theory. For any given bacterial strain, a F_{max} Cloud can be generated based on the three-liquid contact angles of this particular strain, as the one shown in Figure 31 for *E. coli* ATCC 25922. In this three-dimensional space, the red regions indicate where effective antifouling surface against this strain could occur; the orange sphere represents an ideal AAO surface.

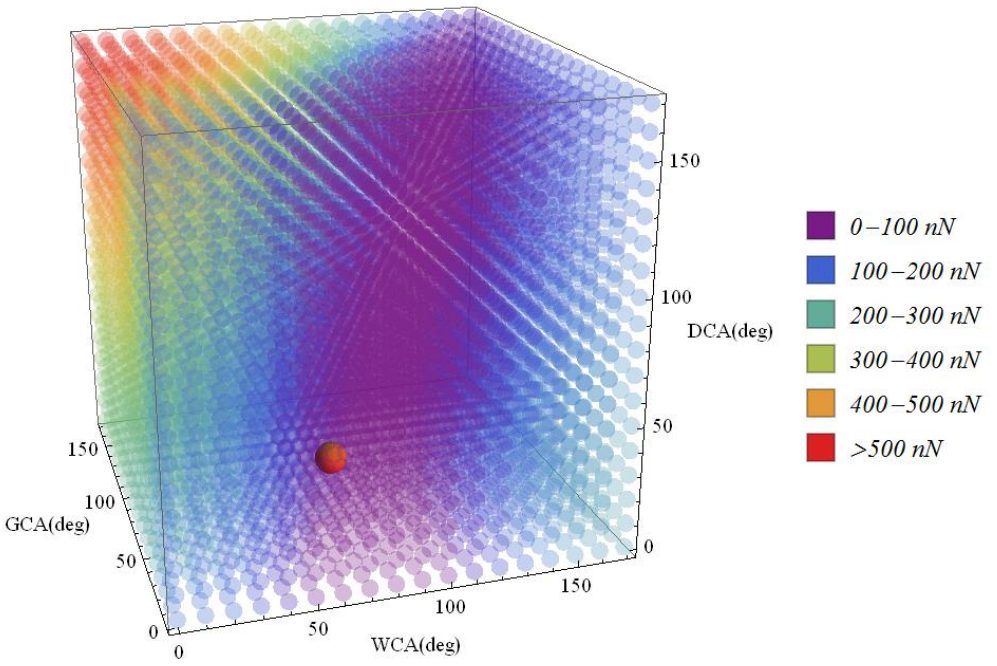

Figure 31. F_{max} Cloud for *E. coli* ATCC 25922 in a contact angle space defined by contact angles of water, glycerol, and diiodomethane on solid substrate surfaces. The orange sphere represents an ideal aluminum oxide surface.

Such an F_{max} Cloud could be built using: (1) a contact angle perspective (Figure 31), which uses the contact angle values of three probe liquids on substrate material as the x, y, and z-axis; and (2) a surface energy perspective (**Error! Reference source not found.**b), which uses the three surface energy components – γ^-, γ^+, and γ^{LW} – as the axes.

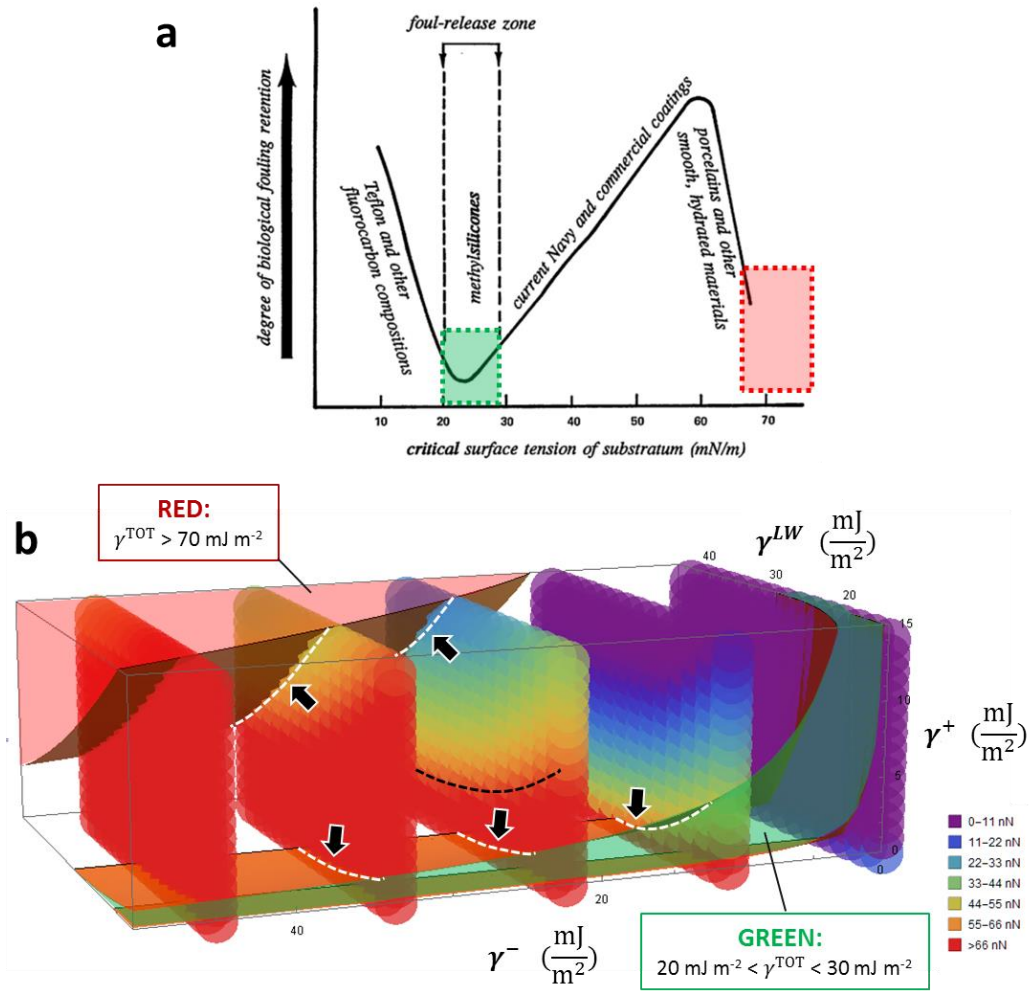

Figure 32. The Baier Curve explained by the "F_{max} Cloud". **(a)** The Baier curve[46] with the "antifouling" or "foul-release" range of the critical surface tension of substratum highlighted in dashed boxes; the green box and the red box denote typical ranges for low-surface-energy and high-surface-energy antifouling materials, respectively; **(b)** the antifouling regions indicated by the Baier Curve juxtaposed on a sectionalized "F_{max} Cloud" in a three-dimensional surface energy space. The space delimited by the "Baier surfaces" is represented in green and red with respect to the antifouling regions highlighted in (a). The "F_{max} Cloud" is color-coded to reflect the magnitude of F_{max} exerted on an *E. coli* ATCC 25922 cell approaching a material surface. The location of a specific material in the "F_{max} Cloud" is determined by the values of its surface

energy components. The black arrows point to examples of the intersection curve segments, which are signified by the dashed white curves; a F_{max} contour curve is signified by a dashed black curve.

Each of these perspectives has its own advantage: the contact angle perspective presents a clear relationship between F_{max} and water contact angles; contact angles can be easily obtained using a goniometer, and the generated F_{max} Cloud is relatively easy to understand. The downside of the contact angle perspective, however, is that such F_{max} Cloud is useful only if the contact angles of the substrate materials of interest happen to be measured with exactly the same set of probe liquids, which limits breath of application for. The surface energy perspective, on the other hand, provides a framework that is useful irrespective of the probe liquids and therefore has broader applicability than the contact angle perspective. For instance, a material whose contact angles are measured with water, glycerol, and formamide cannot be represented in a contact angle F_{max} Cloud based on water, glycerol, and diiodomethane contact angles (Figure 31); after the liquid contact angle values are converted to surface energies though, the material *can* be located in a surface energy F_{max} Cloud (Figure 32b). The full significance of Figure 32 will be explained in detail later.

Once a F_{max} Cloud is generated for a fouling species, a search can be carried out in a material database to find those materials whose surface energy satisfy the "high repulsion zone" indicated by the F_{max} Cloud. These materials in their original form should be first be validated for effectiveness by experimental fouling assays, and the materials that exhibit good intrinsic antifouling characteristics can be then subjected to surface nano-structuring by techniques such as anodization or nanoimprinting This step will dramatically increase the surface area of the material, which should further enhance the repulsive forces and thereby improve the antifouling

effectiveness of the material. This represents a physicochemical roadmap towards achieving highly effective antifouling materials and surfaces.

The F_{max} Cloud concept was also used to understand the validity of the Baier curve, which has already been presented in Section 1.2 of Chapter One. First, the Baier curve was expanded to a three-dimensional surface energy space by expressing the critical surface tension of a substratum (γ^{TOT}) in terms of its apolar surface energy component (γ^{LW}), and its two polar surface components: the electron-donor component (γ^-) and the electron-acceptor component (γ^+):

$$\gamma^{TOT} = \gamma^{LW} + 2\sqrt{\gamma^+ \gamma^-} \quad (25)$$

According to the Baier curve, there two low-fouling/foul-release regions:

$$20 < \gamma^{TOT} < 30 \text{ or } \gamma^{TOT} > 70 \qquad \text{Unit: mJ m}^{-2} \quad (26)$$

Substitute the right-hand side of eq. (25) for the "γ^{TOT}" in eq. (26), we get:

$20 < \gamma^{LW} + 2\sqrt{\gamma^+ \gamma^-} < 30$ (the green region) or $\gamma^{LW} + 2\sqrt{\gamma^+ \gamma^-} > 70$ (the red region)

After the expansion of the surface energy dimension of the Baier curve in Figure 32a from one to three, the originally one-dimensional curve segments enclosed in the green and red dashed box become the three-dimensional low-fouling space delimited by the surfaces defined by $\gamma^{LW} + 2\sqrt{\gamma^+ \gamma^-}$ of 20, 30 and 70 (mJ m^{-2}), respectively.

Next, we can juxtapose the 3D "Baier space" against the F_{max} Cloud (Figure 32b). It is an amazing coincidence that both the green and red 3D Baier space are located in the relatively high F_{max} region of the cloud. More interestingly, the intersection curve segments denoted by the white dashed lines (Figure 32b), which are resulted by the intersection between the "Baier surfaces" and the vertical cross-sections of the F_{max} cloud, possess striking similarity to the contour curves of F_{max}. An example of such contour curves is denoted by the dashed black curve in Figure 32b.

In addition to the information provided by the Baier curve, the F_{max} Cloud predicts that effective antifouling surface against *E. coli* ATCC 25922 should possess the following properties: a large electron donor component (γ^-) and a small electron-acceptor component (γ^+), characteristic to the so-called monopolar surfaces[33]. A small γ^{LW} also favors large F_{max} in this case. Despite the wide range of possible materials predicted by the F_{max} Cloud for antifouling purposes, it should be noted that materials that fulfill such surface energy combinations may not exist, or may not be suitable for certain applications. For instance, most hydrophilic monopolar polymers have an apolar surface tension component $\gamma^{LW} \approx 40$ mJ m^{-2},[47] which restricts the freedom along the γ^{LW} axis.

3.6. Conclusions

The findings of this study demonstrate a science-based, yet relatively simple and practical way to prevent attachment and subsequent biofilm formation by diverse pathogenic, as well as non-pathogenic bacteria.

REFERENCES

(1) Flemming, H.-C.; Wingender, J. The Biofilm Matrix. *Nat. Rev. Microbiol.* **2010**, *8* (9), 623–633.

(2) Costerton, J. W.; Stewart, P. S.; Greenberg, E. P. Bacterial Biofilms: A Common Cause of Persistent Infections. *Science (80-.).* **1999**, *284* (5418), 1318–1322.

(3) Smith, K.; Hunter, I. S. Efficacy of Common Hospital Biocides with Biofilms of Multi-Drug Resistant Clinical Isolates. *J. Med. Microbiol.* **2008**, *57* (8), 966–973.

(4) Stewart, P. S.; William Costerton, J. Antibiotic Resistance of Bacteria in Biofilms. *Lancet* **2001**, *358* (9276), 135–138.

(5) Harro, J. M.; Peters, B. M.; O'May, G. A.; Archer, N.; Kerns, P.; Prabhakara, R.; Shirtliff, M. E. Vaccine Development in Staphylococcus Aureus: Taking the Biofilm Phenotype into Consideration. *FEMS Immunol. Med. Microbiol.* **2010**, *59* (3), 306–323.

(6) Scharff, R. L. Economic Burden from Health Losses due to Foodborne Illness in the United States. *J. Food. Prot.* **2012**, *75* (1), 123–131.

(7) Kolodkin-Gal, I.; Romero, D.; Cao, S.; Clardy, J.; Kolter, R.; Losick, R. D-Amino Acids Trigger Biofilm Disassembly. *Science (80-.).* **2010**, *328* (April), 627–629.

(8) Feng, G.; Klein, M. I.; Gregoire, S.; Singh, A. P.; Vorsa, N.; Koo, H. The Specific Degree-of-Polymerization of A-Type Proanthocyanidin Oligomers Impacts Streptococcus Mutans Glucan-Mediated Adhesion and Transcriptome Responses within Biofilms. *Biofouling* **2013**, *29* (6), 629–640.

(9) Bridier, A.; Briandet, R.; Thomas, V.; Dubois-Brissonnet, F. Resistance of Bacterial Biofilms to Disinfectants : A Review. *Biofouling* **2011**, *26* (9), 1017–1032.

(10) Hori, K.; Matsumoto, S. Bacterial Adhesion: From Mechanism to Control. *Biochem. Eng. J.* **2010**, *48* (3), 424–434.

(11) Whitehead, K. a; Colligon, J.; Verran, J. Retention of Microbial Cells in Substratum Surface Features of Micrometer and Sub-Micrometer Dimensions. *Colloids Surf. B Biointerfaces* **2005**, *41* (2–3), 129–138.

(12) Hsu, L.; Fang, J.; Borca-Tasciuc, D.; Worobo, R.; Moraru, C. I. The Effect of Micro- and Nanoscale Topography on the Adhesion of Bacterial Cells to Solid Surfaces. *Appl. Environ. Microbiol.* **2013**.

(13) Friedlander, R. S.; Vlamakis, H.; Kim, P.; Khan, M.; Kolter, R.; Aizenberg, J. Bacterial Flagella Explore Microscale Hummocks and Hollows to Increase Adhesion. *Proc. Natl. Acad. Sci. U. S. A.* **2013**, *110* (14), 1–6.

(14) Anselme, K.; Davidson, P.; Popa, A. M.; Giazzon, M.; Liley, M.; Ploux, L. The Interaction of Cells and Bacteria with Surfaces Structured at the Nanometre Scale. *Acta Biomater.* **2010**, *6* (10), 3824–3846.

(15) Feng, G.; Cheng, Y.; Wang, S.; Hsu, L. C.; Feliz, Y.; Borca-Tasciuc, D. a.; Worobo, R. W.; Moraru, C. I. Alumina Surfaces with Nanoscale Topography Reduce Attachment and Biofilm Formation by Escherichia Coli and Listeria Spp. *Biofouling* **2014**, *30* (November), 1253–1268.

(16) Mead, P. S.; Slutsker, L.; Dietz, V.; McCaig, L. F.; Bresee, J. S.; Shapiro, C.; Griffin, P. M.; Tauxe, R.

V. Food-Related Illness and Death in the United States. *Emerg. Infect. Dis.* **1999**, *5* (5), 607–625.

(17) Giovannacci, I.; Ragimbeau, C.; Queguiner, S.; Salvat, G.; Vendeuvre, J. L.; Carlier, V.; Ermel, G. Listeria Monocytogenes in Pork Slaughtering and Cutting Plants Use of RAPD, PFGE and PCR-REA for Tracing and Molecular Epidemiology. *Int. J. Food Microbiol.* **1999**, *53* (2–3), 127–140.

(18) Miettinen, M. K.; Björkroth, K. J.; Korkeala, H. J. Characterization of Listeria Monocytogenes from an Ice Cream Plant by Serotyping and Pulsed-Field Gel Electrophoresis. *Int. J. Food Microbiol.* **1999**, *46* (3), 187–192.

(19) Vogel, B. F.; Huss, H. H.; Ojeniyi, B.; Ahrens, P.; Gram, L. Elucidation of Listeria Monocytogenes Contamination Routes in Cold-Smoked Salmon Processing Plants Detected by DNA-Based Typing Methods. *Appl. Environ. Microbiol.* **2001**, *67* (6), 2586–2595.

(20) Beuchat, L. R. Ecological Factors Influencing Survival and Growth of Human Pathogens on Raw Fruits and Vegetables. *Microbes Infect.* **2002**, *4* (4), 413–423.

(21) Karch, H.; Tarr, P. I.; Bielaszewska, M. Enterohaemorrhagic Escherichia Coli in Human Medicine. *Int. J. Med. Microbiol.* **2005**, *295* (6–7), 405–418.

(22) Lowy, F. D. Staphylococcus Aureus Infections. *N. Engl. J. Med.* **1998**, *339* (8), 520–532.

(23) Giacometti, A.; Cirioni, O.; Schimizzi, A. M.; Del Prete, M. S.; Barchiesi, F.; D'Errico, M. M.; Petrelli, E.; Scalise, G. Epidemiology and Microbiology of Surgical Wound Infections. *J. Clin. Microbiol.* **2000**, *38* (2), 918–922.

(24) Huebner, J.; Goldmann, D. A. Coagulase-Negative Staphylococci: Role as Pathogens. *Ann. Rev. Med.* **1999**, *50*, 223–236.

(25) Jessensky, O.; Müller, F.; Gösele, U. Self-Organized Formation of Hexagonal Pore Arrays in Anodic Alumina. *Appl. Phys. Lett.* **1998**, *72* (10), 1173.

(26) Masuda, H.; Yada, K.; Osaka, A. Self-Ordering of Cell Configuration of Anodic Porous Alumina with Large-Size Pores in Phosphoric Acid Solution. *Jpn. J. Appl. Phys.* **1998**, *37* (11A), L1340–L1342.

(27) Heydorn, A.; Nielsen, a T.; Hentzer, M.; Sternberg, C.; Givskov, M.; Ersbøll, B. K.; Molin, S. Quantification of Biofilm Structures by the Novel Computer Program COMSTAT. *Microbiology* **2000**, *146*, 2395–2407.

(28) Li, B.; Logan, B. E. Bacterial Adhesion to Glass and Metal-Oxide Surfaces. *Colloid Surf. B* **2004**, *36* (2), 81–90.

(29) Evans, E.; Brown, M. R. W.; Gilbert, P. Iron Chelator, Exopolysaccharide and Protease Production in Staphylococcus Epidermidis: A Comparative Study of the Effects of Specific Growth Rate in Biofilm and Planktonic Culture. *Microbiology* **1994**, *140* (1), 153–157.

(30) Heilmann, C.; Schweitzer, O.; Gerke, C.; Vanittanakom, N.; Mack, D.; Götz, F. Molecular Basis of Intercellular Adhesion in the Biofilm-Forming Staphylococcus Epidermidis. *Mol. Microbiol.* **1996**, *20* (5), 1083–1091.

(31) Mack, D.; Fischer, W.; Krokotsch, A.; Leopold, K.; Hartmann, R.; Egge, H.; Laufs, R. The Intercellular Adhesin Involved in Biofilm Accumulation of Staphylococcus Epidermidis Is a Linear β-1,6-Linked Glucosaminoglycan: Purification and Structural Analysis. *J. Bacteriol.* **1996**, *178* (1), 175–183.

(32) Ran, C.; Ding, G.; Liu, W.; Deng, Y.; Hou, W. Wetting on Nanoporous Alumina Surface: Transition between Wenzel and Cassie States Controlled by Surface Structure. *Langmuir Acs J. Surfaces Colloids* **2008**, *24* (18), 9952–9955.

(33) van Oss, C. J. Acid—base Interfacial Interactions in Aqueous Media. *Colloids Surfaces A Physicochem. Eng. Asp.* **1993**, *78*, 1–49.

(34) Crawford, R. J.; Webb, H. K.; Truong, V. K.; Hasan, J.; Ivanova, E. P. Surface Topographical Factors Influencing Bacterial Attachment. *Adv. Colloid Interfac.* **2012**, *179–182*, 142–149.

(35) Donoso, M. G.; Méndez-Vilas, A.; Bruque, J. M.; González-Martin, M. L. On the Relationship between Common Amplitude Surface Roughness Parameters and Surface Area: Implications for the Study of Cell–material Interactions. *Int. Biodeter. Biodegr.* **2007**, *59* (3), 245–251.

(36) Mérian, T.; Goddard, J. M. Advances in Nonfouling Materials: Perspectives for the Food Industry. *J. Agric. Food Chem.* **2012**, *60* (12), 2943–2957.

(37) Hook, A. L.; Chang, C.; Yang, J.; Luckett, J.; Cockayne, A.; Atkinson, S.; Mei, Y.; Bayston, R.; Irvine, D. J.; Langer, R.; et al. Combinatorial Discovery of Polymers Resistant to Bacterial Attachment. *Nat. Biotechnol.* **2012**, *30* (9), 868–875.

(38) Gao, L.; McCarthy, T. J. How Wenzel and Cassie Were Wrong. *Langmuir* **2007**, *23* (7), 3762–3765.

(39) Wenzel, R. Resistance of Solid Surfaces. *J. Ind. Eng. Chem.* **1936**, *28* (8), 988–994.

(40) Ran, C.; Ding, G.; Liu, W.; Deng, Y.; Hou, W. Wetting on Nanoporous Alumina Surface: Transition between Wenzel and Cassie States Controlled by Surface Structure. *Langmuir* **2008**, *24* (18), 9952–9955.

(41) Hoek, E. M. V; Bhattacharjee, S.; Elimelech, M. Effect of Membrane Surface Roughness on Colloid - Membrane DLVO Interactions. *Langmuir* **2003**, *19* (16), 4836–4847.

(42) Martines, E.; Csaderova, L.; Morgan, H.; Curtis, A. S. G.; Riehle, M. O. DLVO Interaction Energy between a Sphere and a Nano-Patterned Plate. *Colloid Surf. A* **2007**, *318* (1–3), 45–52.

(43) Chen, Y.; Harapanahalli, A. K.; Busscher, H. J.; Norde, W.; van der Mei, H. C. Nanoscale Cell Wall Deformation Impacts Long-Range Bacterial Adhesion Forces on Surfaces. *Appl. Environ. Microbiol.* **2014**, *80* (2), 637–643.

(44) Chrysikopoulos, C. V.; Syngouna, V. I. Attachment of Bacteriophages MS2 and ΦX174 onto Kaolinite and Montmorillonite: Extended-DLVO Interactions. *Colloids Surfaces B Biointerfaces* **2012**, *92*, 74–83.

(45) Chia, T. W. R.; Nguyen, V. T.; McMeekin, T.; Fegan, N.; Dykes, G. A. Stochasticity of Bacterial Attachment and Its Predictability by the Extended Derjaguin-Landau-Verwey-Overbeek Theory. *Appl. Environ. Microbiol.* **2011**, *77* (11), 3757–3764.

(46) Baier, R. E. Surface Behaviour of Biomaterials: The Theta Surface for Biocompatibility. *J. Mater. Sci. Mater. Med.* **2006**, *17* (11), 1057–1062.

(47) Oss, C. J. Van; Chaudhury, M. K.; Good, R. J. Monopolar Surfaces. *Adv. Colloid Interface Sci.* **1987**, *28*, 35–64.

CHAPTER FOUR

EVIDENCE FOR THE LONG RANGE BACTERIA-EXCLUSION ZONE NEAR HYDROPHILIC SURFACES [3]

4.1. Abstract

Hydrophilic surfaces of both an abiotic and biological origin have been found to bear particle-exclusion zones (EZ) as large as hundreds of micrometers above fluid-solid interfaces. While the mechanism for EZ formation is still debated, its unique long-range particle-repellent property may hold promise for the development of antifouling surfaces. Here we present the first evidence for the existence of bacteria-free exclusion zones against three bacterial pathogens associated with both hospital infections and foodborne outbreaks: *Staphylococcus aureus*, *Escherichia coli* O157:H7, and *Listeria monocytogenes*. Using confocal laser scanning microscopy (CLSM), we visualized and quantified bacterial cell density distribution in the vicinity of a Nafion-liquid interface. A robust image analysis method was developed to generate a quantitative profile of cell concentration near the interface, which allowed the precise quantification of EZ and a transition zone (TZ), based on pixel intensity profiles. Tests were carried out both in a simple buffer, as well as a complex nutritive broth of high ionic strength (IS). Our results revealed a typical bacterial EZ size of 40 - 60 μm and a TZ of 40 - 80 μm for bacteria suspended in tryptic soy broth (TSB, pH 7.0, IS ≈ 100 mM). There were no statistical differences in the size of EZ and TZ for the three strains, implying a physicochemical underpinning for the existence of EZ and suggesting a potentially broad-spectrum efficacy. These findings may have

[3] The main content of this chapter (except section 4.4.4 and 4.4.5) is included in the manuscript: Evidence of a bacterial exclusion zone at the liquid-solid interface of hydrophilic Nafion. Authors: Yifan Cheng and Carmen I. Moraru.

important implications in developing biofouling-resistant material surfaces for a wide range of applications sensitive to bacterial attachment and biofilm formation.

4.2. Introduction

The existence of a long-range, particle-free zone, so-called an exclusion zone (EZ), near certain types of surfaces has been acknowledged by several authors in the past decade.[1–5] EZs have been found in the vicinity of both abiotic surfaces, such as hydrophilic polymers and hydrogels[6,7] and metals[8], as well as biological surfaces, including muscle tissues[1], white blood cells[9], vascular endothelium and xylem[10], and rabbit cornea[11]. Such EZs have been observed when solid surfaces were exposed to a wide range of particle species including microspheres[12], carbon particles, colloidal gold, quantum dots, and dyes[13], of size varying from colloidal particles with diameters of tens of micrometers down to solutes of molecular weight less than 100 Da[1,12]. The reported size of EZ typically ranges from several tens of micrometers up to several hundreds of micrometers depending on the properties of the medium, the material surface, and the suspended particles.[6,12] EZs have many interesting properties[10], the most notable being the remarkably long particle-repelling range, on a typical scale of hundreds of micrometers, which far exceeds that of the Debye length, typically on the order of several nanometers to tenths of nanometers. While the underlying mechanisms for this long-range solute-exclusion zone are not presently clear and sometimes highly debated [3,4,12,14], this phenomenon has already shown promise in a wide range of applications including microfluidics[15] or water purification[16].

While most reports on EZ involve non-biologic particles, Klyuzhin et al. made a brief observation that, when suspended in deionized water, some bacterial cells (*Escherichia coli* and *Nitrousomonus europea*) were excluded from the vicinity of hydrophilic Nafion surfaces.[16] However, neither confirmation of this observation nor a systematic investigation of the existence

of EZ for bacteria have been published. The existence of bacteria EZs near abiotic surfaces could have tremendous significance for the development of materials that minimize colonization by bacteria, which can help the fight against biofouling and bacterial infections in many areas related to human life such as medicine, food or water processing. The attachment of planktonic bacterial cells to surfaces is the first step in the initiation of the biofilm formation cycle[17], which is largely influenced by the interplay between physicochemical and biological factors[19]. Since mature biofilms are very difficult to eradicate, the initial attachment has become the target of an array of novel antifouling approaches, many based on modifying the properties of material surfaces to render antifouling effect. In this context, developing surfaces that show a bacterial EZ may become a promising approach for reducing attachment by bacteria.

To this end, this study investigates the existence of EZ in the vicinity of Nafion for several bacterial strains. Three pathogenic bacterial strains commonly implicated in biomedical, dental or food processing environments were selected as challenge organisms: *Staphylococcus aureus*, *Escherichia coli* O157:H7, and *Listeria monocytogenes*. Additionally, the non-pathogenic *Escherichia coli* ATCC 25922 and *Listeria innocua*, which are commonly used as surrogates for *Escherichia coli* O157:H7 and *Listeria monocytogenes*, were also investigated. These strains provide a good representation for both Gram-positive and Gram-negative cell wall structures, cell morphology (rods and cocci), and surface properties (surface energy, zeta potential, different expression of bacterial appendages), all of which have been shown to greatly influence the attachment of bacterial cells to biotic and abiotic substrates.[18-21] Since the size of EZ is thought to be largely dependent on the pH and ionic strength of the suspension medium[20], it is imperative to evaluate EZ under conditions relevant to possible applications. Therefore, the existence of bacteria EZ in the vicinity of a hydrophilic surface (Nafion) was evaluated in liquids of ionic strength (IS)

that are typical for aqueous environments encountered in biomedical applications and food processing (10 mM and 100 mM, respectively).

4.3. Materials and Methods

4.3.1. Bacteria suspension preparation

Cultures of *E. coli* ATCC 25922, *E. coli* O157:H7 ATCC 43894, *L. innocua*, *L. monocytogenes* 10403S, *S. aureus* 9144 were maintained in tryptic soy broth (TSB) with 20% (volume/volume) glycerol at -80 °C. To activate the cultures, they were streak-plated on tryptic soy agar (TSA), followed by incubation at 37 °C for 24 h. To prepare bacteria suspensions for the EZ experiments, colonies from TSA were subcultured in 3 mL TSB for 16 h at 37 °C. The planktonic bacterial cells were then labeled with propidium iodide and SYTO 9 (Molecular Probes Inc., Eugene, OR, USA) by adding 5 µL of each dye to 3 mL bacteria suspension, followed by incubation in the dark for 10 min at 20 °C. After that the bacterial suspensions were diluted 1:10 (v/v) with Butterfield's Phosphate Buffer (BPB) (pH 7.1, IS ≈ 10 mM) or fresh TSB (pH 7.0, IS ≈ 100 mM), respectively, to reach a final cell concentration about 10^7 cells/mL.

4.3.2. Nafion surface preparation

Nafion, a polymer consisting of a tetrafluoroethylene backbone with sulfonic acid-capped side chains, was selected as the model surface for this work, due to its prominent and well-characterized EZ[6]. Nafion 1110 (254 µm-thick film, Dupont, Wilmington, DL, USA) was cut into 1 cm × 1 cm squares and mounted onto a plastic microscope cover slide via two-sided tape. The mounted surfaces were then immersed in Milli-Q water (18.2 mΩ, UV treated, Millipore Corporation, Billerica, MA, USA) for at least 20 min, to allow them to equilibrate to fully-hydrated state [21]. The edges were trimmed straight with a sharp blade. Next, the Nafion coupons were

subjected to sonication in a bath sonicator for 1 h to remove surface contaminants. The cleaned coupons were then kept submerged in Milli-Q water until CLSM visualization.

4.3.3. Visualization of EZs by confocal laser scanning microscopy

Each Nafion coupon prepared as above was placed vertically in a plastic Petri dish with a confocal-compatible glass bottom, which was placed horizontally over the objective lens of a confocal microscope. After that, 3 mL aliquot of the fluorescently labeled bacteria suspension prepared as above was pipetted onto the glass bottom, ensuring that the bottom half of the Nafion coupon was fully immersed in liquid (Figure 33a), followed by 10 min equilibration. To verify if the experimental conditions did cause bacterial lethality, *E. coli* ATCC 25922 cells were labeled with Live/Dead BacLight SYTO 9 and propidium iodide (PI) and suspended in BPB. The labeled bacterial cells fluoresced either green (if alive) or red (if dead) upon examination by confocal laser scanning microscopy.

Three-dimensional images of the Nafion-bacteria suspension interfaces were acquired using a Zeiss 710 confocal laser scanning microscope (CLSM) equipped with inverted immersion objectives (Carl Zeiss, Jena, Germany). Specifically, a Plan-Apochromat 5 × water immersion objective lens at a scanning speed of 11 and frame pixels of 512 × 512 (surface area of 400 × 400 μm^2) was used. The exciting laser wavelength was 488 nm, and the laser power and pinhole were set to 800 and 9, respectively. The Nafion-bacteria suspension interface was scanned plane-by-plane in Z-Stack mode, with a step size of 3.66 µm. The image stack was later reconstructed to render 3D images that contain quantifiable information about cell distribution at the interface (Figure 33d). In order to avoid the artifacts near the cutting edge of Nafion surfaces and thus its influence on EZ formation, the image slices constituting the 3D CLSM image in Figure 33d were

taken in a region (starting at about 100 μm – 150 μm apart from the glass bottom) where there was no noticeable change in EZ size as the focal plane moved away from the bottom edge of Nafion.

In the experiments with pathogenic strains, several changes of this protocol were made: 1) TSB was used as the liquid medium to better mimic the environmental conditions associated with food processing or biomedical applications (high nutrient availability, high IS); 2) bacterial cells were stained only with the SYTO 9 green fluorescent dye. This was done because red fluorescence emitted by propidium iodide was not detectable at the interface, indicating limited bacterial membrane damage under the experimental conditions used here. Therefore, only green fluorescence was considered for the remainder of the study.

For each strain, at least five Nafion surface replicates were used.

4.3.4. Quantification of EZs using ImageJ

In order to obtain a quantitative characterization of the EZ, the "Profile Plots" plugin of ImageJ[22] was used to extract from the 3D CLSM images the pixel intensity, at incremental separation distances from the Nafion surface, with a step size of about 0.5 μm. The pixel intensity at each separation distance was calculated by averaging the intensity values along a line parallel to the interface. To minimize the impact of experimental variables – such as the binding affinity of SYTO 9 molecules or the initial concentration of the bacterial cells – on EZ quantification, normalized pixel intensity (NPI) profiles were determined. Dimensionless NPI values were calculated by normalizing each pixel intensity relative to the bulk intensity value of the respective bacterial suspension. The bulk intensity value was defined as the average of the pixel intensity values beyond a distance of 200 μm (sampled at a 0.5 μm increment, amounting to ~100 data points), where no difference in intensity with distance from the interface could be distinguished.

NPI profiles for all bacterial strains were generated in order to provide an objective and quantitatively accurate depiction of bacterial cell concentration in the vicinity of the solid-liquid interface.

Since the transition from EZ to the bulk suspension was not a sharply-defined transition, we propose the term "transition zone", or TZ, for describing the region between EZ and the bulk suspension. We arbitrarily defined the cutoff for exclusion zones (EZ) and transition zones (TZ) as the separation distance at which its corresponding NPI *first* reaches 20% (0.20) and 80% (0.80) of the plateau value, respectively.

4.3.5. Statistical analysis

One-tailed Z-test was conducted to determine whether the EZ and TZ thickness was significantly greater than zero at a confidence interval of 99%. One-way analysis of variance and subsequent Tukey's test were conducted using JMP Pro 12 (SAS Institute, Cary, NJ, USA) to infer whether differences in the EZ or TZ thickness across the pathogenic strains were statistically significant, at a confidence interval of 95%.

4.4. Results and Discussions

4.4.1. Evidence for long-range exclusion zones near Nafion surfaces in phosphate buffer

As proof of concept, the presence of a bacteria EZ at the Nafion surface was first verified and confirmed for *E. coli* ATCC 25922 cells suspended in a low IS phosphate buffer. A zone depleted of *E. coli* ATCC 25922 cells was clearly observed, with thickness ranging between 50 μm and 100 μm (Figure 33c). However, it should be noted that the transition from EZ to the bulk suspension occurred gradually, over tens of micrometers, a region that we termed transition zone

(TZ). Since this is more evident in the 3D Z-stacked images (Figure 33d) than the 2D single-slice images (Figure 33c), the 3D images were used for visualization and quantification of EZ throughout this work.

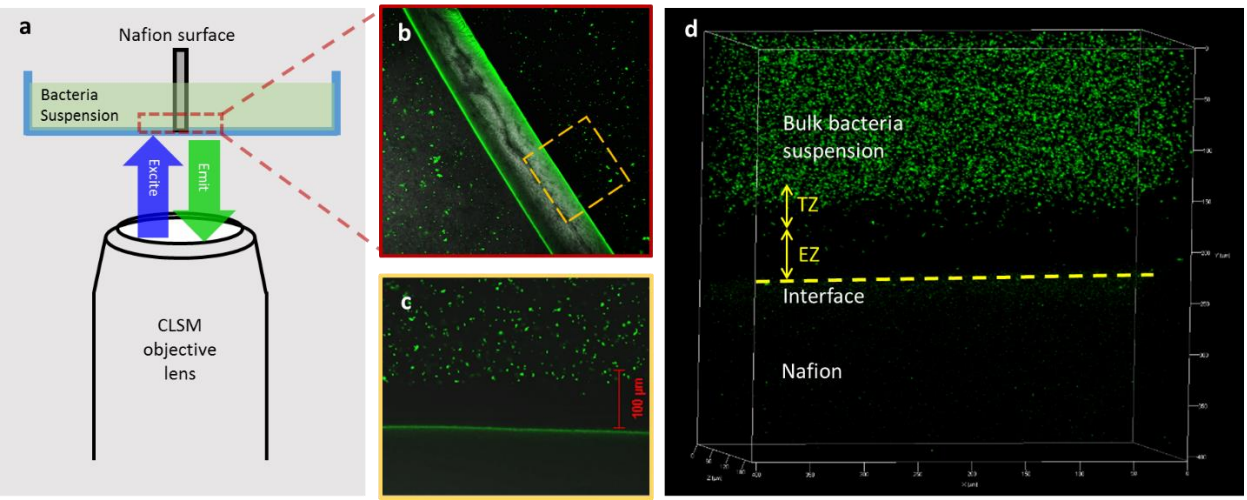

Figure 33. Evidence for the existence of bacteria exclusion zone at Nafion-bacteria suspension interface. **(a)** The setup for CLSM; **(b)** Combined Bright-field and fluorescence microscopic view of the cross-section of Nafion substrate immersed in bacteria suspension (a bottom-up view); **(c)** Zoomed-view at the Nafion-bacteria suspension interface enclosed by the dashed-line square in (c); **(d)** A 3D image of the interface taken by CLSM scanning in vertical direction (TZ: transition zone; EZ: exclusion zone). The dashed line indicates the location of interface.

The surface of Nafion itself emitted green fluorescence during CLSM inspection, forming a thin, continuous green line at the Nafion-bacteria suspension interface (Figure 33b and Figure 33c). To verify that this green fluorescence was indeed caused by the Nafion itself and not by bacteria adhered at the interface, a clean Nafion coupon was submerged for 10 min in dye-containing sterile TSB without bacterial cells, followed by CLSM visualization. Figure 34 shows

that a homogeneous green fluorescence line was observed at the interface even in the absence of bacteria. This line was comprised of single-pixel "dots", which aligns with the fact that SYTO 9 has a molecular weight of about 400 Da, or an equivalent diameter of about 1 nm.[23] Since SYTO dyes typically contain a net positive charge at neutral pH,[24] they could be electrostatically attracted to the sulfone groups branches of Nafion (pKa = - 6)[25] that carry negative charges at the neutral pH of TSB or BPB. Corroborated, these facts demonstrate that the green line was due to the adsorption of the green fluorescent SYTO 9 molecules to Nafion surface. Therefore, this adsorption line was used to delineate the Nafion-liquid interface when quantifying the EZ.

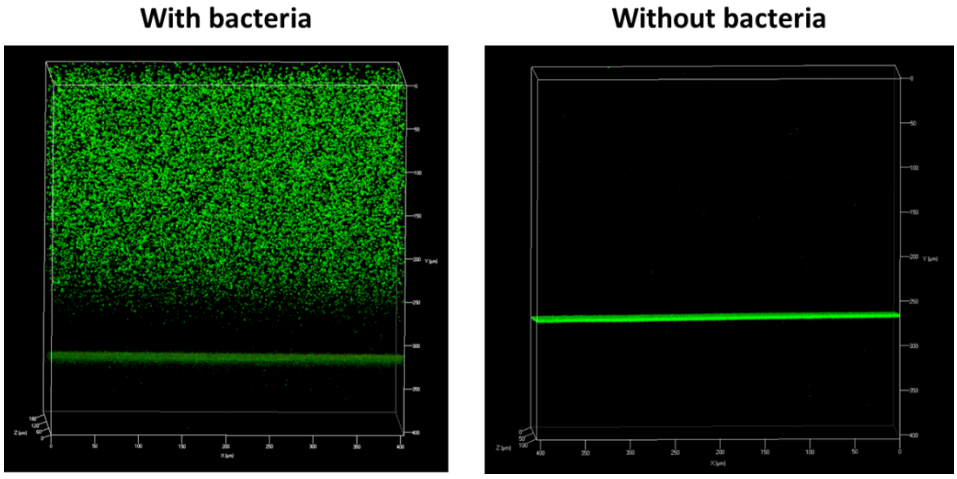

Figure 34. CLSM images of Nafion-TSB interface after 10-min equilibration in dye-containing TSB medium with (left) or without (right) *L. innocua*. The adjacent ticks on vertical axis are 50 μm apart.

4.4.2. Evidence for EZ for pathogenic and nonpathogenic bacteria in nutritive culture medium

The interaction between bacterial cells and surfaces is complex, being governed by the interplay between biological factors[26,27] and physicochemical factors[18,27,28]. Properties of the

liquid medium such as pH[29], ionic strength[30], viscosity[31], surface tension[32], composition[33] also play a significant role in the attachment process. In this study, EZ for *E. coli* ATCC 25922 at the Nafion – liquid interface was observed in both BPB (*IS* ≈ 10 mM) and TSB (*IS* ≈ 100 mM), with the size of EZ in BPB being greater than in TSB (Figure 35). This is in agreement with previous reports that EZ size diminishes as salt concentration (IS) increases.[6,7] Since higher IS is more representative of conditions encountered in real-world applications, including food processing or medical environments, the subsequent experiments were conducted in the higher IS medium (TSB).

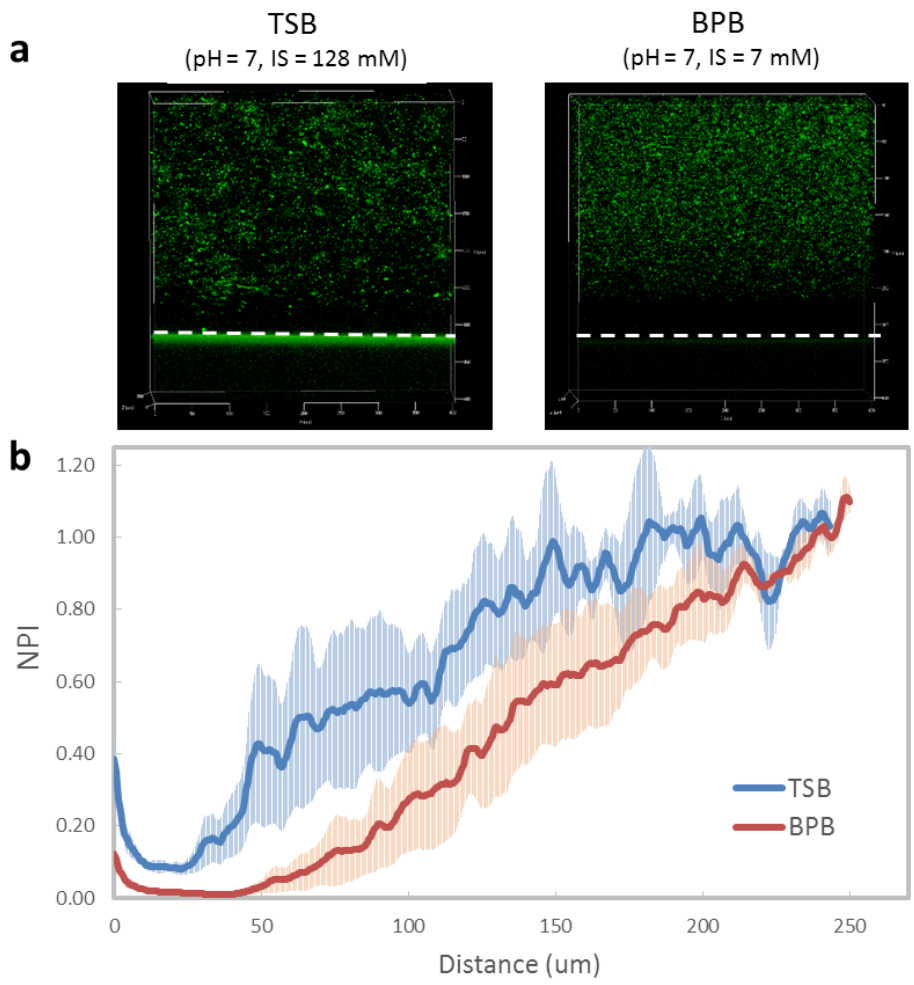

Figure 35. The distribution of E. coli ATCC 25922 cells in the vicinity of Nafion surface in two different dispersants. **(a)** 3D CLSM images of the Nafion-TSB interfaces, taken after 10 min of equilibration. The adjacent ticks on the vertical axis are 50 µm apart. **(b)** Normalized pixel intensity (NPI) profile for the bacteria dispersed in TSB or BPB. Error bars represent standard error of mean (*N* = 3).

The 3D CLSM images in Figure 36a show the presence of EZ at the Nafion-bacteria suspension interface for all three pathogenic strains. Another observation is that there was a noticeable difference in cell distribution near the interface for the pathogenic strains. *E. coli*

O157:H7 and *L. monocytogenes* cells appeared distributed in suspension as individual cells, whereas *S. aureus* cells seemed to agglomerate as clusters of different sizes. The propensity of *S. aureus* to form clusters has been reported before and is attributed to the polysaccharide intercellular adhesin located on the cell membrane surface.[34,35] The NPI profile plots in Figure 36b followed a comparable trajectory: NPI was very close to zero for the first 25 - 30 μm, then it started to increase away from the Nafion-TSB interface. The rate of increase was steeper between d = 25 and d = 50 μm, then it tapered off beyond d = 80 μm, and eventually reached a plateau beyond d = 150 μm. The NPI profiles for the three species were rather similar, although the NPI curve for *E. coli* O157:H7 was slightly lower than for *L. monocytogenes* and *S. aureus* above d = 40 μm, indicating a slightly lower cell density in the transition zone for this strain (Figure 36b).

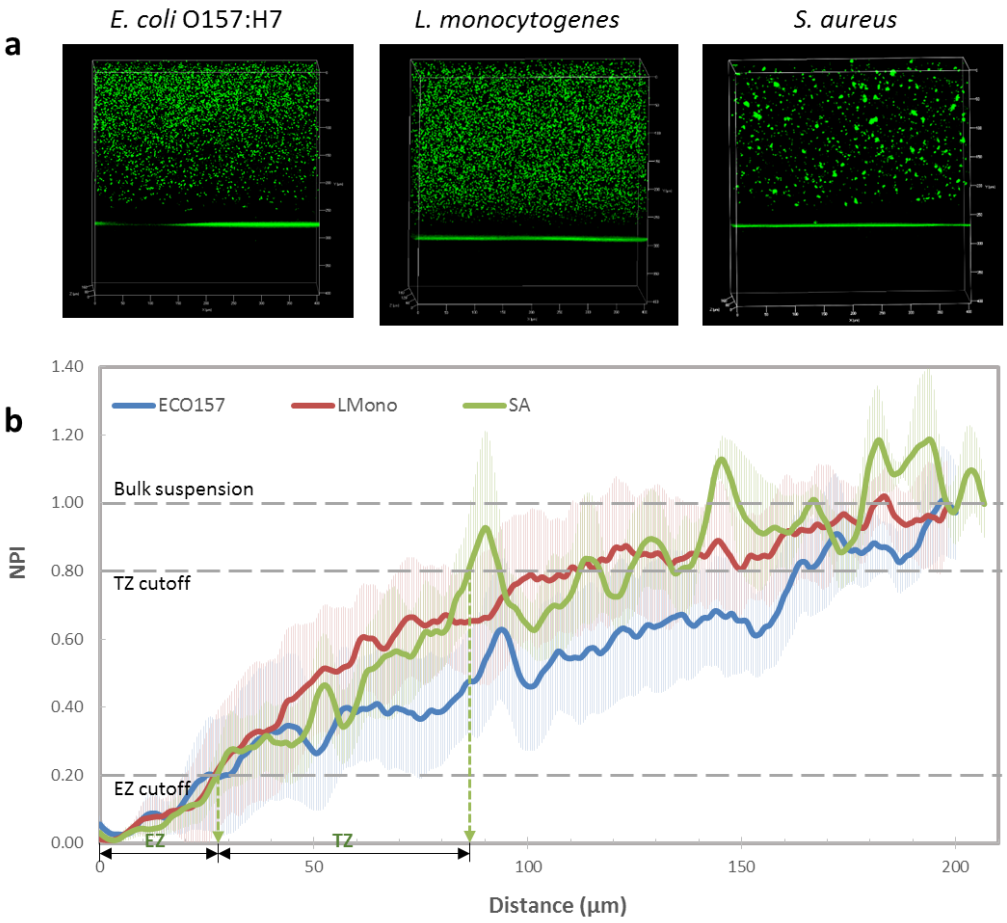

Figure 36. Exclusion zone (EZ) and transition zone (TZ) in the vicinity of Nafion-TSB interface exposed to various pathogenic strains. **(a)** 3D CLSM images of the Nafion-TSB interfaces, taken after 10 min of equilibration. The adjacent ticks on the vertical axis are 50 µm apart; **(b)** Normalized pixel intensity (NPI) profiles for the pathogenic strains in the vicinity of Nafion. Error bars represent standard error of mean ($N \geq 5$).

4.4.3. Quantification of exclusion zones and transition zones

As shown in Figure 37, the thickness values of EZ (average ± SE) for *E. coli* O157:H7, *L. monocytogenes*, and *S. aureus* were 50.3±13.0 µm, 37.2±12.5 µm, and 38.5±11.1 µm, respectively. For the same strains, the TZ averages (± SE) were 77.4±19.2 µm, 62.9±20.5 µm, and 41.5±5.4 µm, respectively. For all three strains, the EZ and TZ thickness values were significantly greater than zero ($p < 0.01$), indicating that the occurrence of EZs and TZs in this experiment is unlikely to be a random event. Despite the fact that the average size of EZ and TZ for *Staphylococcus* were slightly smaller than for *Escherichia* or *Listeria*, no statistically significant differences between were found across strains ($p > 0.05$). Additionally, no statistically significant differences were found when comparing the EZ and TZ of the nonpathogenic strains (*E. coli* ATCC 25922 and *L. innocua*) with their respective pathogenic counterparts (*E. coli* O157:H7 and *L. monocytogenes*, respectively) ($p > 0.05$). Therefore, in future studies, it would be acceptable to estimate the size of EZ or TZ for *E. coli* O157:H7 and *L. monocytogenes* using their nonpathogenic surrogates, *E. coli* ATCC 25922 and *L. innocua*, respectively.

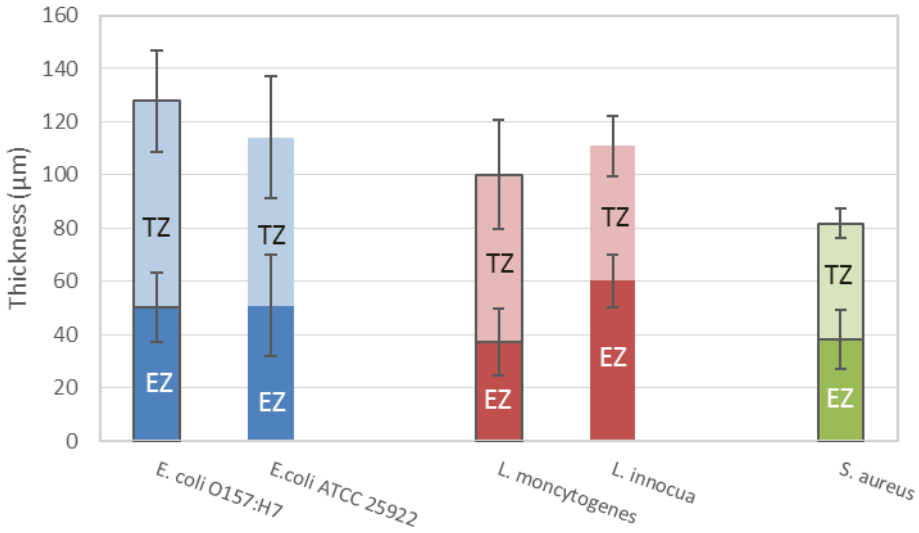

Figure 37. Size of exclusion zone (EZ) and transition zone (TZ) for the pathogenic (highlighted with solid borders) and surrogate strains (without borders) in the vicinity of Nafion-TSB interface. The error bars represent standard error of means for TZ or EZ ($N \geq 3$).

4.4.4. Implication of exclusion and transition zone for bacterial attachment

As the results shown above suggest, the generally agreed upon separation distance where bacterial cells start to be significantly influenced by material surface needs to be re-examined. The mainstream understanding of the physicochemical factors governing bacterial attachment can be based on the XDLVO theory, which attributes the repulsive forces exerted on bacterial cells primarily to the electrostatic repulsion and acid-base interaction.[36] However, the combined EZ-TZ region observed in the vicinity of Nafion featured a typical size of 80 µm - 120 µm (Figure 37), which far exceeds the typical effective range of electrostatic force (F_{EL}, typically within several tens of nanometers) or acid-base repulsive force (F_{AB}, typically within several nanometers) [27]. This disagreement can be further corroborated with force magnitude calculations based on the XDLVO theory, which reveal that for an *E. coli* cell departing the vicinity of a Nafion substrate,

both F_{EL} and F_{AB} become much smaller than 0.01 pN at a separation distance of 1 μm, and further decrease to essentially zero way before where the EZs were found to "fade out". Additionally, the average thrust force generated by a single swimming bacterium was theoretically calculated and experimentally measured to be 0.1 - 1 pN [37–40], more than 2 orders of magnitude greater than the total repulsive force a bacterium has to overcome (i.e. 0.01 pN) at a separation distance of 1 μm suggested by the XDLVO theory. Therefore, had F_{EL} and F_{AB} been the only sources of repulsive forces exerted on a bacterium, the thrust force generated by the flagella-bearing strains – in this case, *E. coli* ATCC 25922 and *E. coli* O157:H7 – should have been sufficient to propel the cell past the top boundary of EZ, at 40 μm – 60 μm from the interface (Figure 37). In fact, under the assumptions of the XDLVO theory, a thrust force of 1 pN would have been adequate to propel the cell to below 10 nm from the surface, until the sum of F_{EL}, $F_{AB,}$ and the hydrodynamic drag exceeds the thrust force, where the cell starts to decelerate and eventually stops. Nevertheless, the 3D CLSM images in Figure 36a indicate a much earlier stall of bacterial cells than predicted by the XDLVO theory. To directly probe the nature of the force responsible for this particle exclusion phenomenon, Chen and colleagues measured the force field in the vicinity of a Nafion-liquid interface at pN precision with optical tweezers. Using negatively-charged forces probes[41], they obtained a repulsive force of pN magnitude up to 50 μm away from the Nafion surface, which is in agreement with the EZ and TZ size presented in Figure 37.

The discrepancy between the XDLVO model predictions and experimentally measured cell-surface interaction forces shown in Figure 13 of Chapter One suggests the existence of other mechanisms conducive to this long range bacteria exclusion phenomenon. While the exact underlying mechanism for EZ is still presently unclear, two competing hypotheses have obtained more experimental support than others: the structured water hypothesis[6] and the diffusiophoresis

hypothesis[4]. Nonetheless, the possibility that the EZ phenomenon involves electrostatic or surface energy-related mechanisms should also be considered. Although more research is needed to further elucidate the nature of EZ, the discovery and confirmation of this far-reaching exclusion phenomenon against motile bacterial cells can have important implications for understanding bacterial attachment to both biotic and abiotic surfaces.

4.4.5. Effect of surface nanoscale topography on exclusion zone size and its implication for bacterial attachment

To investigate the effect of substratum surface nanoscale topography on the size of the EZ-TZ layer, the five types of alumina surfaces with distinctly defined surface topography (Figure 38, top panel) were submerged, as described in section 4.3.3, in a bacteria suspension consisting of Syto 9-labeled *L. innocua* cells and BPB (pH = 7.1, IS = 7 mM). After 10 min equilibration at 20 °C, CLSM 3D Z-Stack images were taken at the liquid-substratum interface for each type of alumina substratum, and the images were analyzed using ImageJ to generate NPI plots, from which the EZ-TZ sizes were extracted and compared with the bacterial attachment results.

The combined EZ-TZ size of the nanoporous AAO surfaces increases with decreasing pore diameter (Figure 38, middle panel), ranging from 69.08 ± 10.25 μm for the 100 nm pore AAO to 102.60 ± 19.53 μm for the 15 nm pore AAO (Figure 39b). The average combined EZ-TZ size for the nanosmooth alumina surfaces is 54.41 ± 12.82 μm, comparable to that of the 50 and 100 nm pore AAOs. Closer inspection of the interfacial region of the CLSM images reveals a discontinues layer of attached *L. innocua* cells, which is clearly different from the continuous green line caused by the adsorption of Syto 9 molecules to the Nafion surfaces (Figure 35a and Figure 36a). The relatively high NPI signals near $d = 0$ are also reflective of bacterial attachment at the liquid-

substratum interface (Figure 39a). The attachment of *L. innocua* cells to the EZ-TZ bearing AAO surfaces, including the 15 nm pore AAO which appeared to have the largest EZ-TZ size, could have occurred in two ways: 1) upon the first contact of the AAO substrate with the suspension, prior to the complete establishment of the EZ-TZ layer; 2) during the 10-min equilibration. In contrast with the absolutely cell-free EZ observed in the vicinity of the Nafion surfaces (Figure 34a and Figure 35a), the EZs near the nanoporous and the smooth alumina substrate contain sparsely distributed cells (Figure 38, middle panel), suggesting that the EZs near the alumina surfaces are less consistent or stable than those near the Nafion surfaces.

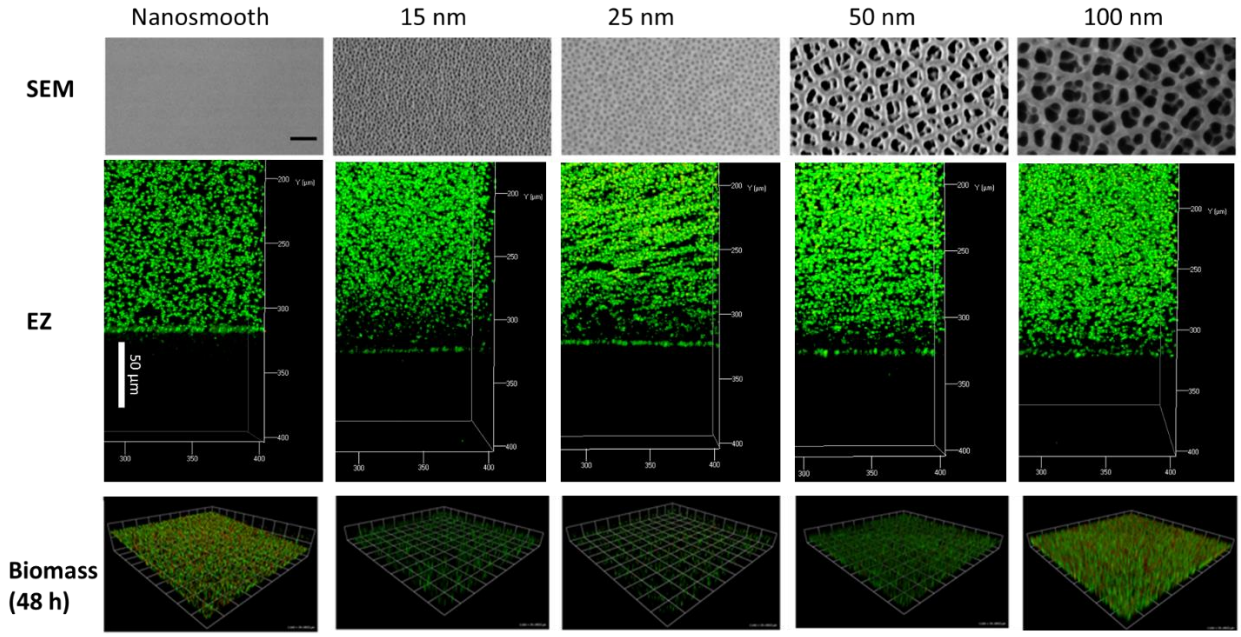

Figure 38. *L. innocua* exclusion zone in the vicinity of alumina substrates with different surface topography. Top panel: representative SEM images of the alumina substrates; Middle panel: 3D z-stack CLSM images taken at the solid-liquid interfaces; Bottom panel: biomass accumulation on these surfaces after 48 h incubation at 37 °C.

To investigate the impact of bacteria-exclusion zone on biomass accumulation over a longer time scale, the 48 h biomass accumulation of *L. innocua* on various alumina surfaces are presented below their respective interfacial CLSM 3D Z-stack images (Figure 39, middle and

bottom panels). The CLSM images indicate that the 15 nm and 25 nm pore AAOs had the largest EZ-TZ size after 10 min of contact and the least biomass after 48 h static incubation in TSB culture, which is substantiated by the quantitative comparison shown in Figure 39b. Despite that no statistically significant difference between these values was found across surface types ($p > 0.05$) except between the EZ size of 15 nm pore AAO and nanosmooth alumina ($p < 0.05$), the size of EZ and TZ appear to increase with decreasing pore diameters. Taken together, Figure 38 and Figure 39 reveal for the first time that surface nanoscale topography may have an impact on the size of EZ and TZ, which was shown earlier in this Chapter to substantially alter how bacteria approach and attach to solid substrates. The rising trend of EZ-TZ size from NS to 15 nm AAO coincides with the decreasing trend of 48 h biomass data, suggesting that the EZ-TZ phenomenon could have played a role in the low-fouling characteristic of the smaller pore AAO surfaces. More research is needed to determine whether the topographical dependence of the EZ-TZ barrier is a manifestation of the topographical dependence of the XDLVO interactions, or it is in and of itself an additional repulsion mechanism, not accounted for by the XDLVO theory.

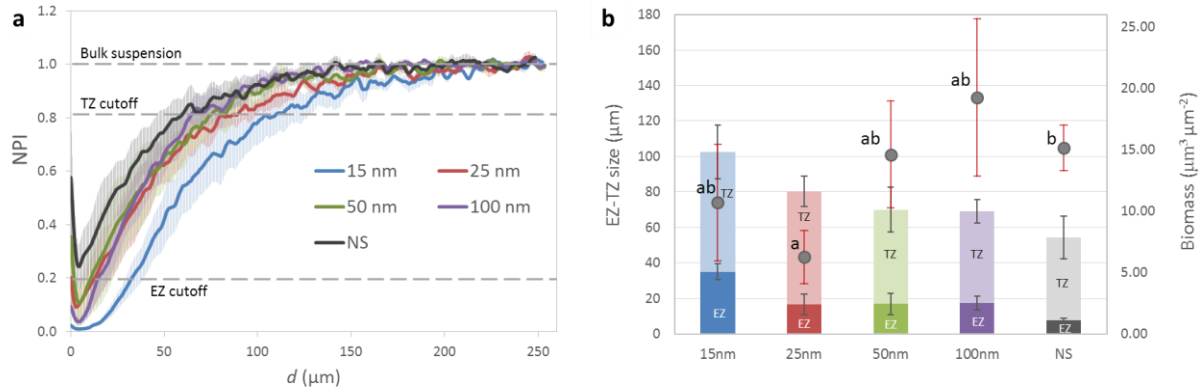

Figure 39. The bacteria-exclusion phenomena near nanoporous AAO surfaces and nanosmooth control in BPB (pH = 7.1, IS = 7 mM). **(a)** The NPI profiles for five types of alumina surfaces; **(b)** *L. innocua* EZ-TZ size (the bar plot) and 48-h biomass accumulation (the scatterplot) on these alumina surfaces. The error bars represent standard error of the mean. For the 48-h biomass data, values not connected by the same letter are statistically different from each other ($p < 0.05$).

4.5. Conclusions

Complementary to previous studies that demonstrated the existence of a long-range exclusion of abiotic colloidal particles in the vicinity of certain hydrophilic surfaces, here we show that such exclusion zones also exist for various bacterial strains. We further demonstrate that EZs are present both in a simple, low ionic strength liquid, as well as in a complex liquid medium of moderately high ionic strength that resembles various biological liquids. Surface nanoscale topography seems to have an impact on the size of EZ and TZ, which may contribute to bacterial attachment and possibly long-term biofilm formation behavior on these surfaces. The confirmation of this long range exclusion phenomenon for motile bacterial cells can have

significant implications for the understanding of bacterial attachment to hydrophilic biotic and abiotic surfaces. From a practical standpoint, these findings provide important insights into the potential of developing EZ-conducive coatings or materials as antifouling surfaces, in order to prevent attachment and fouling by bacteria. This could have implications for a range of applications related to human health and life, such as food and water processing or the biomedical industry.

REFERENCES

(1) Zheng, J.; Chin, W.; Khijniak, E.; Pollack, G. H. Surfaces and Interfacial Water: Evidence That Hydrophilic Surfaces Have Long-Range Impact. Adv. Colloid Interface Sci. 2006, 127 (1), 19–27.

(2) Musa, S.; Florea, D.; Wyss, H. M.; Huyghe, J. M. Convection Associated with Exclusion Zone Formation in Colloidal Suspensions. Soft Matter 2016, 12, 1127–1132.

(3) Schurr, J. M.; Fujimoto, B. S.; Huynh, L.; Chiu, D. T. A Theory of Macromolecular Chemotaxis. J. Phys. Chem. B 2013, 117 (25), 7626–7652.

(4) Florea, D.; Musa, S.; Huyghe, J. M. R.; Wyss, H. M. Long-Range Repulsion of Colloids Driven by Ion Exchange and Diffusiophoresis. Proc. Natl. Acad. Sci. U. S. A. 2014, 111 (18), 6554–6559.

(5) Siegismund, D.; Schroeter, A.; Lüdecke, C.; Undisz, A.; Jandt, K. D.; Roth, M.; Rettenmayr, M.; Schuster, S.; Germerodt, S. Discrimination between Random and Non-Random Processes in Early Bacterial Colonization on Biomaterial Surfaces: Application of Point Pattern Analysis. Biofouling 2014, 30 (9), 1023–1033.

(6) Zheng, J.; Pollack, G. H. Long-Range Forces Extending from Polymer-Gel Surfaces. Phys. Rev. E. Stat. Nonlin. Soft Matter Phys. 2003, 68 (3), 31408-1-031408–7.

(7) Zhao, Q.; Ovchinnikova, K.; Chai, B.; Yoo, H.; Magula, J.; Pollack, G. H. Role of Proton Gradients in the Mechanism of Osmosis. J. Phys. Chem. B 2009, 113 (31), 10708–10714.

(8) Chai, B.; Mahtani, a G.; Pollack, G. H. Unexpected Presence of Solute-Free Zones At Metal-Water Interfaces. Contemp. Mater. 2012, 3 (1), 1–12.

(9) Derjaguin, B. V. On Long-Range Forces of Repulsion Between Biological Cells. Colloids and Surfaces 1984, 10, 77–84.

(10) Pollack, G. H. Fourth Phase of Water; Ebner and Sons Publishers: Seattle, 2013.

(11) Green, K.; Otori, T. Direct Measurements of Membrane Unstirred Layers. J. Physiol. 1970, 207 (1), 93–102.

(12) Chai, B.; Yoo, H.; Pollack, G. H. Effect of Radiant Energy on near-Surface Water. J. Phys. Chem. B 2009, 113 (42), 13953–13958.

(13) Cameron, I. Dye Exclusion and Other Physical Properties of Hen Egg White. Water 2010, 2, 83–96.

(14) Elia, V.; Napoli, E.; Niccoli, M. Physical-Chemical Study of Water in Contact with a Hydrophilic Polymer: Nafion. J. Therm. Anal. Calorim. 2013, 112 (2), 937–944.

(15) Chen, C.; Farr, E.; Anaya, J.; Chen, E.; Chin, W. New Method of Water Purification Based on the Particle-Exclusion Phenomenon. Entropy 2015, 17 (3), 1466–1476.

(16) Klyuzhin, I.; Symonds, A.; Magula, J.; Pollack, G. H. New Method of Water Purification Based on the Particle-Exclusion Phenomenon. Environ. Sci. Technol. 2008, 42 (16), 6160–6166.

(17) Stoodley, P.; Sauer, K.; Davies, D. G.; Costerton, J. W. Biofilms as Complex Differentiated Communities. Annu. Rev. Microbiol. 2002, 56, 187–209.

(18) Feng, G.; Cheng, Y.; Wang, S.; Borca-Tasciuc, D. A.; Worobo, R. W.; Moraru, C. I. Bacterial Attachment and Biofilm Formation on Surfaces Are Reduced by Small-Diameter Nanoscale Pores:

How Small Is Small Enough? npj Biofilms Microbiomes 2015, 1 (December), 15022.

(19) Hizal, F.; Rungraeng, N.; Jun, S.; Choi, C. Nano-Engineered Alumina Surfaces for Prevention of Bacteria Adhesions. In Proceedings of the 9th IEEE International Conference on Nano/Micro Engineered and Moleculer Systems; 2014; pp 17–22.

(20) Zheng, J.; Pollack, G. H. Water and the Cell; Pollack, G. H.; Cameron, I. L.; Wheatley, D. N., Ed.; Springer Netherlands: Dordrecht, 2006.

(21) Goswami, S.; Klaus, S.; Benziger, J. Wetting and Absorption of Water Drops on Nafion Films. Langmuir 2008, 24 (16), 8627–8633.

(22) Schneider, C. a; Rasband, W. S.; Eliceiri, K. W. NIH Image to ImageJ: 25 Years of Image Analysis. Nat. Methods 2012, 9 (7), 671–675.

(23) Erickson, H. P. Size and Shape of Protein Molecules at the Nanometer Level Determined by Sedimentation, Gel Filtration, and Electron Microscopy. Biol. Proced. Online 2009, 11 (1), 32–51.

(24) Johnson, I. Chapter 8 - Nucleic Acid Detection and Genomics Technology. In The Molecular Probes Handbook: A Guide to Fluorescent Probes and Labeling Technologies, 11th Edition; Life Technologies Corporation, 2010; pp 269–283.

(25) Chaabane, L.; Dammak, L.; Nikonenko, V. V.; Bulvestre, G.; Auclair, B. The Influence of Absorbed Methanol on the Conductivity and on the Microstructure of Ion-Exchange Membranes. J. Memb. Sci. 2007, 298 (1–2), 126–135.

(26) Reisner, A.; Haagensen, J. a J.; Schembri, M. a; Zechner, E. L.; Molin, S. Development and Maturation of Escherichia Coli K-12 Biofilms. Mol. Microbiol. 2003, 48 (4), 933–946.

(27) Feng, G.; Cheng, Y.; Wang, S.; Hsu, L. C.; Feliz, Y.; Borca-Tasciuc, D. a.; Worobo, R. W.; Moraru, C. I. Alumina Surfaces with Nanoscale Topography Reduce Attachment and Biofilm Formation by Escherichia Coli and Listeria Spp. Biofouling 2014, 30 (November), 1253–1268.

(28) Hori, K.; Matsumoto, S. Bacterial Adhesion: From Mechanism to Control. Biochem. Eng. J. 2010, 48 (3), 424–434.

(29) Schwan, W. R.; Lee, J. L.; Lenard, F. A.; Brian, T.; Beck, M. T.; Matthews, B. T. Osmolarity and pH Growth Conditions Regulate Fim Gene Transcription and Type 1 Pilus Expression in Uropathogenic Escherichia Coli Osmolarity and pH Growth Conditions Regulate Fim Gene Transcription and Type 1 Pilus Expression in Uropathogenic Escherichia. Infect. Immun. 2002, 70 (3), 1391–1402.

(30) Li, B.; Logan, B. E. Bacterial Adhesion to Glass and Metal-Oxide Surfaces. Colloids Surf. B. Biointerfaces 2004, 36 (2), 81–90.

(31) Petrova, O. E.; Sauer, K. Sticky Situations: Key Components That Control Bacterial Surface Attachment. J. Bacteriol. 2012, 194 (10), 2413–2425.

(32) Fletcher, M.; Pringle, J. H. The Effect of Surface Free Energy and Medium Surface Tension on Bacterial Attachment to Solid Surfaces. J. Colloid Interface Sci. 1985, 104 (1), 5–14.

(33) Parkar, S. G.; Flint, S. H.; Palmer, J. S.; Brooks, J. D. Factors Influencing Attachment of Thermophilic Bacilli to Stainless Steel. J. Appl. Microbiol. 2001, 90 (6), 901–908.

(34) Heilmann, C.; Heilmann, C.; Schweitzer, O.; Schweitzer, O.; Mack, D.; Mack, D.; Gotz, F.; Gotz, F. Molecular Basis of Intercellular Adhesion in the Biofilm-Forming. Mol. Microbiol. 1996, 20 (5), 1083–1091.

(35) Mack, D.; Fischer, W.; Krokotsch, A.; Leopold, K.; Hartmann, R.; Egge, H.; Laufs, R. The Intercellular Adhesin Involved in Biofilm Accumulation of Staphylococcus Epidermidis Is a Linear β-1,6-Linked Glucosaminoglycan : Purification and Structural Analysis. 1996, 178 (1), 175–183.

(36) Van Oss, C. J.; Chaudhury, M. K.; Good, R. J. Interfacial Lifshitz-van Der Waals and Polar Interactions in Macroscopic Systems. Chem. Rev. 1988, 88 (6), 927–941.

(37) Chattopadhyay, S.; Moldovan, R.; Yeung, C.; Wu, X. L. Swimming Efficiency of Bacterium Escherichia Coli. 2005, 103 (37).

(38) Behkam, B.; Sitti, M. Bacterial Flagella-Based Propulsion and On/off Motion Control of Microscale Objects. Appl. Phys. Lett. 2007, 90 (2), 12–15.

(39) Berke, A. P.; Turner, L.; Berg, H. C.; Lauga, E. Hydrodynamic Attraction of Swimming Microorganisms by Surfaces. Phys. Rev. Lett. 2008, 101 (3), 1–4.

(40) Darnton, N. C.; Turner, L.; Rojevsky, S.; Berg, H. C. On Torque and Tumbling in Swimming Escherichia Coli. J. Bacteriol. 2007, 189 (5), 1756–1764.

(41) Chen, C.-S.; Chung, W.-J.; Hsu, I. C.; Wu, C.-M.; Chin, W.-C. Force Field Measurements within the Exclusion Zone of Water. J. Biol. Phys. 2012, 38 (1), 113–120.

CHAPTER FIVE

SUGGESTIONS FOR FUTURE RESEARCH

This dissertation focused on understanding the effect of various physicochemical factors on bacterial attachment using a theoretical as well as an experimental approach. The adjusted XDLVO model developed in this work provides a framework for quantitatively evaluating the interaction force between bacterial cells and surfaces with nanoscale pores. The maximum repulsive force (F_{max}) calculated from the model can serve as a predictor for the tendency of a specific bacterial strain to attach to various solid substrates. However, F_{max} alone failed to predict biofilm formation by certain bacterial strains capable of establishing vertical micro-colonies via strong cell-cell interactions. Future modeling efforts could focus on building a cell-cell interaction component into the current XDLVO model.

Another important role of the model is to provide a roadmap for engineering surfaces with even better antifouling effect. Results from Chapter Three show that by decreasing pore diameter or increasing surface porosity, F_{max} can be increased further, and thereby more bacteria-repellent can be achieved. The current record for the smallest pore diameter achieved on AAO surfaces is 12 nm. Future breakthroughs in anodization technology may allow further lowering the diameters of the pores, without a significant reduction in porosity, or increasing porosity, which could lead to more effective bacteria-repellent surfaces. Modifying surface chemistry is another route to enhance F_{max}, which could be achieved by applying a very thin coating of a material with intrinsic bacteria-repellent surface energies (i.e. high γ^- and low γ^+ and low γ^{LW}) to the nanostructured surfaces. This coating needs to be thin enough, not exceeding several nanometers, in order not to interfere with nanoscale surface topography.

Evidence of long-range bacteria exclusion zones was found in the vicinity of Nafion and alumina surfaces (Chapter Four). Both surface chemistry and surface topography have been found to affect the size of EZ, but how each of these physicochemical factors influences EZ still remains to be discovered. Another interesting phenomenon associated with EZ is that incident radiant energy has been shown to expand the size of EZ in a wavelength dependent manner, with a maximum degree of expansion in the mid-infrared region.[1] This could prove to be an accessible means of improving the antifouling capability of the EZ-bearing surfaces. It is also quite interesting to think about what bacterial cells approaching an EZ-bearing surface may experience. Could EZ trigger any change in the transcriptome or proteome of the cells inside EZ? What is the implication of EZ for the nutrient accessibility of cells located in the vicinity of such surfaces? Since EZ has been found near a wide range of natural hydrophilic surfaces, could it be possible that some bacterial strains have developed coping mechanisms against EZ, which allow them to approach hydrophilic surfaces?

All of these open questions deserve further research, as they may provide useful answers to the fascinating world of microbial life and behavior, with tremendous implications for many areas that affect human health and life in general.

REFERENCES

(1) Chai, B.; Yoo, H.; Pollack, G. H. Effect of Radiant Energy on near-Surface Water. *J. Phys. Chem. B* **2009**, *113* (42), 13953–13958.